MICROMAGNETIC AND TRANSPORT SIMULATION OF MAGNETIC NANOSTRUCTURES

GUO JIE

NATIONAL UNIVERSITY OF SINGAPORE

2006

MICROMAGNETIC AND TRANSPORT SIMULATION OF MAGNETIC NANOSTRUCTURES

GUO JIE

(B. Eng, NORTHWESTERN POLYTECHNICAL UNIVERSITY)

A THESIS SUBMITTED

FOR THE DEGREE OF PHILOSOPHY

DEPARTMENT OF ECLECTRICAL AND COMPUTER

ENGINEERING

NATIONAL UNIVERSITY OF SINGAPORE

2006

ACKNOWLEDGMENT

This author would like to express her heartfelt gratitude to her supervisor, Dr. Mansoor Bin Abdul Jalil for his concern, encouragement and advice throughout the course of the project.

The author would like to thank Miss Loh Fong Leong, Miss Liu Ling, Mr. Maung Kyaw Min Tun, Darren and Mr. Wong Wai Kong, Alaric and Prof. Jiang Yong for their kindly assistance and advice.

In addition, the author is grateful for the friendship and support of Wang Xiao Qiang, Cheng Xing Zhi, Verma Lalit Kumar, Agrawal Saurab, Chen Chao, Chen Wen Qian and other research engineers and research scholars in the Information Storage Materials Laboratory.

Last but not least, the author would like to thank her family for their love, support and understanding during the period of the research project.

TABLE OF CONTENTS

SUMMARY

The requirement for reducing the feature size of magnetic sensor devices and increasing the bit density of magnetic media used in ultra magnetic recording has led to the development of patterned magnetic materials. Advances in lithography and nanofabrication techniques have enabled the controlled fabrication of materials down to deep submicron or nanometer scale. Accompanying this progress is the rapid growth in computational power and improvement in numerical techniques, which makes simulation an effective tool to study the magnetic and electrical properties of the patterned magnetic nanostructures. In this thesis, the magnetic and transport properties of two important magnetic nanostructures, the antidot array and the spin-valve magnetic multilayer structures, are investigated using finite element analysis and micromagnetic simulation. A transport model was first presented to study the lateral transport properties of Permalloy films patterned with an antidot array. The transport model considers the nonuniform current density distribution, which is influenced by the film geometry, as well as the Planar and normal Hall effects. The variation in properties such as coercivity and anisotropy magnetoresistance as a function of geometry was presented. In addition, to investigate the applicability of the structure for magnetic recording applications, recording parameters such as signal to noise ratio and the magnetization switching mechanism were studied, and optimal conditions in terms of geometry and bias fields are determined. In the next half of the thesis, we investigate a new method of magnetization switching in magnetic multilayer nanostructures i.e. current-induced magnetization switching (CIMS). We first investigate the CIMS effect in ring-shaped spin-valve device, and consider the contributions from both the Oersted fields and the interfacial spin dependent scattering

effects. From this analysis, we obtain the current pulse amplitude and duration for optimal switching speed. Next, we develop a CIMS model in planar spin-valve multiplayers which combines the contributions transmitted spin current due to ballistic (specular) scattering at interfaces, and the relaxation of the transverse spin accumulation within each of the layers. The effective field due to the CIMS effect, and the corresponding critical current density j_c are determined, and the value of j_c obtained agrees well with existing experimental observations. In addition, our model predicts that j_c can be substantially reduced by considering two modified pseudo-spin-valve structures, i.e. one having a Ru cap layer and the other having layers which are magnetized in the out-of-plane direction. The detailed analysis of the spin transport and spin transfer torque in magnetic multilayer structures has improved our understanding of the CIMS mechanism, and increases the prospect of utilizing this new switching method in future spintronics devices, e.g. in MRAMs.

SYMBOLS AND ABBREVIATIONS

Å	Angstroms (10^{-10}m)
AMR	Anisotropy Magnetoresistance
B	Magnetic flux density
CIP	Current in plane
CPP	Current perpendicular to plane
Co	Cobalt
DC	Direct current
E_F	Fermi energy
Fe	Iron
FM	Ferromagnetic
GMR	Giant magnetoresistance
H	Magnetic field strength
Hc	Coercivity field
I	Current
M	Magnetization
Mr	Remnant magnetization
MR	Magnetoresistance
MRAM	Magnetic random access memory
MTJ	Magnetic tunnel Junctions
nm	Nanometer (10^{-9} m)
$Ni_{80}Fe_{20}$	Permalloy (Py) with 80% Nickel and 20% Iron composition

PSV	Pseudo spin-valve
RT	Room temperature
Ru	Ruthenium
TMR	Tunneling magnetoresistance
V	Voltage
μ	Micro (10^{-6} m)
Ω	Ohms

LIST OF FIGURES

Chapter 1 Introduction

1.1Background

Computer modeling of magnetic nanostructures is increasingly important due to the relentless trend of decreasing feature size of magnetic elements used in magnetic recording media and magnetic sensor devices, coupled with the rapid growth in available computational power. In addition, advances in lithography technology and microscope have enabled better controlled fabrication of deep sub-micron to nanometer scale structures, and it has been made possible to engineer new magnetic properties in magnetic nanostructures by patterning or by interfacing magnetic materials with other materials (e.g. in a multilayer structure). In this thesis we will conduct a theoretical and computational study of magnetic and transport properties of some important patterned nanostructures, such as the antidot array and spin-valve multilayers. Micromagnetic and transport analysis of antidot arrays with different geometries will be first discussed. The magnetization of nanostructures is also strongly influenced by interface effects and spin transfer phenomena. Therefore, the latter half of the thesis will focus on modeling effects of spin torques, particularly, the current-induced magnetization switching (CIMS) in spin-valve structures. In addition, a refined version of the standard micromagnetic technique, which includes the spin transfer torque, is developed in order to study the switching mechanism of spin valve structures.

The invention of paper by Chinese represented a great step forward for human technology, as it allows us to conveniently record a permanent record. However, with the

explosion of knowledge presented to us in this age of information, we require new types of media to store huge amount of information, which is being continuously generated. For this purpose, electronic data storage devices are ideally suited due to its large capacity and low price. There are many kinds of data storage devices available now, such as magnetic tapes, compact disks and hard disk drives. Of these, the hard disk drive is the most popular due to its high capacity and high access speed. Hard disk drives make use of a magnetic thin film as recording media.

Since the 1980s there has been an exponential growth in the bit area density of magnetic media used in hard disk drives, which is driven by the insatiable demand from consumers for ever greater storage space. At present the bit density of disk media has exceeded 100 Gb/in^2 and further exponential increase may not be possible if hard disk drives continue to rely on continuous media, which are either magnetized longitudinally, or perpendicular to the media plane. This is due to increasing instability as a result of thermal fluctuations as individual grains of the media decrease in size. When the superparamagnetic size range is approached, thermal effects become strong enough to induce random flipping of the magnetic moments, and the nanoparticles have zero magnetization on average. In order to overcome this limitation, self-organized patterned media arrays have been proposed as an alternative to continuous media. Such patterned media possess a higher thermal stability because each patterned element is larger in size compared to individual grains in continuous media. Thus, the use of patterned media may eventually lead to recording of one single particle per bit, and achieve ultimate area densities of close to 50 Tb/in^2 [1] before it reaches the superparamagnetic limit.

1.2 Motivation

Magnetoelectric transport properties of patterned nanomagnetic structures with the current in-plane direction have been well studied. Some examples are anisotropy magnetoresistance (AMR), magnetic domain wall switching, domain wall resistance and Planar Hall effect (PHE). However, in the analysis of the electron transport of magnetic patterned structures, all the existing models assumed that the current direction is parallel to the applied electrical field direction. It is also assumed that the current is uniformly distributed within the magnetic materials. These assumptions may be valid for conduction within a uniform bulk film. However, for nanostructured magnetic films, the current direction is constrained by the geometry to flow inhomogenously. The current direction plays an important role in the analysis of its magnetic properties, such as the AMR and Planar Hall effects. Thus it is necessary for us to analyze the transport properties of the patterned magnetic nanostructure and this analysis could be further utilized to calculate the AMR response of the antidot array.

On the other hand, the electric and magnetic properties of the magnetic multilayer structures with the current perpendicular to plane direction have also been extensively studied, including magnetic tunnel junctions and giant magnetoresistance, where the spin dependent scattering at the nonmagnetic/magnetic interface are crucial in these structures. In 1996, Berger [2] and Slonczewski [3] made the first predictions of the CIMS effect in the current perpendicular to the plane of magnetic multilayers. The CIMS can be regarded as the opposite phenomenon to the GMR effect. It has attracted much attention due to its advantages of the small power consumption and less risk of crossing writing.

But until now, the theoretical mechanism of the current-induced magnetization switching is not very clear. In particular, the in-depth understanding of the origin of the switching mechanism and the different modes of the switching is still lacking. None of the existing theoretical models can completely predict or explain all of the experimental results. For example, Jiang *et al.* [4] discovered that the utilization of Ru as the capping layer of the spin valve could dramatically reduce the critical current density. This observation cannot be explained by any of the existing models. Therefore, there is still a lot of work to be done in the exploration of the mechanism of CIMS and critical current density in the spin valve nanostructures.

1.3 Objectives

From the brief review in section 1.2, we can see much scope for further development of micromagnetic and magnetotransport studies of magnetic nanostructures. This thesis will focus on two specific magnetic nanostructures, namely the antidot (nano-patterned film) and the magnetic multilayers. The work described in the thesis aims to achieve the following objectives:

1) Present a combined micromagnetic and magnetotransport model which accounts for non-uniformity of both magnetization and current density distribution in the antidot arrays, and investigate the influence from geometry, Planar and normal Hall effects on the magnetic behaviour of the antidot arrays.

2) Model the magnetization and spin transport in a magnetic multilayered spin-valve, and calculate the spin polarization of current and the switching characteristics of the multilayer for a current perpendicular-to-plane (CPP) geometry.

3) Develop a model for the mechanism of the current-induced magnetization switching in a magnetic multilayer, which includes the effects of spin accumulation, diffusive spin relaxation within the layers, and ballistic spin-dependent transmission and scattering at the interfaces.

4) Incorporate the effect of the spin transfer into Landau-Lifshitz-Gilbert (LLG) equation to explore the dynamics of the magnetization reversal process in the presence of a spin polarized current and calculate the critical current density.

The aspects studied here may lead to a better understanding of the electric and magnetic properties of the patterned magnetic nanostructures. The transport model could also be used in the analysis of magnetotransport properties of other patterned magnetic nanostructures. The analysis of spin transport and the mechanism of the CIMS in the spin-valve structure are significant in view of the intense interest at present in utilizing CIMS as a new magnetization switching mechanism, without requiring an external magnetic field.

1.4 Outline of Thesis

The thesis is divided into six main chapters, as detailed in the table of contents.

In chapter 2, we will discuss several basic theories related to micromagnetic and magnetotransport simulation of patterned magnetic nanostructures. We will discuss the four basic terms in the free energy expression of a micromagnetic system, and the methods used to minimize this free energy, and approach the equilibrium energy state. We will also discuss transport phenomena such as magnetoresistance and the Hall effect. Some basic elements of finite element methods (FEM) are also included since we adopt FEM in both our transport and micromagnetic simulations. In addition, we will review some previous works on the transport and micromagnetic properties of the nanomagnetic structures, in both the current in-plane and current perpendicular-to-plane geometries.

In chapter 3, we will discuss the lateral transport and magnetic recording properties of a specific type of magnetic nanostructure, i.e. the regular antidot arrays in the current-in-plane geometry. Magnetic reversal processes and the AMR behavior in these structures are numerically evaluated, with consideration of the inhomogeneous current density distribution and magnetization configuration. We will investigate the effect of geometry, e.g. antidot size, film thickness and aspect ratio on the micromagnetic and magnetic switching properties of the antidot arrays. We will also evaluate its magnetic recording parameters, such as the signal-to-noise-ratios.

In chapter 4, we will study the magnetization switching in a ring-shaped pseudo-spin-valve (PSV) structure with the application of the perpendicular-to-plane current. The switching conditions between the two stable vortex states of the ring element are analyzed and optimized as a function of current pulse size and duration. Additionally, we also propose a purely diffusive spin transport model to analyze the spin transfer torque and critical current density in the PSV structure, with and without a Ru capping layer.

Chapter 5 presents a new combined ballistic and diffusive model to analyze the effect of spin torque in spin-polarized CIMS in PSV structure. This model incorporates ballistic spin-dependent transmission/reflection of electrons at the interfaces, and the diffusive relaxation of spin accumulation within the free layer. The combined model is utilized to theoretically explore the possibility of reducing critical current at PSV by using a strong spin scattering capping layer or by varying the easy axis in the out-of-plane orientation.

The last chapter concludes this thesis and suggests future works in the relevant areas.

References

[1] Dieter Weller, Assault on storage density of 1 terabit per square inch and beyond, IEEE Trans. on Magn., 39 (6): pp.3476-3476. 2003.

[2] L. Berger, Phys. Rev. B, vol. 54, pp.9353-9358. 1996.

[3] J. C. Slonczewski, J. Magn. Magn. Mater., vol. 159, pp.L1-L7. 1996.

[4] Y. Jiang, S. Abe, T. Ochiai, T. Nozaki, A. Hirohata, N. Tezuka and K. Inomata, Phys. Rev. Lett. 92, pp.167204. 2004.

Chapter 2 Theory and Review

2.1 Introduction

In the previous chapter, we have discussed the historical development of the recording media technology. Extensive studies have been carried out on different patterned magnetic nanostructures, such as circular dots [1], square dots [2], modulated wire [3] and truncated cone [4]. This thesis will focus on two specific magnetic nanostructures, namely:

- Patterned antidot array: Its lateral transport and magnetic recording properties under the application of an in-plane current (CIP) will be studied;
- Magnetic multilayer (spin valve) structure: The current-induced magnetization switching (CIMS) with the application of the perpendicular-to-plane current (CPP) will be discussed.

In this chapter, some important magnetotransport phenomena, which arise in magnetic nanostructures, such as anisotropy magnetoresistance (AMR), giant magnetoresistance (GMR), tunneling magnetoresistance (TMR) and the planar Hall effect (PHE) will be introduced. In addition, some simulation methodologies will be discussed, including the micromagnetic and finite element methods, which are adopted in the analysis of magnetic and transport properties of magnetic nanostructures. Finally, relevant literature will be reviewed, with special emphasis on work related to patterned magnetic nanostructures and the current induced magnetization switching (CIMS) in magnetic multilayers.

2.2 A Survey on MR and Hall Effects

One of the most distinctive electric transport properties of magnetic materials is their magnetoresistance (MR) effect, i.e. the electrical resistance of a magnetic structure changes with the application of externally applied magnetic fields. Furthermore, the MR effect can be grouped as AMR, GMR or TMR due to their different arising mechanisms. Hall effect is another important electromagnetic property for magnetic conductor such as the normal and planar hall effects (PHE), which will be also discussed in the following sub-sections.

2.2.1 Anisotropy Magnetoresistance (AMR)

The anisotropy magnetoresistance effect is a magnetoresistive effect observed in a uniform (i.e. made of a single material) ferromagnetic sample with the application of an in-plane current. It is defined as the fractional difference in the resistance when current is flowing along the magnetization **M** as compared to the resistance when the current is perpendicular to **M** [5]. AMR is dependent on the angle q between the current direction and the magnetization orientation of the sample and it can be expressed as

$$r = r_{\perp} + \Delta r \cos^2 q \tag{2.1}$$

where r is the film resistivity, $\Delta r = r_{\parallel} - r_{\perp}$ represents the maximum change in resistivity due to the AMR effect, $r_{\parallel}$ ($r_{\perp}$) is the resistivity for the electrical current applied parallel (perpendicular) to the local magnetization direction, respectively.

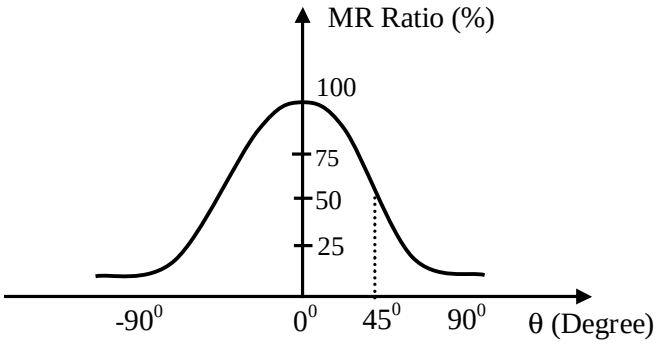

Figure 2.1 Variation of the normalized magnetoresistance ratio with the angle θ between the magnetization direction and electron current direction.

The AMR ratio is defined as Equ. (2.2) and the plot of normalized MR ratio as a function of q is shown in Fig 2.1. We can see that the AMR reaches its maximum (minimum) value for $q = 0^0$ ($q = \pm 90^0$).

$$AMR(\%) = \frac{\Delta R}{R} = \frac{R(H) - R(H=0)}{R(H=0)} \times 100\% \qquad (2.2)$$

The direction of magnetization can be altered by an externally applied magnetic field as shown in Fig 2.2.

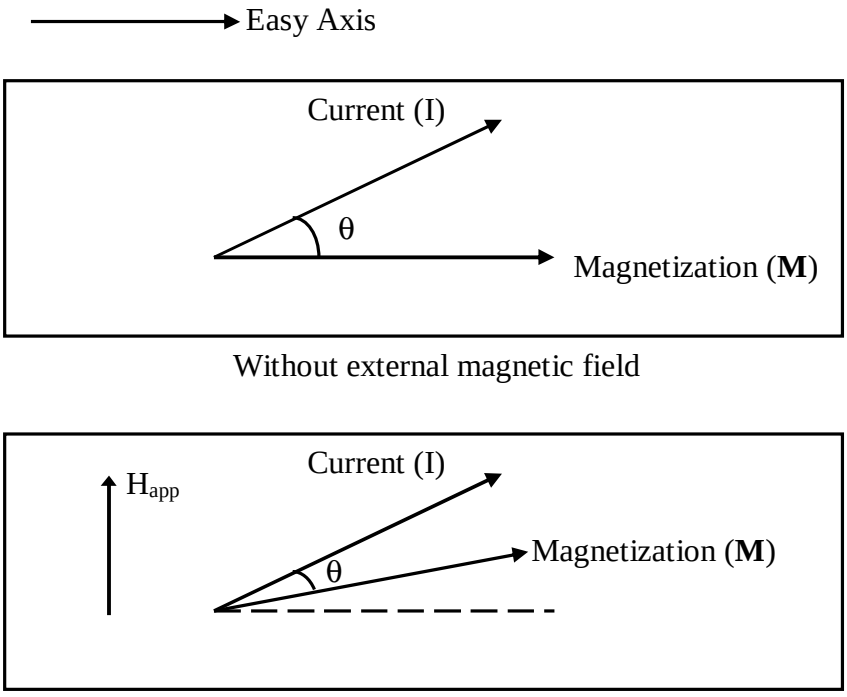

Figure 2.2 Schematic diagram of the AMR effect without external magnetic filed (upper) and with external magnetic field H_{app} perpendicular to easy axis (lower).

The basic origin of AMR is the spin-orbit interaction (SOI), which causes spin flip scattering between the *s* and *d* states, leading to a contribution in the anisotropy of the resistivity. When the SOI is inoperative, there is no s-d interaction in the majority-spin channel, while when SOI is turned on, $s^{\uparrow}$ electrons have some probability of being scattered into $3d^{\downarrow}$ hole states, and hence the total resistivity increases. The SOI also allows $d^{\uparrow} \rightarrow s^{\downarrow}$ transition that open $3d^{\uparrow}$ hole states, which provide further channels for *s-d* scattering. When the current is parallel to the magnetization direction, the *s-d* interaction is non-zero and spin mixing and spin flipping always increase the total resistance. Therefore the AMR is high (low) when the current is parallel (perpendicular) to

magnetization direction.

The AMR-based read head was first introduced in mobile drives around 1994 and in desktop drives around 1995. In order to optimize the read and write capabilities, the read and write elements in the AMR head are separated. The read element in an AMR head is composed of a thin strip of magnetic material. The stripe's magnetoresistance changes in the presence of a magnetic field, producing a strong signal, i.e. AMR effect. Normally the strip is made of by soft magnetic materials such as Permalloy, so that the magnetization direction of the sensor can be easily switched. This enables the magnetoresistance to be altered in response to a small magnetic field. However, the main drawback of AMR-based read head sensor is its low MR ratio and hence low sensitivity [6]. Thus, AMR-based read head sensors have been totally superseded by sensors utilizing the GMR effect, which is described in the next section.

2.2.2 Giant Magnetoresistance (GMR)

The giant magnetoresistance (GMR) effect was first reported in Fe/Cr multilayers [7] and in Co/Cu superlattice [8] in the late 1980's. The electrical resistance of these structures was found to highly sensitive to the relative orientation of the magnetization of alternate ferromagnetic layers. The resistance of the multilayers can change up to 50%, which is extremely large, compared to the AMR effect.

After the initial discovery of GMR effect, many researchers reported the observation of GMR in other types of ferromagnetic/non-magnetic metal multilayers. It was found that there are two pre-requisites [9] for the GMR effect: 1) the relative

magnetization orientation of adjacent ferromagnetic layers must be changeable; and 2) the electron transport distance between the multilayers must be shorter than the electron mean free path.

Generally, GMR effect arises because of the spin dependent scattering either at the interface between the ferromagnetic/non-magnetic metal layers or within the ferromagnetic layer. The mechanism of the GMR can be described by a simple two current model, which was proposed by A. Barthélémy ***et al.*** [10] as shown in Fig 2.3.

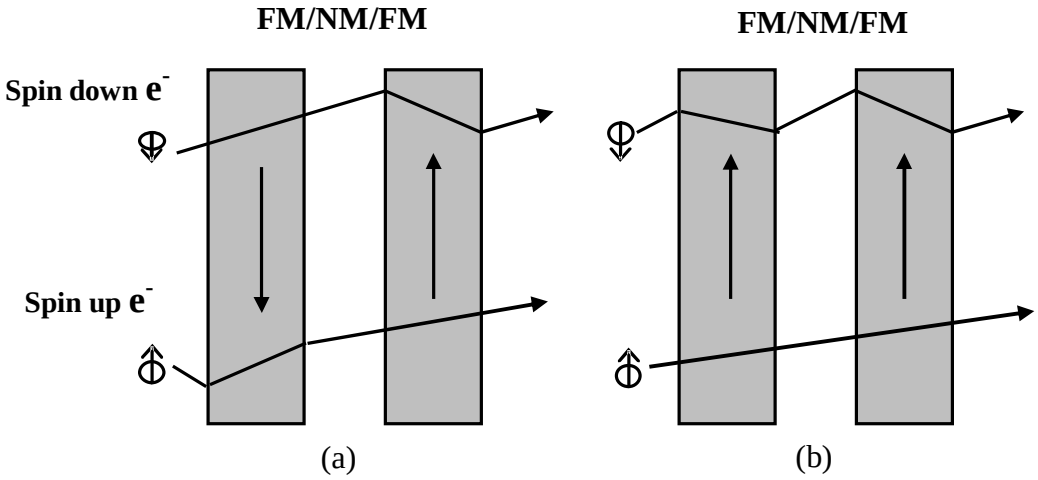

Figure 2.3 Schematic diagrams showing the scattering process at (a) antiparallel of the two FM layers and (b) parallel of the two FM layers. The dark arrows represent the majority spin directions in the magnetic layer.

Figure 2.3 presents two schematic configurations of the multilayers (a) antiparallel and (b) parallel. In the parallel configuration, the spin up and spin down electrons represent the majority and minority electron channels in the magnetic layer. These two electron channels encounter different resistivities r_+ and r_- due to the spin-dependent scattering probability, i.e., the majority (minority) electrons will experience lower (higher) scattering probability, resulting in a low (high) resistance. For the parallel configuration, the overall

resistivity r_P is given by

$$r_P = \frac{2 r_+ r_-}{r_+ + r_-} \tag{2.3}$$

In the antiparallel configuration, the electrons in both channels are alternatively majority and minority spin electrons with respect to the local magnetization orientation, and the overall resistivity r_{AP} can be expressed as

$$r_{AP} = \frac{r_+ + r_-}{2} \tag{2.4}$$

In the two-current model, the GMR ratio is given by

$$GMR = \frac{R_{AP} - R_P}{R_P} \times 100\% = \frac{(r_+ - r_-)^2}{4 r_+ r_-} \times 100\% \tag{2.5}$$

When the GMR effect is utilized for sensor applications in magnetic read heads, the magnetic multilayer of Fig. 2.3 is usually replaced by a simpler spin-valve structure consisting of four basic layers:

- Free layer - The free layer is typically made of a nickel-iron alloy, which is passed over the surface of the data bits to be read. It is free to rotate in response to the external magnetic field.
- Spacer - Typically made of copper, which is a nonmagnetic layer. The spacer separates the free and pinned layers, so their magnetizations are not coupled to one another.
- Pinned layer - A layer of hard ferromagnetic material whose magnetization is not affected by the applied magnetic field. The magnetization of the hard layer is pinned by antiferromagnetic coupling to the adjacent pinning layer.

- Pinning layer - A layer of antiferromagnetic material, e.g. FeMn, which fixes the pinned layer's magnetization.

In the above spin-valve structure, there exists two kinds of exchange couplings: i) Ruderman-Kittel-Kasuya-Yoshida (RKKY) coupling [8] between the two ferromagnetic layers. The RKKY interaction arises from the exchange of two (or more) localized spins, which is mediated via the spin polarization of the surrounding conduction electrons. The sign of the exchange interaction between two ferromagnetic layers oscillates as a function of distance between the two ferromagnetic layers, with a periodicity $l_F = p / K_F$ where K_F is the wave vector of the Fermi surface, and ii) antiferromagnetic coupling between the pinned layer and pinning layer, which pins the magnetization orientation of the pinned layer.

The introduction of the spin-valve in 1996 by IBM was a major technological breakthrough, which enables the GMR effect to be introduced into commercial magnetic hard disk drives, and is a key factor in the rapid increase of the areal density increase of magnetic hard disk in the late 1990's. However, more recently (circa 2005) the GMR-based read heads have been superseded by those based on another MR effect – the tunneling MR (TMR) effect. TMR based read-heads boast several advantages compared to GMR-based ones, as will be discussed in the next section.

2.2.3 Tunneling Magnetoresistance (TMR)

The tunneling magnetoresistance (TMR) effect was first reported by Julliére [11] in 1975 when the conductance of the Fe/Ge/Pb and Fe/Ge/Co structure was measured with the oxidized semiconductor layer. It is found that the conductance of the structure varies when the relative orientation of the two FM layers varies, i.e., when the two FM layers are parallel to each other, the conductance is higher, while when the two FM layers are antiparallel, the conductance is lower. This effect is called as the TMR effect and the FM/I/FM structure is termed as the magnetic tunneling junctions (MTJ).

While both GMR and TMR effects utilize the resistance difference, which occurs when the relative orientation of the two FM layers changes, the transport mechanism of these two structures is very different. In the TMR effect, the insulating layer is made very thin (typically around 1~2nm) so that electrons can tunnel through the barrier from one FM layer to the other. It is known that when the electrons pass through the first FM layer, it has been spin-polarized along the local magnetization direction. When the magnetizations in these two FM layers are parallel, there is a maximal match between the numbers of occupied states in one FM electrode and available states in the other. Thus, the electron transmission probability across the insulator is maximum and the tunneling resistance is minimum. In the antiparallel configuration, electron tunneling is between majority states in one FM electrode and minority states in the other. This mismatch results in a low tunneling probability and a high tunneling resistance. The basic theory to describe the TMR effect was first proposed by Julliére, who suggested that for each spin direction, the tunneling probability and current is proportional product of the density of states at the

Fermi level of left and right FM electrode. The TMR ratio is given by

$$TMR(\%) = \frac{\Delta R}{R} = \frac{I_{\uparrow\uparrow} - I_{\uparrow\downarrow}}{I_{\uparrow\uparrow}} \times 100\% = \frac{2PP'}{1+PP'} \times 100\% \tag{2.6}$$

where $I_{\uparrow\uparrow}(I_{\uparrow\downarrow})$ represent the current for parallel (antiparallel) configuration, P and P' are the spin-polarization ratio of left and right FM electrodes, which can be defined as

$$P = \frac{N_{\uparrow} - N_{\downarrow}}{N_{\uparrow} + N_{\downarrow}} \qquad P' = \frac{N'_{\uparrow} - N'_{\downarrow}}{N'_{\uparrow} + N'_{\downarrow}} \tag{2.7}$$

where $N_{\uparrow}(N'_{\uparrow})$ and $N_{\downarrow}(N'_{\downarrow})$ are the density of states for spin up (down) electrons at the Fermi level for left (right) FM electrode, respectively. Julliére's model assumes that the spin of electrons is conserved during tunneling process, thus spin-up (down) electron from left FM electrode can only tunnel into spin-up (down) density of states of right FM electrode. It is known that tunneling process is a spin-dependent process, which means that electrons from the left FM electrode have a high probability to tunnel through if its spin direction is parallel to the majority spins of the right FM electrode. Thus the transmission probability is high for parallel configuration and it is low for antiparallel configurations. Although the Julliére's model is a simple phenomenological model, it turns out to be in good agreement with the most experimental results.

The TMR ratio was only less than 1% at room temperature when it was first reported, however with more and more works conducted in this area, the TMR ratio of more than 200% for Fe/MgO/Fe structures [12] and 60% for CoFeB/Al_2O_3/CoFeB structure [13] can be achieved, which make it very attractive for the further application in the magnetic random access memory (MRAM) and magnetic reading head.

2.2.4 Planar Hall Effect

In the normal Hall effect, when an electron flows through a conductor in a magnetic field, the magnetic field exerts a transverse force on the moving electron, which tends to push it to one side of the conductor. This leads to a Hall voltage perpendicular to both the magnetic field and current directions.

If a DC current is applied to a ferromagnetic thin film, the electrical field, which is induced in the film, is not necessarily directed along the current. Due to the anisotropy of the resistivity tensor, there is a considerable electrical field, which can be detected perpendicular to the current of the direction. This transverse electrical field is known as the planar Hall effect (PHE) as opposed to the normal Hall effect, which is directed in the out-of-plane direction. PHE depends on the angles between the magnetization and the direction of the sensing current. [14]

$$V_y = \frac{k I_x}{t} M^2 sin^2(q) sin(2f), \tag{2.8}$$

where t is the thickness of the magnetic layer, I_x is the applied electrical current, f is the angle between the current and in-plane magnetization vector $Msin(q)$. AMR ratio can be expressed as $(\Delta r / r) \propto k M^2 sin^2(q)$, thus PHE is the results of AMR effect. PHE can be employed to determine the contribution of the AMR to the total MR and the magnetization direction of the magnetic film.

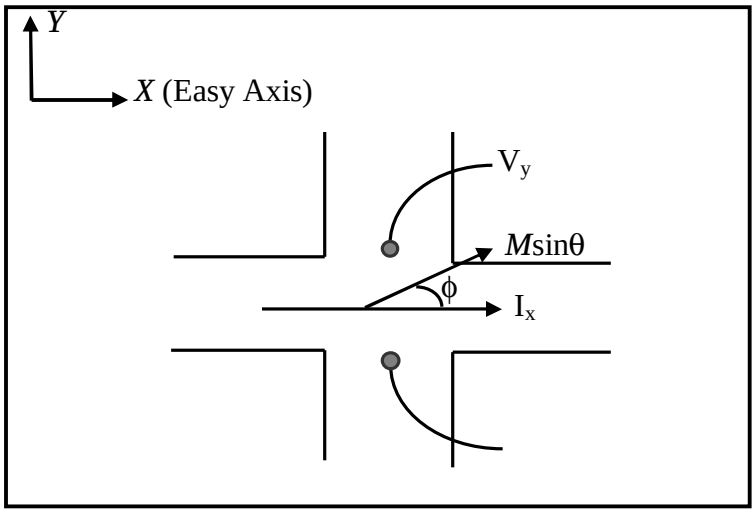

Figure 2.4 Schematic diagram showing the planar Hall effect with the electrical current I_x applied in the x direction and in-plane magnetization *Msinq* in the x-y plane.

2.3 Micromagnetics

In this section the theory of micromagnetic simulation will be discussed, which includes an introduction of the four basic magnetic energy items and the determination of the minimum energy (equilibrium) magnetic state based on the Landau-Lifshitz-Gilbert (LLG) equation. In addition, the mathematical theory and analysis procedure of the finite element method are discussed for its utilization in the electron transport analysis for magnetic patterned media.

2.3.1 Introduction

The most common model to obtain the magnetization configuration in nanoscale magnetic elements is the micromagnetic model. The steady state of spin orientation is determined by the minimization of the total free energy

$$E_{Total} = E_{an} + E_{mag} + E_{ex} + E_{app} \quad (2.9)$$

where E_{an} is the magnetocrystalline anisotropy energy, E_{mag} is the magnetostatic energy, E_{ex} is the exchange energy and E_{app} is the Zeeman energy. These four energy terms are standard in conventional micromagnetics, and the details on them can be obtained in various references [14-17].

The equilibrium magnetization states of elements for static calculations are those that yield a minimum total energy. However these four energy terms play different roles in the determination of the equilibrium state. The magnetocrystalline anisotropy energy tries to align the spins along the crystal lattice orientation, while exchange energy favors parallel alignment of the magnetic momentums, regardless of the direction. The Zeeman energy tends to rotate the magnetization polarization parallel to the external applied magnetic field, and the magnetostatic energy will encourage the formation of closed loops (vortices) in order to avoid the formation of magnetic poles. So the equilibrium state is the minimum energy taking into consideration the competition between these four energy terms.

For example, when there is no applied magnetic field, E_{an}, E_{mag} and E_{ex} will be minimum for a single crystal ferromagnetic sample if all the magnetic momentum align along the crystal easy-axis. However, E_{mag} will not be at its equilibrium due to the appearance of the magnetic free poles at the two ends of the sample. E_{mag} can be reduced by introducing a magnetic domain wall, within which the spins gradually change their directions. However we should note that E_{mag} is reduced at the expense of the increasing of E_{an} and E_{ex}. Therefore a competition between various energy terms is expected, which

will result in a minimum energy state corresponding to the equilibrium energy state of the magnetic materials. There are many numerical methods to minimize the energy with respect to the orientations of individual moments within the sample. In the micromagnetics package we utilize, the equilibrium state is obtained by a magnetization relaxation process governed by the Landau-Lifshitz-Gilbert (LLG) equation, as described in the following section.

2.3.2 Landau-Lifshitz-Gilbert (LLG) Equation

Within the magnetic sample, the magnetic moment at each point is different. To perform the micromagnetic simulation, the ferromagnetic sample has to be first meshed into small unit elements and the magnetization (magnetic moment per unit volume) within each element is assumed to be uniform.

In micromagnetic method, the time evolution of the magnetization of each unit element is controlled by the LLG equation, which is the equation of motion for the magnetization and it is defined as [18,19]

$$\frac{dM}{dt} = -gM \times H_{eff} - \frac{ga}{M_s} M \times (M \times H_{eff}) \tag{2.10}$$

where M is the magnetization(A/M), H_{eff} is the effective field (A/M), $g = ge/2m_e$ is the gyromagneitc ratio(m/(A·s) and g is the Landau factor, which is a material dependent constant). g describes how fast the magnetization M precesses around the effective field H_{eff} and α is the damping coefficient(dimensionless).

The effective field H_{eff} is defined as

$$H_{eff} = -m_0^{-1} \frac{\partial E_{Total}}{\partial M} \tag{2.11}$$

where E_{Total} is the total energy of the sample and has been discussed in Equ. (2.9). $g = ge/2m_e$. Physical materials typically have a damping coefficient α in the range of 0.004-0.15. However, if one is interested in the equilibrium configuration and not the actual magnetization dynamics, a default value of around 0.5 is usually used, which allows the results to converge in a reasonable number of iterations.

On the right-hand side of Equ. (2.10), the first term is a precession term which needs to be included only if we are interested in the time-dependent dynamics M. The second term is the damping term, which is a phenomenological term and causes the magnetization to spiral inwards towards H_{eff} [see Fig 2.5]. If one wants to find the equilibrium state which M settles down after a long time, the damping term is the only one which needs to be considered.

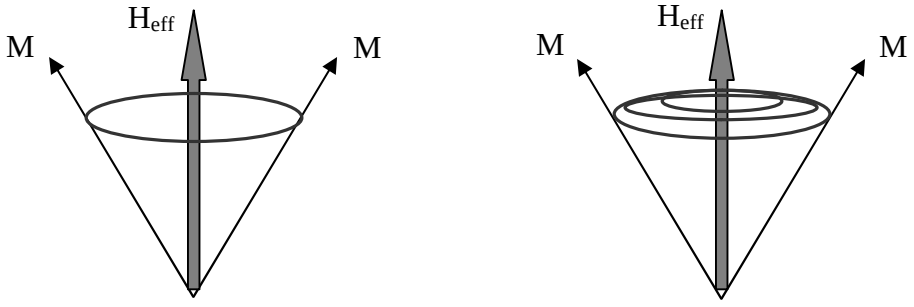

a) undamped precession b) damped precession

Figure 2.5 The precession process of the magnetization M a) without the damping term and b) with the damping term precession.

2.3.3 OOMMF

The simulation software used in this thesis is known as the Object Oriented Micromagnetic Framework (OOMMF) package, which was developed by National Institute of Standards and Technology. The software can be downloaded from http://math.nist.gov/oommf/software.html and the work in this thesis uses version 1.2.0.3 [20].

OOMMF provides a framework for the micromagnetic simulation of the magnetic nanostructure. In its latest version, the script can be used to describe geometries of the magnetic sample, which are essential to build up the model curves instead of straight line in the previous versions. In addition, we can specify the region-defined vector magnetic field and the initial magnetization of the sample could be defined in any configuration via the script. On the other hand, we should also note that this public micromagnetic program has several limitations: it cannot model infinite periodic structures; it becomes too inefficient for samples of large size and complicated geometry; it is limited to zero temperature (no thermal effects), its unit cell size has to be uniform throughout (areal limitation in large samples where rapid magnetization changes occur in a limited area), and there is no way to introduce other contributions to the effective field, e.g. due to spin torque or antiferromagnetic coupling effects.

2.4 Finite Element Analysis

Besides micromagnetics, the thesis also uses the finite element method (FEM) to

model the current distribution within a current-carrying magnetic sample. FEM is based on building a complicated object with simple blocks, or dividing a complicated object into small and manageable pieces. Because of its general applicability, FEM is one of the most widely applied computer simulation methods in engineering. It can be closely integrated with CAD/CAM applications. The main applications of the FEM in engineering are mechanical and civil engineering, structure analysis, thermal /fluid flowing and electromagnetism.

For studying electron transport in patterned magnetic nanostructures, the quantities under consideration are the current density and the electrical potential distribution. To obtain these quantities, electric field analysis was performed. There are many commercial finite element method software packages, such as ANSYS, ABAQUS, ADINA and NISA [21]. In this project, the FEM simulation was performed using the ANSYS program. ANSYS has many finite element analysis capabilities, ranging from a simple, linear, static analysis to a complex, nonlinear, transient dynamic analysis. The next description on the mathematical theory will only concentrate on the electric field analysis.

2.4.1 Mathematical Theory of FEA

Electromagnetic fields are governed by the following Maxwell's equations [22]

$$\nabla \times H = J + \frac{\partial D}{\partial t} \tag{2.12}$$

$$\nabla \times E = -\frac{\partial B}{\partial t} \tag{2.13}$$

$$\nabla \cdot D = r \tag{2.14}$$

$$\nabla \cdot B = D \tag{2.15}$$

And $$D = eE \tag{2.16}$$

$$E = -\nabla j = -\frac{\partial j}{\partial x} i - \frac{\partial j}{\partial y} j \tag{2.17}$$

The Poisson equation is expressed as

$$\nabla^2 j = \frac{\partial^2 j}{\partial^2 x^2} + \frac{\partial^2 j}{\partial^2 y^2} = -r / e \tag{2.18}$$

Where H is magnetic field intensity, D is electric flux density, E is electric field intensity, B is magnetic flux density, J is total current density, ρ is the free charge density and ε is the permitivity constant.

The Poisson equation is solved by the finite element solver with boundary conditions of fixed voltage at one end of the antidot structure. Then the value of E, which is obtained directly from the ANSYS output, is substituted into the Equ. (2.18) to obtain the current density distribution of the whole sample.

$$\mathbf{J} = \sigma \mathbf{E} \tag{2.19}$$

2.5 Transport Analysis with Current in Plane

In recent years, there has been much interest in artificially "engineering" the magnetic properties of thin film magnetic micro- and nanostructures by altering the lateral size and geometry. A prime example is the proposed use of patterned magnetic nanostructures as a possible candidate for ultrahigh density recording media, with areal densities greater than 10 Tbits/in^2. Extensive studies of the size and shape effect of these patterned elements have been carried out involving different materials and geometrical

patterns to achieve well-controlled magnetic and electrical transport properties. In the following sections, we will discuss previous research work on magnetotransport in patterned nanostructures for both CIP and CPP geometry. We will first analyze the transport in the CIP geometry.

2.5.1 Patterned Magnetic Nanostructure

Rapid advances in electron beam lithography techniques make it possible to pattern large numbers of regular single domain magnetic nano-elements which can potentially be used as a recording media in ultra high density storage applications. A lot of research has been carried out on the studies of the size and shape effect on different geometric patterns, e.g. circular and square dots [1,2], fixed width wires [23] and modulated nanowires [3]. The end shape effect of the patterned magnetic nanostructures has also been extensively studies by Kirk *et al.* [24] who investigated the switching field and the reversal behaviour of Co and Permalloy (Py) elements with flat rectangular or triangular pointed ends. They found that it was possible to control the magnetic domain structure and switching field by altering the end shape and the size of the structure.

Among all the patterned magnetic nanostructures, the dot arrays [25,26] with dimensions in the sub-micron or even nanometer size scale constitute one of the most promising candidates for information storage applications. The magnetic dot from 10 to 100 Gb/in^2 has been fabricated [27-29] and later the nanodot array with 400 Gb/in^2 densities [30] has also been achieved using the nanoimprint lithography and lift-off process. In these dot arrays, the magnetic dots are surrounded by a matrix of nonmagnetic material. The inverse system called antidot arrays consisting of thin films with etched

holes or nonmagnetic regions surrounded by a magnetic media have also been proposed as a new candidate for the magnetic media applications. This will be discussed in the next section.

2.5.2 Antidot Array

As shown in Fig 2.6, an antidot array consists of a mesh of holes in a continuous magnetic film. The presence of these antidots (holes) can significantly modify the magnetization configuration and switching properties of the magnetic thin film. This is because the presence of extra air-FM metal surfaces creates artificially induced easy-axis directions parallel to the surfaces. Thus, the magnetization of the interdot regions can be stabilized by the induced anisotropy axis. The detailed magnetization reversal process in antidot array structure is quite interesting and has not been fully analyzed. Besides this, domain wall pinning in engineered defects has also been of long-standing research interest.

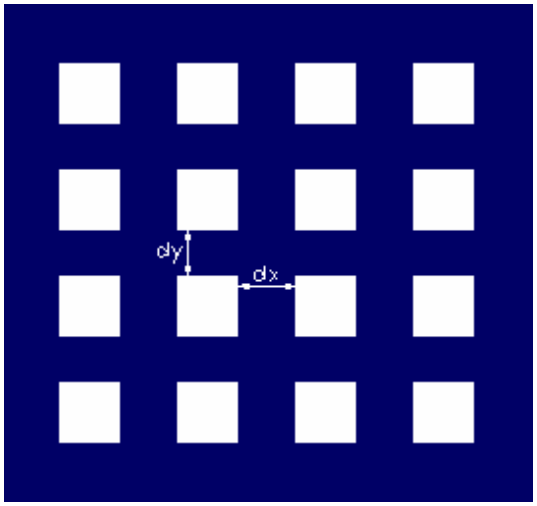

Figure 2.6 Schematic diagram of magnetic thin film with a 4×4 antidot array where *dx* presents the horizontal spacing and *dy* presents the vertical spacing.

Permalloy antidot array was fist reported by Cowburn *et al.* [31] and later considerable experimental and theoretical analysis has been done in investigating its properties. In the experimental studies [32-34], magnetic properties such as the permeability, magnetic domain structure, and M-H hysteresis curves, were investigated as a function of film thickness, and the size and shape of the antidots.

In parallel to these experimental studies, computational micromagnetic analysis has also been performed [35-40] to study its magnetization reversal process. Torres *et al.* [36] studied the remnant state and dependence of the signal to noise ratio to the thickness of the film, antidot size, and dot separation distance. In addition, they also found that the signal to noise ratio decreases dramatically when the separation distance is larger than the dot size [37]. The micromagnetic analysis [38] of the interaction between adjacent bits was also studied and the results showed that the external magnetic field should be carefully controlled to avoid the undesired switching of neighboring bits, in order to achieve 750Gbits/in^2. The antidot arrays of different patterns, such as square rectangular, hexagonal and oblique parallelogram [39] have been investigated and the results confirm the strong dependence of the hard axis and coercivity field on the geometry of the antidots.

2.6 Spin Transport Analysis with Current Perpendicular to Plane

2.6.1 Introduction

In the previous section, we have reviewed the spin transport properties for the structures in the current-in-plane geometry. We now discuss another common configuration for magnetic structures, i.e. multilayers consisting of magnetic and

nonmagnetic layers with current passing in the perpendicular to plane direction. Conventionally the magnetization orientation of a magnetic layer is switched by generating a magnetic field with an externally applied current. However, for small-scale devices, this method has several drawbacks such as relatively high power consumption and risk of cross writing. In recent years, another alternative based on current-induced magnetization switching (CIMS) has received a lot of attention from the research community. Compared to the traditional switching method, CIMS provides a more robust method to switch the magnetization configuration of the magnetic media. It can also lead to simpler device structures by removing the need for an external magnetic field. The concept of spin transfer torque, which is the basis of CIMS, was first introduced by Slonzewski [41] and Berger [42] in 1996. They explained that CIMS originated from the *s-d* exchange interaction between the spin-polarized electrons carrying the current and the local magnetic moments. The *s-d* interaction exerts a torque on the local moments in the magnetic layers. Beyond a certain threshold (critical) current density, the torque becomes strong enough to affect the switching of the magnetization layer. In most of the experimental results, the critical current density to observe the excitation of the magnetization configuration is estimated to be in the range of 10^7 to 10^8 A/cm^2.

Slonzewski and Berger's idea was followed by other researchers and many reports have been published in this area. In the initial experimental studies, high current density is achieved by means of point-contact structures to inject current into a magnetic multilayer structure [43,44]. Subsequent experimental studies focused onto magnetic multilayer structures because of the development of the lithography techniques, which enables the fabrication of multilayers in a nanopillar structure. The current-induced displacements of

Bloch domain walls were first observed on a magnetic thin film, which can be seen as the partial switching of the magnetization configuration [45,46]. Salhi and Berger [45] then reported the current-induced displacement of domain wall in Permalloy films, which was observed by Kerr-contrast microscopy. Gan and Chuang [46] reported the pulsed current induced domain wall propagation in patterned Permalloy strips. The relationship between the direction of the motion and the applied current direction was also discussed.

2.6.2 CIMS Observed in Spin Valve Structure

More recently, the experimental studies on CIMS has concentrated on the reduction of the lateral size of magnetic multilayers in order to obtain complete magnetization switching. Many researchers have reported their observations of complete CIMS in three-layer [tri-layer] Co/Cu/Co [47-50] Co/Cu/Py [51] and Py/Cu/Py [52] spin-valve structures with lateral dimensions of less than 100nm [53-56]. Myers *et al.* [48] measured the statistical properties of the magnetic properties in Co/Cu/Co nanomagnetic structures by a spin-polarized current. They found that the switching near room temperature exhibited the properties of thermally activated escape over an effective barrier. The experimental data showed clearly the magnetic statistical properties of spin-valve structures at room temperature with or without the magnetic field. Ozyilmaz *et al.* [49] studied the current-driven magnetization reversal in low/high magnetic fields in Co/Cu/Co spin-valve nanopillars. The switching properties of the nanopillar at low temperatures were explored with the application of a magnetic field perpendicular to the layers. At low temperature, the probability of the thermal excitation was eliminated, so it can provide us with a clearer environment to observe the magnetization switching process excited by spin-polarized current.

On the other hand, many research groups have also carried out theoretical studies of the mechanism of CIMS [57-65]. There are four important models to explain the mechanism of the current-induced magnetization switching. The first model, known as the spin-transfer model [41,42], stated that the spin-dependent reflection at the paramagnetic/ferromagnetic interfaces transfers transverse angular momentum to the magnetic layer. The spin-transfer model can provide explanations for many experimental results. The second model, proposed by Heide [66], considered only the longitudinal spin accumulation. The spin torque effect generated from the longitudinal spin accumulation acts as an effective exchange field. In the second model, effects from both the forward electrons and the reflected electrons by the metal/ferromagnetic interface were considered, while the spin-transfer model only considered the forward electrons. The third model, as proposed by Zhang and Levy [67], focused on the transverse spin accumulation where the spin-current effect was separated into two items, namely effective field and spin torque. This model can be seen as the further development of spin-transfer model and both of them have a similar expression on the effect of spin torque. Finally, the fourth model proposed by A. Fert ***et al.*** [68] included effects from both the longitudinal and transverse spin accumulation. In this model, the spin torque is proportional to the absorbed transverse spin current, which is composed of two parts, the transverse spin diffusion current generated by the transverse spin accumulation and the transverse component of the applied spin-polarized current. The transverse spin-diffusion current can be much larger than the charge current, while the transverse spin-polarized current is only a fraction of the charge current. The fourth model clearly indicated two ways of maximizing the spin-torque effect, i.e. by increasing the spin polarization ratio and the transverse spin accumulation.

When these theoretical explanations are compared with experimental results, there were some agreements between them [43,44**]**. Both the experimental data and theoretical predictions showed that the critical current density was in the in the range of 10^7 to $10^8 A/cm^2$. However, there were other simulation results that are not in agreement with the experimental results [69]. The second model, which predicted that critical current density is inversely proportional to the thickness of the fixed magnetic layer, was found to be inconsistent with experimental observation. The experimental data for diffusion length of transverse spin accumulation was less than 1.2nm, which was much less than the estimation of the third model. Hence, the theoretical mechanism of the current-induced magnetization switching is an area of research, which needs to be investigated in greater detail.

2.6.3 CIMS Effect in Other Structures

In the previous section, we have focused on current induced magnetization switching in the spin-valve structure, typically Co/Cu/Co multilayers. But recently the scope of CIMS has expanded to encompass other spintronic device structure besides the conventional spin-valve structures.

The first current-induced domain wall switching in a (diluted) ferromagnetic semiconductor structure was reported by H. Ohno's group in Tohoku [70] and subsequently by other researchers [71], where the applied current pulse for switching is of density of only $10^5 A/cm^2$ or less. Although this system has some drawbacks, such as the slow switching speed and the low ferromagnetic transition temperature, it can provide

CIMS with much lower critical current density and is promising for the intergradations of spintronic devices with semiconductor devices.

In August 2004, CIMS was reported in a nanoscale magnetic tunnel junction structure [72] for the first time, and reproducible magnetic switching and the steady-state magnetic precession were observed. In 2006, CIMS was demonstrated in diluted magnetic MTJ [71] and recently it is reported that CIMS was achieved in nanopillars with perpendicular anisotropy [73]. This is especially significant for the application of CIMS in data storage application, since perpendicular recording is gradually replacing the traditional longitudinal recording technology. The critical current in these junctions is observed to be comparable to those for normal spin-valve nanopillars, which indicated the robust and efficient spin transport process within the barriers. This development is especially encouraging in view of the higher MR ratio achieved in MTJs as compared to spin valve multilayers, which augurs well for the development of the CIMS-based MTJ in MRAM applications.

On the theoretical side, Berger [74] has proposed a different configuration where the thin free layer is sandwiched between two thick pinned magnetic layers with opposite magnetic orientations, which is named as asymmetric spin valve. His theoretical analysis indicated that both interface of the free magnetic layers are active to generate spin torque, which can potentially result in a reduction of the critical current density. Recently, the conclusions from this model were confirmation experimentally by a research group from Cornell University and they concluded that the critical current density can be reduced to the order of 10^6 A/cm^2 [75].

References

[1] C. Mathieu ***et al.***, Appl. Phys. Lett. 70, pp.2912-2914. 1997.

[2] A. Maeda, M. Kume, T. Ogura, K. Kuroki, T. Yamada, M. Nishikawa, and Y. Harada, J. Appl. Phys.76, pp.6667-6670. 1994.

[3] C. C. Yao, D. G. Hasko, Y. B. Xu, W. Y. Lee, and J. A. C. Bland, J. Appl. Phys. 85, pp.1689-1692. 1999.

[4] C. A. Ross, M. Farhoud, M. Hwang, H. I. Smith, M. Redjdal, F. B. Humphrey, J. Appl. Phys. 89, pp.1310-1319. 2001.

[5] P. M. Levy, J. Magn, Magn, Mater, 140, pp.485-487. 1995.

[6] Shan X. Wang and Alexander M.Taratorin, Magnetic Information Storage Technology. pp.123-133, Boston : Academic Press. c1998.

[7] P. Grnberg, R, Schreiber, Y. Pang, M. B. Brodsky and C. H. Sowers, Phys, Rev. Lett., 57, pp.2442-2445. 1986.

[8] M. N. Baibich, I. M. Broto, A, Fert, F. Nguyen, Van Dau, F. Petroff, P. Eitenne, G. Creuzet, A. Friederich and J. Chazelas, Phys. Rev. Lett.,61, pp.2472-2475. 1988.

[9] Robert. L. White, IEEE Trans on Magn., 28, pp.2482, 1992.

[10]A. Barthélémy, A. Fert and F. Petroff, Giant Magnetoresistance in Magnetic Multilayers. In Handbook of Magnetic Materials, vol, 12, ed, by K.H.J. Buschow, pp.19-20. Amsterdam: Elsevier Science. 1999.

[11] M. Julliére, Phys. Lett.,54A, pp.225. 1975.

[12] S. Yuasa, T. Nagahama, A. Fukushima, Y, Suzuki and K. Ando, Nature Materials, 3, pp.868-871. 2004.

[13] D. Wang, C. Nordman, J. M. Daughton, Z. Qian, and J. Fink, IEEE Trans. Magn. 40, No. 4, 2269–2271. 2004.

[14] Robert C. O'Handley. Modern Magnetic Materials, pp.567-584, New York: Wiley. 1999.

[15] Sōshin Chikazumi, Physics of Ferromagnetism, Oxford: Clarendon Press; New York: Oxford University Press, 1997.

[16] Derek Craik, Magnetism: principles and applications, Chichester; New York: Wiley, c1995.

[17] J. P. Jakubovics, Magnetism and Magnetic Materials, London: Institute of Materials, 1994.

[18] L. Landau and E. Lifshitz, Physik. Z. Sowjetunion, 8, pp.153-169. 1935.

[19] T. L. Gilbert, Phys. Rev.100, pp.1243. 1955.

[20] M. J. Donahue and D. G. Porter <URL: http://math.nist.gov/oommf/>.

[21] Brebbia, C. A. Finite Element System: a handbook, pp.3-16, Berlin: Springer-Verlag. 1985.

[22] Zienkiewicz, O. C. The Finite Element Method in Engineering Science, pp.423-449, London, New York, McGraw-Hill. 1971.

[23] A. O. Adeyeye, G. Lauhoff, J. A. C. Bland, C. Daboo, D. G. Hasko, and H. Ahmed, Appl. Phys. Lett. 70, pp.1046-1048. 1997.

[24] K. J. Kirk, J. N. Chapman, and C. D. W. Wilkinson, Appl. Phys. Lett. 71, pp.539-541.1997.

[25] R. P Cowburn, D. K. Koltsov, A. O. Adeyeye, M. E. Welland, and D. M. Tricker, Phys. Rev. Lett. 83, pp.1042-1045. 1999.

[26] T. Pokhil, D. Song, and J. Nowak, J. Appl. Phys. 87, pp.6319-632. 2000.

[27] B. D. Terris, H. J. Mamin and D. Rugar, 1996 EIPBN, Atlanta, GA, 1996.

[28] B. D. Terris, H. J. Mamin, M. E. Best, J. A. Logan, D. Rugar and S. A. Rishton, Appl. Phys. Lett. 69, pp.4262-4264. 1996.

[29] S. Y. Chou, M. S. Wei, P. R. Krauss and P. B. Fisher, J. Appl. Phys. 76, pp.6673-6675. 1994.

[30] Peter R. Krauss and Stephen Y. Chou, Appl. Phys. Lett, 71, pp.3174-3176, 1997.

[31] R. P. Cowburn, A. O. Adeyeye, and J. A. C. Bland. Apply. Phys. Lett. 70, pp.2309-2311.1997.

[32] C. T. Yu, H. Jiang, L. Shen, P. J. Flanders and G. J. Mankey, J. Appl. Phys. 87, pp.6322-6324. 2000.

[33] A. Yu, Toporov, R. M. Langford, and A. K. Petford-Long, Appl. Phys. Lett. 77, pp.3063-3065. 2000.

[34]C. A.Grimes, P. L. Trouilloud, J. K. Lumpp and G. C. Bush, J. Appl. Phys. 81, pp.4720-4722. 1997.

[35] N. Dao, S. L. Whittenburg and R. P. Cowburn, J. Appl. Phys. 90, pp.5235-5237. 2001.

[36] L.Torres, L. Lopez-Diaz, and J. Iñiguez, Appl. Phys. Lett. 73, pp.3766-3768. 1998.

[37] L.Torres, L. López-Díaz, O. Alejos, and J. Iñiguez, J. Appl. Phys. 85, pp.6208-6210. 1999.

[38] L. Torres, L. Lopez-Diaz and O. Alejos, J. Appl. Phys. 87, pp.5645-5647. 2000.

[39] P. Vavassori, G. Gubbiotti, G. Zangari, C. T. Yu, H. Yin, H. Jiang and G. J. Mankey, J. Appl. Phys. 91, pp.7992-7994. 2002.

[40] M. B. A. Jalil, S. L. A. Phoa, S. L. Tan and A. O. Adeyeye, IEEE, Trans. Magn, 38(5), pp.2556-2558. 2002.

[41] J. C. Slonczewski, J. Magn. Magn. Mater., 159, pp.L1-L7. 1996.

[42] L. Berger, Phys. Rev. B, 54, pp.9353-9358. 1996.

[43] E. B. Myers *et al.*, Science, 285, pp.867-870. 1999.

[44] M.Tsoi *et al.*, Phys. Rev. Lett., 80, pp.4281-4284. 1998.

[45] E. Salhi and L. Berger, J. Appl. Phys., 76, pp.4787-4792. 1994.

[46] L. Gan, S. H. Chung, K. H. Aschenbach, M. Dreyer and R. D. Gomez, IEEE Trans. Magn. 36, No. 5, pp.3047-3049. 2000.

[47] Derek. Kelly *et al.,* Phys. Rev. B, 68, pp.134425. 2003.

[48] E. M. Myers *et al.,* Phys. Rev. Lett., 89, pp.196801. 2002.

[49] B.Ozyilmaz *et al.,* Phys. Rev. Lett., 91, pp.067203. 2003.

[50] A. Fábián, C. Terrier, S. Serrano Guisan, X. Hoffer, M. Dubey, L. Gravier, and J.-Ph. Ansermet and J.-E.Wegrowe, Phys. Rev. Lett. 91, pp.257209. 2003.

[51] S. I. Kiselev, J. C. Sankey, I. N. Krivorotov, N. C. Emley, M. Rinkoski, C. Perez, R. A. Buhrman and D. C. Ralph, Phys. Rev. Lett., 93, pp.036601. 2004.

[52] S. Urazhdin, Norman O. Birge, W. P. Pratt, Jr., and J. Bass, Phys. Rev. Lett., 91, pp.146803. 2003.

[53] M. Covington, M. AlHajDarwish, Y. Ding, N. J. Gokemeijer, and M. A. Seigler. Phys. Rev. B, 69, pp.184406. 2004.

[54] S.Urazhdin, NO. Birge, W. P. Pratt, J. Bass, Appl. Phys Lett., 84 (9), pp.1516-1518. 2004.

[55] Urazhdin S, Birge NO, Pratt WP, Bass J. J. Appl. Phys. 95 (11), pp.7429-7434 Part 2. 2004.

[56] A. Deac, K. J. Lee, Y. Liu, O. Redon, M. Li, P. Wang, J. P. Nozières, and B. Dieny, Phys. Rev. B, 73, pp.064414. 2006.

[57] M. Di Ventra, Y.-C. Chen and T. N. Todorov. Phys. Rev. Lett. 92, pp.176803. 2004.

[58] M. D. Stiles and Jiang Xiao and A. Zangwill. Phys. Rev. B, 69, pp.054408. 2004.

[59] M. B. Jalil and S. G. Tan, Phys. Rev. B, 72, pp.214417. 2005.

[60] J. Barnaś, A. Fert, M. Gmitra, I. Weymann, and V. K. Dugaev, Phys. Rev. B, 72, pp. 024426. 2005.

[61] J. Zhang, P. M. Levy, S. Zhang, and V. Antropov, Phys. Rev. Lett., 93, pp.256602. 2004.

[62] A. Manchon and J. C. Slonczewski, Phys. Rev. B, 73, pp.184419. 2006.

[63] J Xiao, A. Zangwill, and M. D. Stiles, Phys. Rev. B, 73, pp.054428. 2006.

[64] L. Joly, J. K. Ha, M. Alouani, J. Kortus, and W. Weber, Phys. Rev. Lett. 96, pp. 137206. 2006.

[65] M. Gmitra, J. Barnaś, A. Fert, I. Weymann and V. K. Dugaev, Phys. Stat. Sol. (c) 3, pp.97. 2006.

[66] C. Heide, P. E. Zilberman and R. J. Elliott, Phys. Rev. B, 63, pp.064424. 2001.

[67] S. Zhang, P. M. Levy and A. Fert, Phys. Rev. Lett., 88, pp.236601. 2002; A. Shpiro, P. M. Levy and S. Zhang. Phys. Rev. B, 67, pp.104430. 2003.

[68] A. Fert *et al.*, J. Magn. Magn. Mater., 272-276, pp.1706-1711. 2003.

[69] F. J. Albert, *et al*., Phys. Rev. Lett., 89, pp.226802. 2002.

[70] M. Yamanouchi, D. Chiba, F. Matsukura, H. Ohno, Nature 428 (6982): pp.539-542. 2004.

[71] M. Elsen, O. Boulle, J.-M. George, H. Jaffrès, R. Mattana, V. Cros, A. Fert, A. Lemaitre, R. Giraud, and G. Faini, Phys. Rev. B, 73, pp.035303. 2006.

[72] G. D. Fuchs, N.C. Emley, I. N. Krivorotov, P. M. Braganca, E. M. Ryan, S. I. Kiselev, J. C. Sankey, D. C. Ralph and R. A. Buhrman, Appl. Phys. Lett, 85, pp.1205-1207. 2004.

[73] S. Mangin, D. Ravelosona, J. A. Katine, M. J. Carey, B. D. Terris, Eric E. Fullerton, Nature Materials 5, pp.210. 2006.

[74] L. Berger, J. Appl. Lett. 93, pp.7693-7695. 2003.

[75] G. D. Fuchs, I. N. Krivorotov, P. M. Braganca, N. C. Emley, A. G. F. Garcia, D. C. Ralph, and R. A. Buhrman, Appl. Phys. Lett, 86, pp.152509. 2005.

Chapter 3 Transport and Recording Properties Modeling of the Magnetic Antidot Array

3.1 Introduction

After reviewing the electromagnetic properties of some nanomagnetic structures and studying the transport and micromagnetic analysis method in Chapter 2, we focus our study in this chapter, on the lateral transport and magnetic recording properties of $Ni_{80}Fe_{20}$ [also known as Permalloy (Py)] film, which is etched into a 2-dimensional antidot array.

The antidot array is a type of patterned magnetic media, which was first proposed in 1997. Since then, extensive experimental and theoretical analysis has been done to investigate its magnetic and transport properties such as permeability, magnetic domain structure, remanent states and signal to noise ratio. The detailed review of these works has been presented in section 2.5 of chapter 2. Thus in this chapter, we will present our own work on the theoretical analysis of the lateral transport properties and magnetic recording properties of magnetic antidot array.

We first focus on the lateral magnetotransport properties across a ferromagnetic antidot array structure. This is modeled by numerically solving the inhomogeneous current density distribution **j** and magnetization **M** configuration, under the influence of an external magnetic field. Subsequently, the overall anisotrophy magnetoresistance (AMR) of the structure is evaluated by a linear interpolation of **M** and **j** across the sample. The

main result of the investigations is that the AMR behavior is significantly influenced by the film geometry such as the antidot spacing and the aspect ratio.

Next, we investigated the magnetic reversal process of the antidot array structure. Initially such a patterned structure has been proposed as a potential candidate for ultra-high density storage, in which discrete magnetically-hard regions can act as individual storage bits. However, given the rapid progress in magnetic recording media technology, which has yielded areal density well in excess of 100 Gb/in^2 (in the case of the latest perpendicular media technology), it is increasingly unlikely that patterned antidot arrays can emerge as a viable alternative in its present form. However, from the research perspective, it is useful to analyze the magnetic reversal process in an antidot array, since it provides a controlled environment to study e.g. the interaction between a domain wall and geometrical features such as surfaces and constrictions. It is also useful to study the magnetic reversal of discrete regions, and how geometry affects the quality of the reversal process. Thus, in the second part of this chapter, a micromagnetic simulation was performed to study the magnetic reversal and recording quality of the Py antidot array. A Karlqvist head field is applied to a single bit region to reverse its magnetization. The detailed magnetization reversal within the sample was displayed. The recording quality is quantified by the reciprocal of noise and contrast ratio as well. Our simulation results show that the magnetization reversal properties can be altered by the presence of the antidot array and its geometry. The recording quality can be improved significantly by optimizing the bit aspect ratio.

3.2 Transport and Micromagnetic Modeling of Antidot Array

3.2.1 Introduction

Anisotropy magnetoresistance (AMR) is one of the most important electromagnetic properties for both continuous magnetic thin films and patterned media. It has been extensively studied and widely used in magnetic sensing devices [1,2] and readout heads [3] in magnetic recording systems. Ferromagnetic (FM) materials like Co and Permalloy (Py) exhibit an intrinsic AMR behavior due to the anisotropy scattering of conduction electrons by spin-orbit interaction [4]. In submicron structures, the AMR property may be tailored externally by modifying the lateral geometry. Previous studies have been performed on different geometric structures, e.g. antidot arrays [5,6], nanowire arrays [7] and modulated nanowire [8], to investigate the effect of geometry on the transport and magnetic behavior of a FM material.

In the existing model used to calculate the AMR, the current density **j** is assumed to be parallel to the applied electric field direction [9]. This could be valid for conduction within a uniform bulk film. However, for nanostructured magnetic films and wires, the current direction is constrained by the geometry to flow inhomogenously. In this chapter, we present a transport model to obtain this nonuniform current density distribution in the Permalloy antidot array while taking into consideration the influencing geometry and planar and normal Hall effects. The AMR responses obtained from different antidot film geometries is presented and explained as well.

3.2.2 The Transport Model

In general, the anisotropy magnetoresistance of magnetic materials, is expressed as

$$r(q) = r_0 + \Delta r \cos^2 q \tag{3.1}$$

where q is the angle the magnetization **M** makes with the direction of current **j**. To evaluate q, we need to evaluate **M** and **j** throughout the sample.

3.2.2.1 Magnetization Calculation via OOMMF

The magnetization **M** is obtained by micromagnetic simulation using the OOMMF software from NIST [10]. The film with a 4×4 antidot array, shown in Fig 3.1, is first meshed into 3D cubic cells (10 nm×10 nm×10 nm). The equilibrium magnetization is then obtained by iteration using the Landau-Lifshitz-Gilbert equation, until the residual torque in each cell falls below 10^{-5} $\mathbf{M} \times \mathbf{H}_{\text{eff}}$, where $\mathbf{H}_{\text{eff}}$ is the effective field [11]. The applied magnetic field is varied from 1000 mT to −1000 mT, and vice versa in x-direction. The arrow plot of the magnetization distribution at different applied fields is shown in Fig 3.1. The remanent state (0 mT), where the magnetization in the horizontal interdot regions is strongly aligned along the field direction, is in agreement with the previous work [12].

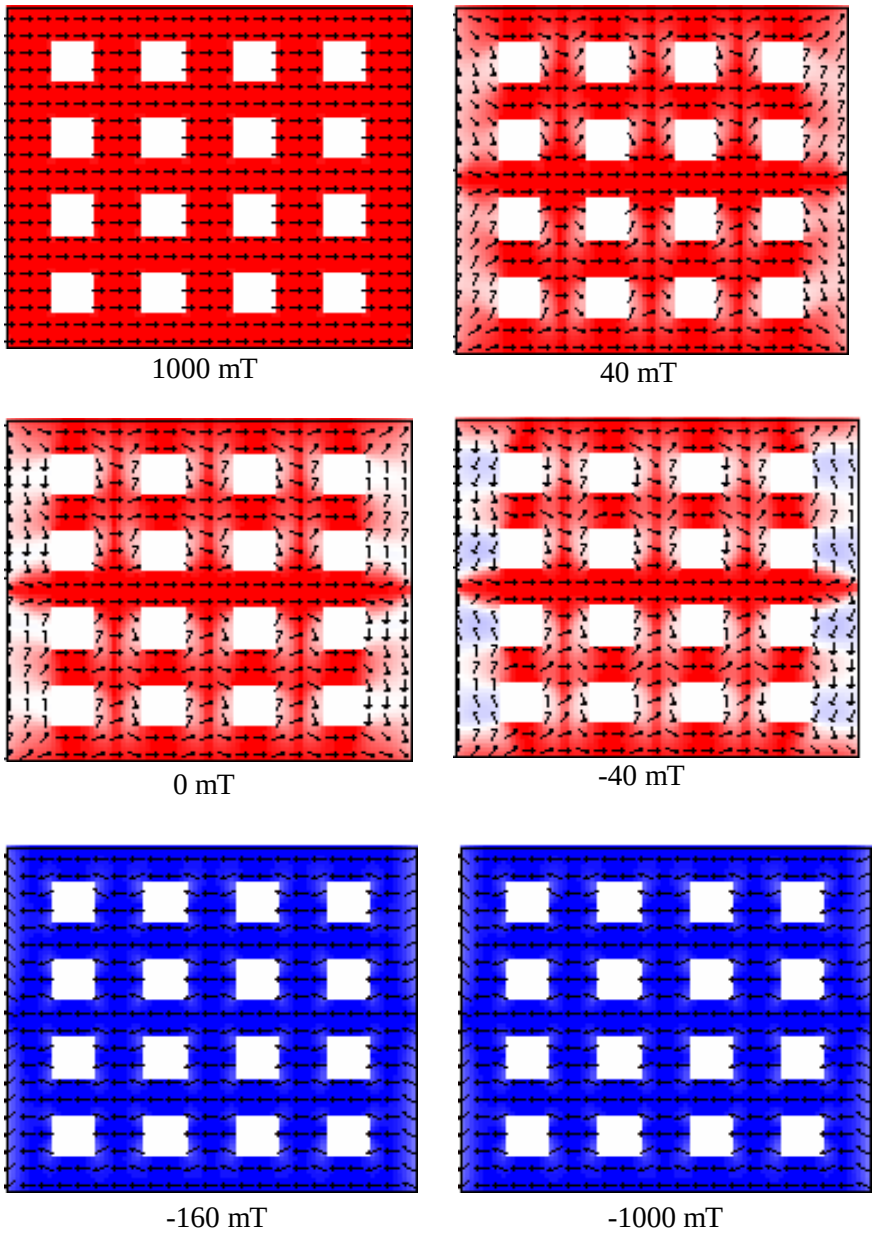

Figure 3.1 The magnetization configurations of the Permalloy antidot array with dx=100 nm, dy=80 nm and antidot size = 100 nm×100 nm×20 nm at different applied magnetic fields along the *x* direction, obtained from OOMMF micromagnetic simulations.

3.2.2.2 Calculation of Current Density Distribution Using Ansys

The current density distribution **j** is first estimated numerically when a d.c. current of 1 mA is passed in the *x* direction, in the absence of **B** field. This is done by solving the

Poisson equation, using the ANSYS finite element software [13] and based on tetrahedral meshing as shown in Fig 3.2. The details of this calculation are described as follows. The ANSYS Preference is set to Electromagnetic-Electric option, which is appropriate to the current density calculation that we are interested in (i.e. solving the Poisson equation). This ensures that the element types needed for our analysis will be available, since the GUI filters element types are based on the chosen preference.

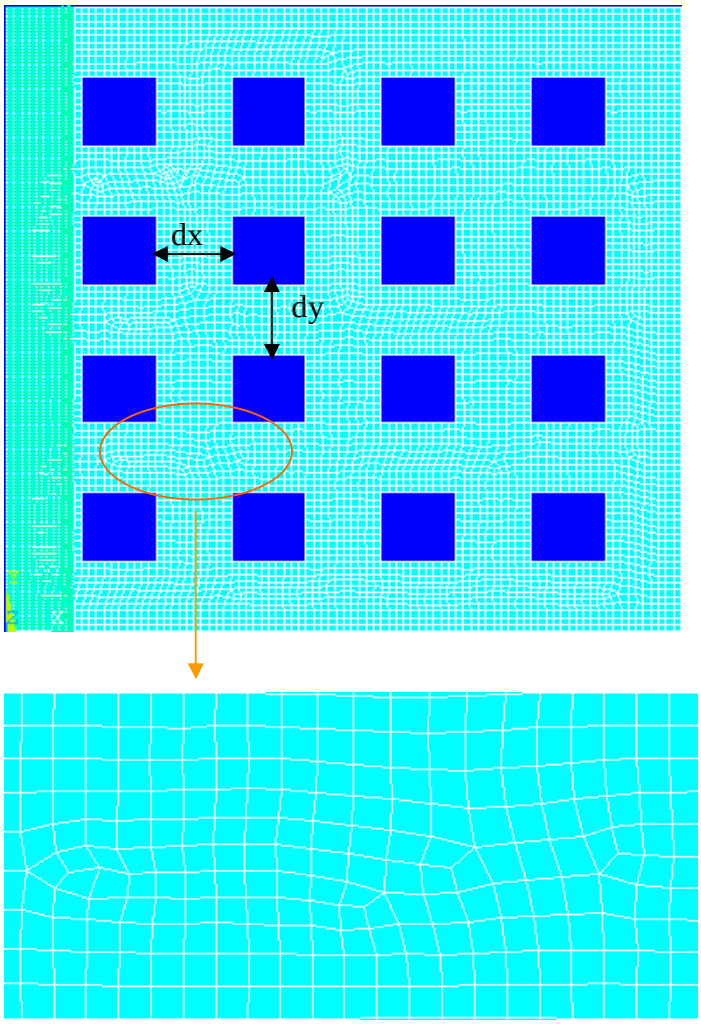

Figure 3.2 (Upper) The antidot array is meshed with tetrahedral cell, with the current applied on the left end of the element, and the right end of the element is constrained to zero voltage. The antidot size is 100 nm×100 nm×20 nm with dx=100 nm, dy=100 nm. (Bottom) The enlarged diagram of the tetrahedral meshing in one part of above figure, indicated by the orange circle.

ANSYS Preprocessor steps

To input the geometric data of our model (a Py antidot structure with horizontal interdot spacing dx=100 nm and vertical interdot spacing dy=80 nm, we first create a rectangle with a width of 900 nm and a height of 800 nm, which encompasses the whole sample. Next, a 4×4 array of holes is defined, and then subtracted from the rectangular Py film created earlier. The dimensions are expressed in nanometers when the model is being created. For the transport analysis, the thin film is modeled with PLANE67, in which each element consists of a 2-D four-node electrical conduction element.

Having defined the geometry of our model, the next step is to input the material parameters, and here only one parameter needs to be defined, i.e. r = electrical resistivity of the antidot film material- Permalloy. This is inputted as a temperature-independent and isotropic constant, with a numerical value of 1.156×10^{-7} (Ωm)[14].

The model is then meshed, with the mesh element size set at 10 nm, and the mesh element shape chosen to be quadrilateral. When the magnetization is simulated by micromagnetic OOMMF software, the model is also divided into many finite-element cells. However, due to the limitation of OOMMF, these elements have to be cubic in shape, with dimensions of 5-10 nm.

ANSYS Solution Steps

After defining the geometry, material, and meshing of the sample, we are now ready to solve the Poisson equation. For the analysis type, we selected the steady-state analysis, since we are interested only in the equilibrium current density distribution under DC condition, and not on any AC or transient effects. The Frontal Solver is selected as the equation solver, and a d.c. current of 1 mA is applied along the horizontal direction from left to right across the sample. This current load is specified on every finite-element node on the left end of the model and is applied as an electrical excitation. For the boundary conditions, a typical approach is to specify a zero voltage at one end of the conductor. We thus constrain the voltage to be zero at the right end of the model shown in Fig 3.2.

ANSYS General Postprocessing Steps

After the calculations have been performed, the relevant results are viewed in the post-processing stage. The current density distribution is most effectively depicted using the vector display mode. The vector arrows in the figure depict the flux and gradient of the electric field, which gives us an indication of the concentration of current between the antidots [Fig 3.3(a)]. The contour plot of the electrostatic potential across the sample can also be plotted [Fig 3.3(b)]. The magnitude of the potential gradient ∇f however is fairly constant in the horizontal direction across the sample, despite the presence of the antidots.

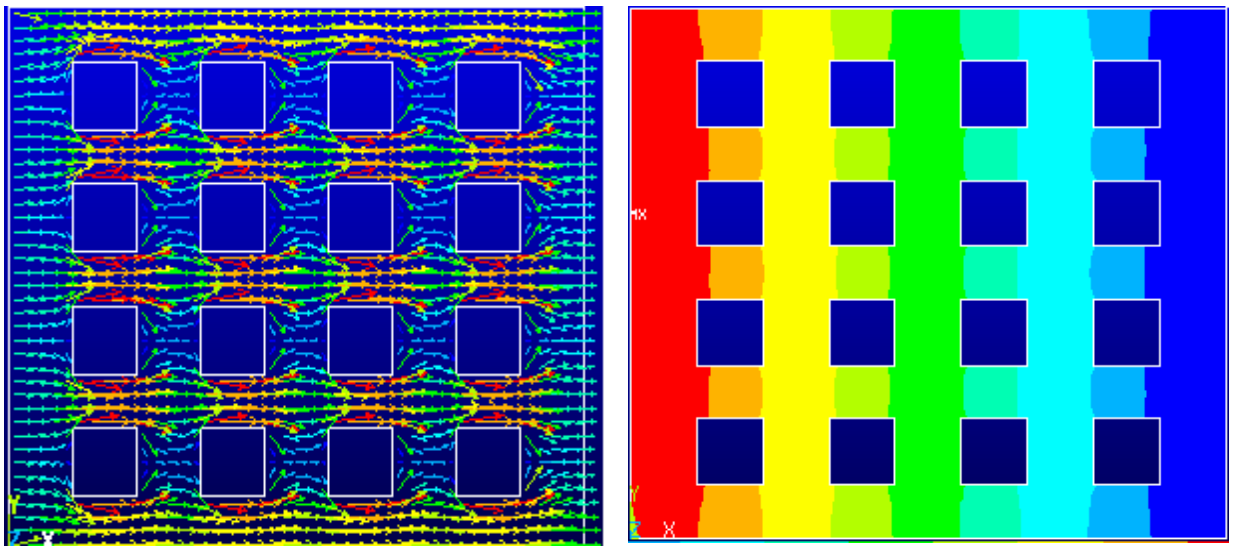

(a) (b)

Figure 3.3 (a) Simulated current density distribution and (b) contour plot of the electrostatic potential in the absence of B in a Py film with a 4×4 antidot array with square-shaped dot width size of 100 nm and separation distances, dx=100 nm and dy=80 nm. The arrow indicates the magnitude and direction of current.

3.2.2.3 Linear Interpolation of j and M

We have thus calculated the current density **j** distribution at every node in the absence of an applied **H** field. The next step is to combine the **j** distribution with that of magnetization **M** in order to obtain the divergence *q* between the two vectors at all points on the sample. Thus, **j** has to be interpolated within each element based on the nodal values, by using appropriate linear shape functions. We first assume that the potential varies linearly in the *x* and *y* direction as such:

$$V_e(x, y) = a + bx + cy + dxy \tag{3.2}$$

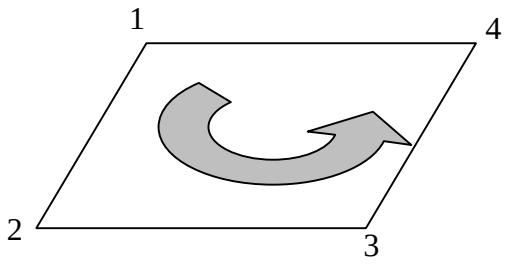

Figure 3.4 Schematic plot of quadrilateral element with the 4 node numbering 1-2-3-4 proceeding counterclockwise.

within a particular quadrilateral element labeled *e*. The constants *a*, *b*, *c*, and *d* are to be determined. Consider a quadrilateral element with the 4 node numbering 1-2-3-4 proceeding counterclockwise (as shown in Fig 3.4). The current density distribution at the nodes 1, 2, 3 and 4 could be obtained using the following equations:

$$\begin{bmatrix} j_1 \\ j_2 \\ j_3 \\ j_4 \end{bmatrix} = \begin{bmatrix} 1, x_1, y_1, x_1 y_1 \\ 1, x_2, y_2, x_2 y_2 \\ 1, x_3, y_3, x_3 y_3 \\ 1, x_4, y_4, x_4 y_4 \end{bmatrix} \begin{bmatrix} a \\ b \\ c \\ d \end{bmatrix} \tag{3.3}$$

where j_k for k = 1 to 4 are the nodal values given by our earlier ANSYS calculations. The coefficients *a*, *b*, *c* and *d* are then given by

$$\begin{bmatrix} a \\ b \\ c \\ d \end{bmatrix} = \begin{bmatrix} 1, x_1, y_1, x_1 y_1 \\ 1, x_2, y_2, x_2 y_2 \\ 1, x_3, y_3, x_3 y_3 \\ 1, x_4, y_4, x_4 y_4 \end{bmatrix}^{-1} \begin{bmatrix} j_1 \\ j_2 \\ j_3 \\ j_4 \end{bmatrix} \tag{3.4}$$

Substituting these constants into Equ. (3.2), we obtain the value **j** at all (x, y) points within element *e*. The above is repeated for all quadrilateral elements. Thus, to obtain an interpolated **j** value at any point (x, y), we identify which element e_0 the point belongs to (this is quite straightforward given that all elements are convex), and apply Equ. (3.2) with *a*, *b*, *c* and *d* values corresponding to e_0.

From OOMMF and ANSYS, we have got the value of **M** and **j** at the center of the each cell. The discrete solutions of **M** and **j** are then interpolated throughout the sample using linear shape functions, following a similar procedure as outlined above.

3.2.2.4 Incorporating the Magnetic Field B into j

The current, which was obtained from ANSYS consists only of the ohmic component. It is well known that the **j** is modified in the presence of a **B** field due to the planar and normal Hall effects. To incorporate these effects on the current direction, we note that the current density vector **j** is given as

$$\mathbf{j} = 2Q\mathbf{v} = 2Qm\mathbf{E} \tag{3.5}$$

where Q, μ, **v** and **E** are the carrier charge density, mobility, steady-state drift velocity and electric field in the specimen, respectively. In the presence of a magnetic flux density **B,** Equ. (3.5) becomes [15]

$$\mathbf{j}=2Q\mu\,\mathbf{E}+f\,(\mathbf{E}\times\mathbf{B})+g\,(\mathbf{E}\times\mathbf{B})\times\mathbf{B} \tag{3.6}$$

where

$$\mathbf{B}=m_0(\mathbf{H}+\mathbf{M}) \tag{3.7}$$

$$f=\frac{2Qm^2}{1+(mB)^2} \qquad g=\frac{2Qm^3}{1+(mB)^2} \tag{3.8}$$

In Equ. (3.7), m_0 is the permeability of the medium, and **H** the applied magnetic field. The first term of Equ. (3.6) corresponds to the ohmic term, while the second and third terms are the normal and planar Hall effect terms. Equ. (3.6) can be inverted so as to express electric field **E** as a function of the current density **j** and magnetic flux density **B**, i.e.

$$\mathbf{E}=\frac{1}{2Qm}\mathbf{j}-\frac{1}{2Q}(\mathbf{j}\times\mathbf{B}) \tag{3.9}$$

Starting from the current $\mathbf{j}_0$ and $\mathbf{E}_0$ in the absence of **B** field, the galvanomagnetic Hall effects on **j** and **E** are then incorporated through a self-consistency scheme. Equs. (3.6) and (3.9) are first rewritten as

$$\mathbf{j}=2Q\mu\,\mathbf{E} + f\,(\mathbf{E}\times\mathbf{B})+ g\,(\mathbf{E}\times\mathbf{B})\times\mathbf{B} = \mathbf{j}_0+[\Delta\sigma]\cdot\mathbf{E} \qquad (3.10)$$

$$\mathbf{E}=\frac{1}{2Qm}\mathbf{j}-\frac{1}{2Q}(\mathbf{j}\times\mathbf{B}) = \mathbf{E}_0+[\Delta\rho]\cdot\mathbf{j} \qquad (3.11)$$

where the galvanometric effects on **j** and **E** have been combined into matrices $[\Delta\sigma]$ and $[\Delta r\,]$. Subsequently, the values of **j** and **E** are obtained via iteration using the following relations:

$$\mathbf{E}_n= \mathbf{E}_0+[\Delta\rho]\cdot\mathbf{j}_{n-1} \qquad (3.12)$$

$$\mathbf{j}_n= \mathbf{j}_0+[\Delta\sigma]\cdot\mathbf{E}_{n-1} \qquad (3.13)$$

The iteration is continued until the **E** and **j** converge, that is the difference between successive values of **E** and **j** is within 1% of the previous values. The modified current density distribution **j** is then interpolated using linear shape functions and normalized. Based on the converged current density **j**, we then determine the current paths throughout the film.

3.2.3 Magnetoresistance Calculation

Since the current distribution through the sample is non-uniform, it is strictly not accurate to obtain the magnetoresistance (MR) by dividing the sample into equal parallel strips, and combining the parallel resistances associated with each strip. We now discuss a more refined model to obtain the MR in the presence of non-uniform **j**. The source (left) end of the film is divided into (say) 100 segments, and the middle of each segment is

regarded as the starting point of each path. From these initial points, an individual current path is traced out by a series of ministeps of length $\Delta x << L_{x,}$ where L_x is the width of the sample. The direction of each ministep is given by the normalized **j** its starting point. If a ministep happens to end within an antidot, then the path is rendered invalid. Current is constrained to flow along the antidot edge instead. In this way a path is drawn until it reaches the drain (right) boundary of the film. Note that the paths will not cross or meet, because there are no sources or sinks of current within the film. Due to the symmetry of the film in the $\pm x$ direction, the y-position of the start and end points of each current path should coincide. If they differ by greater than a preset tolerance, then the current path tracing is repeated with the endpoint of the previous iteration being used as the start point of the next. Figure 3.5 shows the 100 current paths after convergence.

To calculate the magnetoresistance, we obtain the angle q between **j** and **M** at the start of each ministep of each path. Each current path can be regarded as a series of cells, whose resistance is

$$R_{cell} = r\left(q_{\text{cell}}\right)\Delta x/\left(\Delta y_{\text{cell}} \times t\right) \tag{3.14}$$

where y_{cell} is the cell thickness in the y-direction, and is given by half the distance to the adjacent current paths. The total resistance is then computed as the parallel combination of the resistances of all paths:

$$R_{\text{tot}}^{-1} = \sum_{\text{paths}} \left[\sum_{\text{cells}} R_{\text{cell}} \right]^{-1} \tag{3.15}$$

The overall AMR results of Fig 3.6 are obtained by calculating R_{tot}^{-1} at different field H values from positive to negative saturation, and vice versa. In our calculations, we

assumed the numerical values of the parameters r_0 and $(\Delta r / r_0)$ of Py to be 1.156×10^{-7} (Ωcm) and 3.5%, respectively [14]. Besides the absolute values of the AMR ratio, we will also focus on the shape of the AMR response, as this will show how the magnetotransport is correlated to the magnetic reversal process.

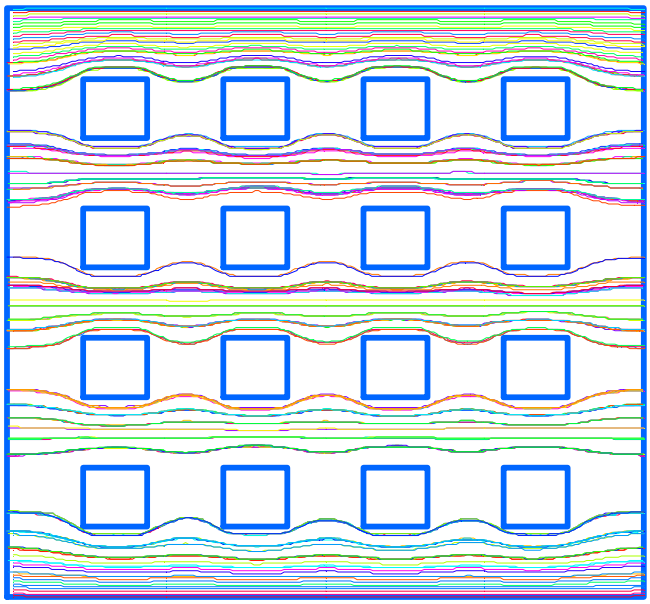

Figure 3.5 The self-consistent calculated current paths in the antidot array with dx=100 nm and dy=100 nm and dot size=100 nm ×100 nm ×20 nm.

3.2.4 Results and Discussion

The current density distribution of the antidot array is calculated for different horizontal interdot spacing (dx) and vertical interdot spacing (dy). Fig 3.3(a) shows the inhomogeneous current density distribution in the antidot array with dx=100 nm and dy=80 nm. We can see clearly that the current density distribution **j** is not parallel to the applied current direction due to the influence of the antidots. Fig 3.5 shows the current paths after incorporating the galvanomagnetic effects. Most of the current is confined to

the horizontal segments of the film between the antidots, with very little current in the vertical segment. Thus there is very little coupling between current flow in adjacent horizontal segments.

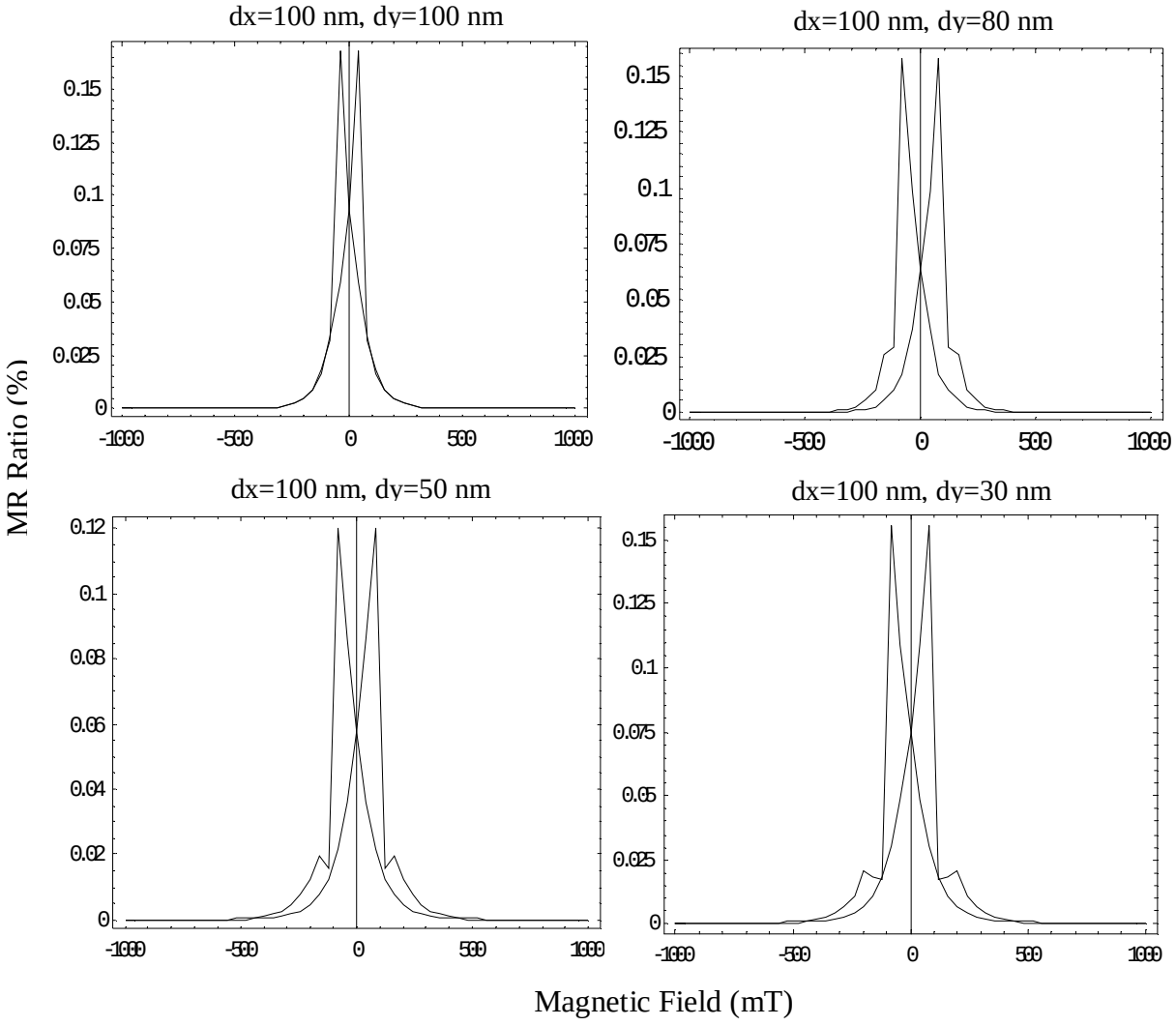

Figure 3.6 Calculated field-dependent AMR curve for the Permalloy antidot array for different vertical interdot spacing with hole size of 100 nm ×100 nm×20 nm. The magnetic fields are applied along the *x* direction.

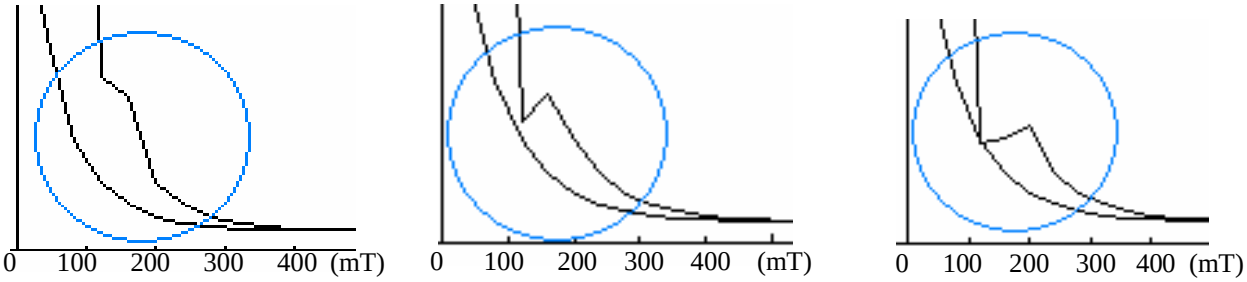

(a) dx=100 nm, dy=80 nm (b) dx=100 nm, dy=50 nm (c) dx=100 nm, dy=30 nm

Figure 3.7 The detailed picture for the small peak of AMR curve for the Permalloy antidot array for different vertical interdot spacing with the hole size 100 nm×100 nm×20 nm and magnetic field 150 mT along the *x* direction.

Figure 3.6 shows the simulated AMR results with the application of the magnetic field along *x* direction for different vertical interdot, while the size of the holes is kept constant at 100 nm×100 nm×20 nm. The position of the big peak in AMR plot can be understood in terms of the strength of the coercivity and we can observe an increasing in the coercivity of antidot arrays compared with the continuous thin films of the same thickness, which is due to the local modification of the spin rotation with the presence of the holes within the thin films. Furthermore, we can also see that the coercivity field of a structure with larger vertical spacing shows a relatively smaller coercivity field of about 40 mT while the coercivity field for structures with smaller vertical spacing is of around 100 mT. This increasing in the coercivity field with reduced vertical spacing can be attributed to the pinning of the magnetization in the vicinity of the holes, which will require higher energy to switch its direction, since the oppositely-charged magnetic poles formed during switching at the antidot-film interface are closer to one another. These simulation results are in agreement with experimental observation. For example, the study

of Permalloy film with square-shaped and circle-shaped dot arrays has also found that the coercive force increases as the separation between antidots is reduced [16].

Besides the above observation, there is also a change in the shape of the AMR curves when the vertical interdot spacing is reduced to below 100 nm, i.e. a small peak emerges at around the magnetic field of 150 mT along *x* direction (as shown in Fig 3.7). In order to investigate its origins, a refined magnetization configuration by taking more intermediate points is plotted in Fig 3.8 to show the detailed magnetization reversal process at fields of 0 mT to -160 mT along *x* direction.

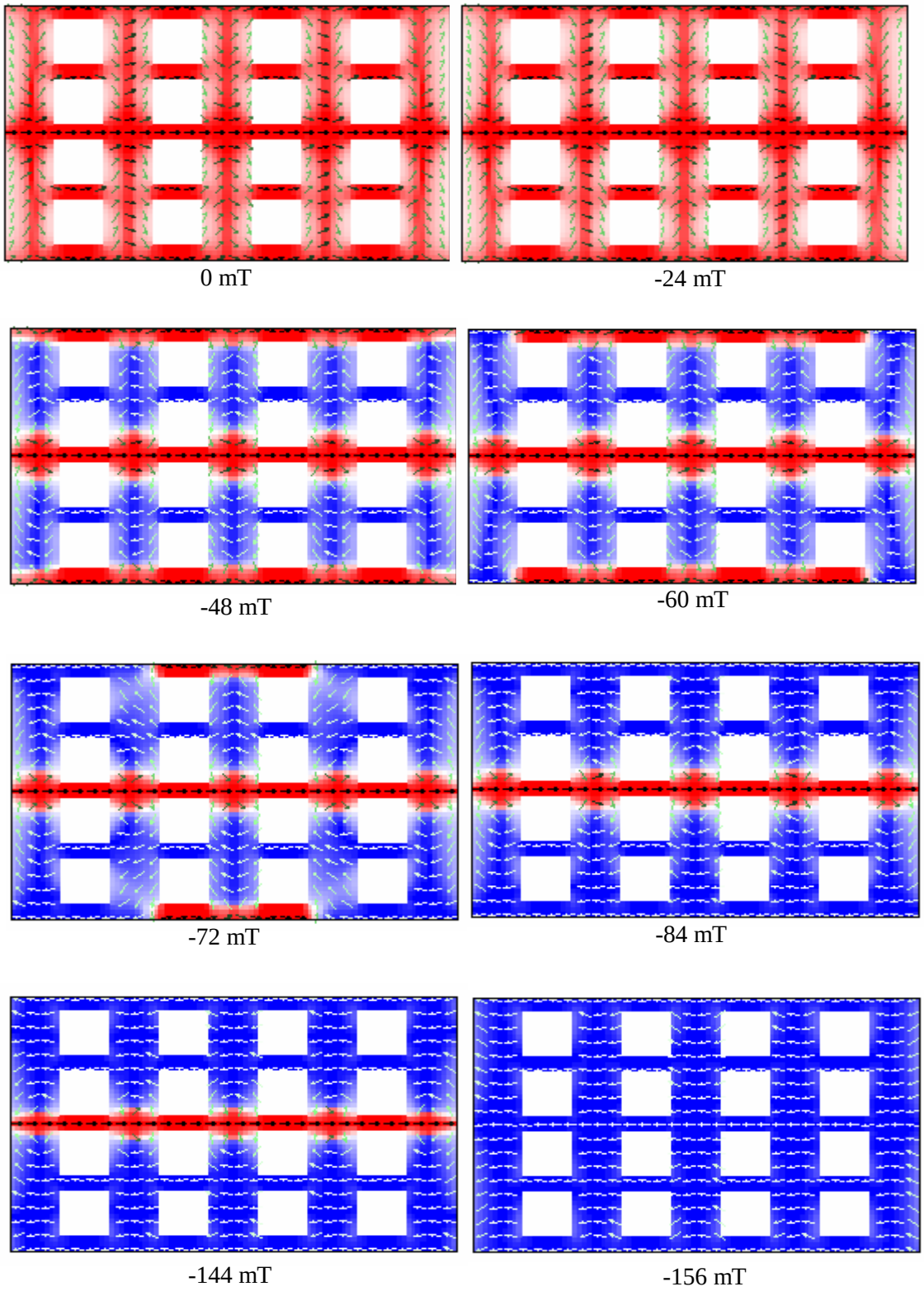

Figure 3.8 The magnetization configurations of the Permalloy antidot array with dx=100 nm, dy=30 nm and antidot size = 100 nm × 100 nm × 20 nm at different magnetic applied fields from 0mT to -156 mT along the *x* direction, obtained from OOMMF micromagnetic simulations.

From Fig 3.8, we can see that the majority of the spins switch their directions when the magnetization field increases from 0 to 48 mT in the -x direction, except spins at the upper and lower boundaries and those in the middle vertical interdot regions. Here, the vertical interdot regions refer to the regions above one antidot and below another in the y direction. The magnetization switching at 48 mT corresponds to the main peak of AMR plot, which is observed for all structures with different antidot spacing. As the strength of the positive magnetic field is increased further, the spins at the horizontal interdot regions and those at the up and bottom boundaries started to rotate their directions gradually. Their reversal behavior may be explained in terms of the combined effect of shape-induced anisotropy and edge effect at the boundaries. When the magnetic field reaches around 150 mT, it induces the magnetization reversal of the vertical interdot region in the middle of the array, and this corresponds to the small MR peak. The middle antidot region switches at a higher field compared to the other antidot regions, because it is stabilized by magnetic vortexes of opposite sense, above and below the middle line. Unlike the gradual alignment of the spins at the top and bottom boundary regions to the applied field, the middle antidot region undergoes a sharp magnetization switching, resulting in a small MR peak.

The above calculation and analysis is done with the consideration of the inhomogeneity of the current density distribution due to the presence of the antidot array within the Permalloy film. In order to have a better understanding of how it affects the magnetoresistance response, we simplified the model with a uniformly distributed current density along x-axis. Fig 3.9 shows the AMR curve obtained from our model, with the incorporation of inhomogeneous current density distribution and from the simplified

model with uniform current density distribution for structures with dx=100 nm, dy= 80nm, and dot size =100nm × 100 nm × 20 nm. The magnetic fields are applied along the *x* direction for both models. Comparing Figs. 3.6 and 3.9, we find that there is not much difference between the overall shapes and the peak positions of these two plots because of the same contribution of the magnetization switching configurations, obtained from OOMMF micromagnetic simulations. However, the saturation magnetic field of the simplified model is significantly higher than those obtained from our model because the magnetization direction aligns along the x-axis direction at a higher field than it aligns along the accurate current density direction.

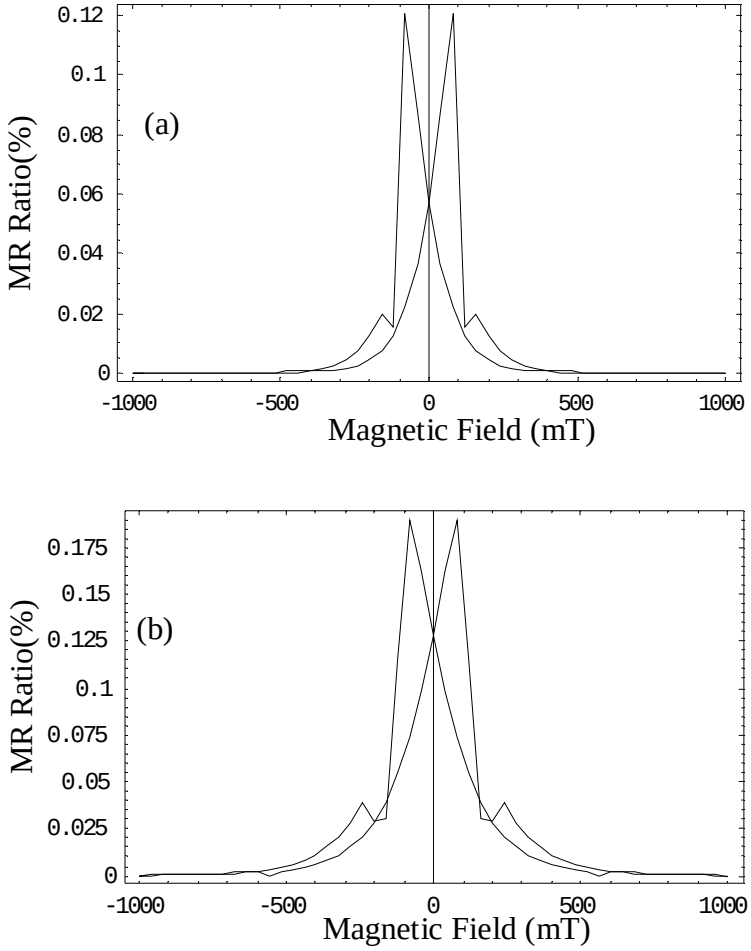

Figure 3.9 (a) Calculated field-dependent AMR curve obtained from the model with the consideration of the inhomogeneity of the current density distribution and b) with the uniform current direction along x-axis for Permalloy antidot array with dx=100 nm, dy=50 nm and hole size 100 nm ×100 nm×20 nm. The magnetic fields are applied along the *x* direction.

Next, we investigate the influence of the film thickness on the magnetization reversal properties of antidot arrays, by repeating the above analysis for the same antidot structures but with a smaller film thickness (10 nm). We found that the magnetization switching process can also be altered not only by dot size and dot spacing but also by the film thickness. Comparing Fig 3.8 and Fig 3.10, we can see that the remanent magnetization configurations of these structures are quite similar to each other, with the magnetization in most regions strongly aligned along the original field direction, while the

spins at the edges of the horizontal interdot regions pointed in the vertical direction due to the high vertical shape anisotrophy in that direction. When the magnitude of the negative magnetic field increases further, we find that the magnetization switching behaviour differs for antidot structures of different film thickness. For structures with larger thickness (20 nm), the small peak/shoulder due to the reversal of the middle antidot region occurs for interdot spacing $dy \leq 80nm$, while for structures with smaller thickness, the small peak/shoulder is only observed for smaller interdot spacing i.e. $dy \leq 50nm$ (see Fig. 3.6 and Fig 3.11). This may be explained by the fact that magnetic vortices (which stabilize the middle antidot region) can occur more easily in films of larger thickness.

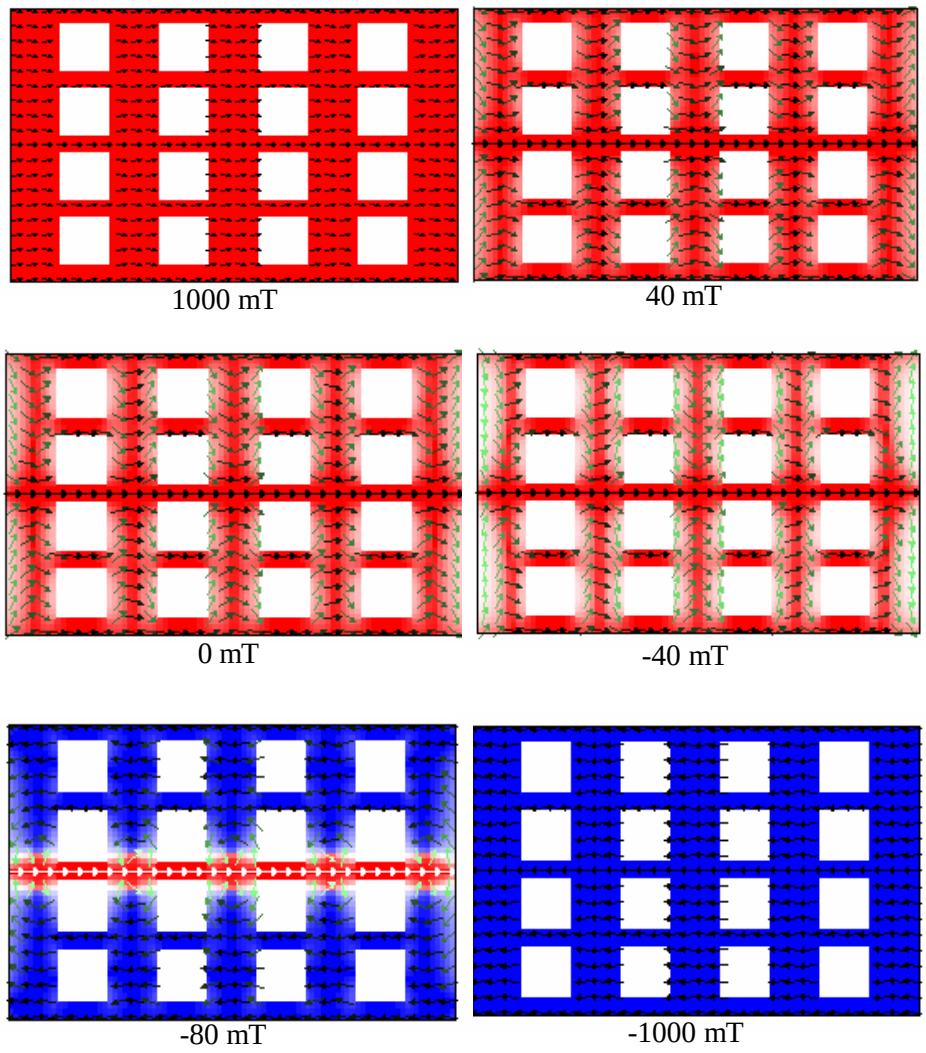

Figure 3.10 The magnetization configurations of the Permalloy antidot array with dx=100 nm, dy=30 nm and antidot size = 100 nm×100 nm×10 nm at different applied magnetic fields along the *x* direction, obtained from OOMMF micromagnetic simulations.

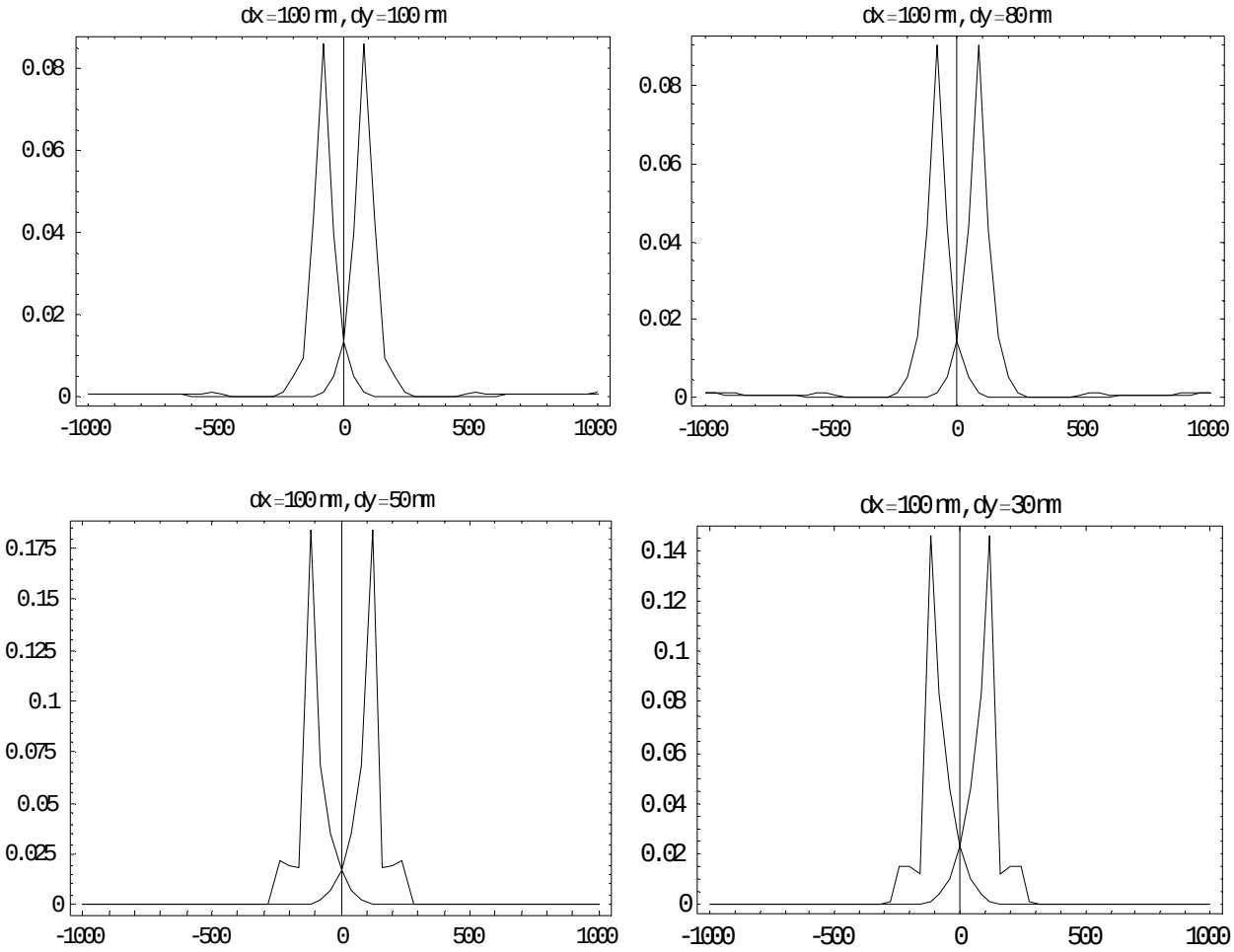

Figure 3.11 Calculated field-dependent AMR curve for the Permalloy antidot array for different vertical interdot spacing with the hole size 100 nm ×100 nm×10 nm and the applied magnetic field along the *x* direction.

3.2.5 Conclusions

In summary, a transport model has been presented to study the AMR property of a Permalloy film with square-shaped antidot arrays. The model considers the inhomogeneity in the current and magnetization distribution, and the galvanometric effects on the current due to the presence of a magnetic field. We show that magnetotransport behavior of a Permalloy film with an antidot array can be altered by changing the geometry, such as the interdot spacing or film thickness. Further studies on the correlation between geometry

and magnetic properties may lead to optimal magnetoresistive behavior for spin-based device applications.

3.3 Modeling of Magnetic Recording of Antidot Array

3.3.1 Introduction

Ferromagnetic antidot structures have been suggested as a prospective candidate for ultra high-density storage devices, because as we have seen in the previous section, the presence of antidots pattern creates regions with a remanent hard-axis, which can be used to store information bits [12,17,18]. The antidot array presents several conceptual advantages over the dot structure, (magnetic dot in a nonmagnetic media), like the absence of superparamagnetic and the preservation of magnetic continuity of the film. There is however, one disadvantage of this antidot array structure – because it is based on a continuous film, the transition from one bit to another is not well-defined. In this section, following analysis of the magnetotransport properties of the antidot structure in the previous section, we will focus on the magnetic recording quality of the antidot array. We will quantify the recording quality by considering the signal to noise ratio and contrast ratio.

The ideal situation for storage is sketched in Fig 3.12(a) [12], where the magnetization in the regions between the neighboring two bits aligns with the easy axis direction (gray region)

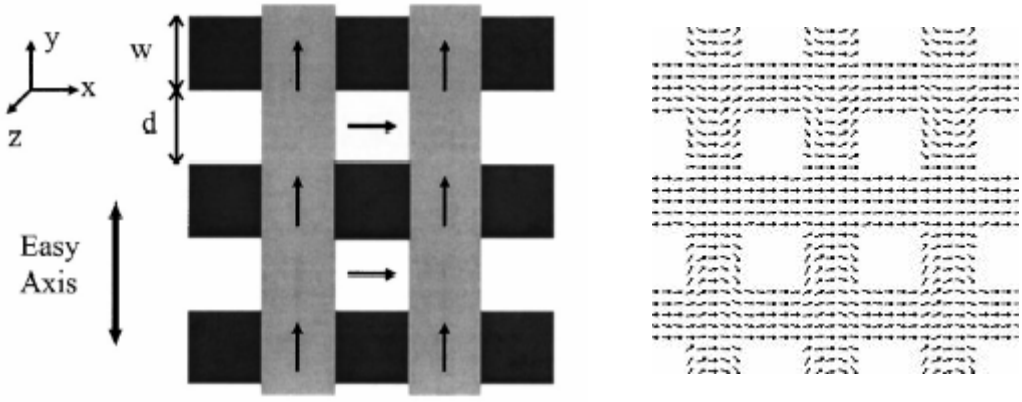

(a) (b)

Figure 3.12 (a) Diagram of the ideal remanent state for data storage. The nonmagnetic antidot is sketched in black and the white regions are the recorded bit and (b) the remanent state of the antidot array structure with dot size =100 nm×100 nm×20 nm.

Comparing the ideal magnetization of Fig 3.12(a) and the configuration obtained from micromagnetics in Fig 3.12(b), it is clear that in the latter, the magnetization in the regions between the neighboring two bits does not align well in the vertical direction, which leads to poorly defined limits for the storage bit zones. Thus, a suggested solution is the application of a vertical field to enhance the alignment of the inter-bit region along the vertical direction.

In the previous modeling [19,20] of the magnetization distribution of the patterned media, the magnetic field is applied through the entire film for both magnetic dot media and the antidot structure. But in practice, the head magnetic field is applied only on one bit at a time, rather than on the whole recording media.

Based on the two reasons above, in this work, micromagnetic simulation is performed to study the recording of a single bit of the Permalloy antidot memory array where i) a writing magnetic field is applied only to an area confined to the center bit and ii) a transverse field (cross-track direction) is applied to isolate the neighboring bits.

3.3.2 Analysis Procedure

The geometry under consideration is an array of square antidots of size 30 nm. The antidot distance in the horizontal and vertical directions *dx* and *dy,* is independently varied from 5 nm to 30 nm. For more accurate modeling of the head field, we consider a Kalqvist head field instead of the uniform magnetic field. The *x* and *y* components of the Karlqvist head field can be expressed as [21] Equ. (3.16) and Equ. (3.17):

$$H_x(x,y) = -\frac{\partial f}{\partial x} = \frac{H_g}{p}[\tan^{-1}(\frac{x+g/2}{y}) - \tan^{-1}(\frac{x-g/2}{y}) = \frac{H_g}{p}\tan^{-1}[\frac{gy}{x^2+y^2-(g/2)^2}] \quad (3.16)$$

$$H_y(x,y) = -\frac{\partial f}{\partial y} = -\frac{H_g}{2p}\ln\frac{(x+g/2)^2+y^2}{(x-g/2)^2+y^2}, \quad (3.17)$$

where *x* is the displacement among data track, *y* is the spacing between the magnetic media and head air-bearing surface, *g* is the gap distance and H_g is the magnetic field in the head gap.

Both the magnitude and the shape of the head field are important in the magnetic write process. We adopt the longitudinal magnetic recording scheme in which the recording

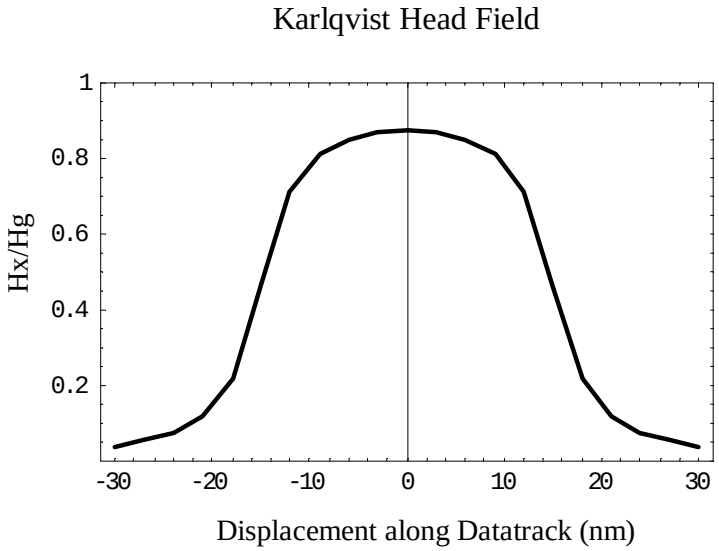

Figure 3.13.The in-plane component of the Karlqvist head field while y=0.1g, where g is assumed to be 30 nm.

media is magnetized along the data track direction. Thus we consider the effect of x component of the Karlqvist field on the antidot array. Micromagnetic simulation of the film is performed using the OOMMF software. The sample is meshed into a regular 3D grid of cubic cell of uniform magnetization. The cell size used is 5 nm which is smaller than the exchange length of Permalloy $\sqrt{2A/m_0M_s^2}$ = 5.3 nm (with the saturation magnetization M_s= $860\times10^3 Am^{-1}$, and exchange constant A=13×10^{-12} Jm^{-1}). The remanent configuration is obtained by applied the Karlqvist field only on the center bit of the antidot array, starting from sufficiently large field $2.5M_s$ in the +x direction to the $2.5M_s$ in the -x direction and vice versa, where M_s is the saturation magnetization of the Permalloy. At each field *Hx*, the total energy is minimized iteratively using the Landau-Lifshitz- Gilbert equation until the torque $\frac{\|M\times H_{eff}\|}{\|M\|}$ is within the tolerance value of 10^{-5}. The signal

quality of the data bit is quantified at remanence by the reciprocal of noise N^{-1} and contrast ratio C_r. The noise component is defined as the difference

$$N = \sum_{i \in cells} N_i = \sum_{i \in cells} \left| m_i - m_i^{ideal} \right| = \sum_{i \in cells} \sqrt{2(1 - m_i \cdot m_i^{ideal})} \tag{3.18}$$

$$N^{-1} = 1/N \tag{3.19}$$

The contrast ratio is defined as

$$C_r = \frac{\langle m_x^{center} \rangle}{\langle m_x^{inerdot} \rangle} \tag{3.20}$$

where $\langle m_x^{centerl} \rangle$ is the average value of the x component of the magnetization of the cells in the center bit region, and N^{-1} is the average value of the x component of the magnetization of the cells at the interdot region.

We need the second parameter, the contrast ratio C_r, to describe the isolation of the bit region. In some specific cases, the reciprocal of noise may be good, but the neighboring dots are not well isolated. Figure 3.15(b) shown that the magnetization direction is aligned to the horizontal in the "bit" part, which leads to a good noise reciprocal, while the horizontal regions between the "bit" are aligned in the diagonals direction not in the vertical direction, which is undesired in the storage application.

3.3.3 Results and Discussion

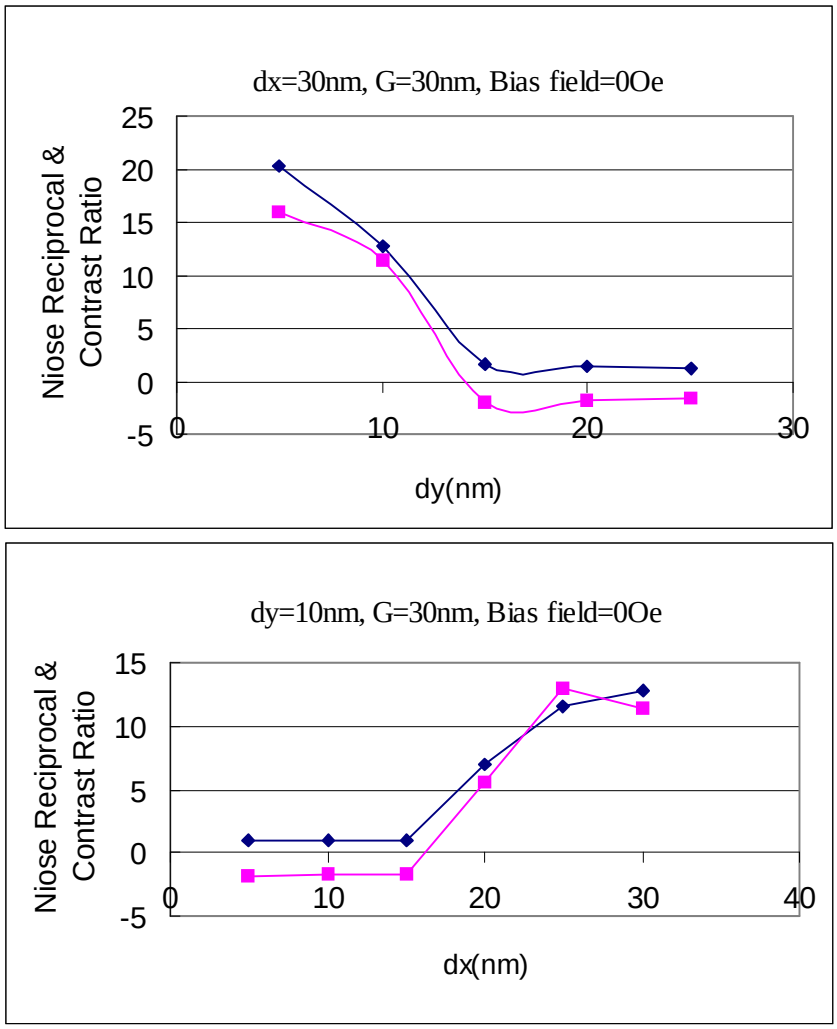

Figure 3.14 Decrease of the N^{-1} (square) and contrast ratio C_r (diamond) for different vertical antidot separation *dy* the horizontal antidot separation *dx*=30 nm (upper), and different *dx* for *dy*=10 nm (bottom), the antidot size are 30 nm×30 nm for both case.

Figure 3.14 shows the significant increase in the reciprocal of noise N^{-1} and contrast ratio C_r with increasing bit aspect ratio. For a high bit aspect ratio, e.g. 6:1, a well-defined reversal of the recorded bit at remanent state is achieved as shown by the center bit in Fig 3.15(a). For bits with low aspect ratio (i.e. more square-shaped), the shape anisotropy is too weak to maintain the written data at remanence, and the center bit reverts

back to its original magnetization direction when the head field is removed as shown in Fig 3.15(b) .

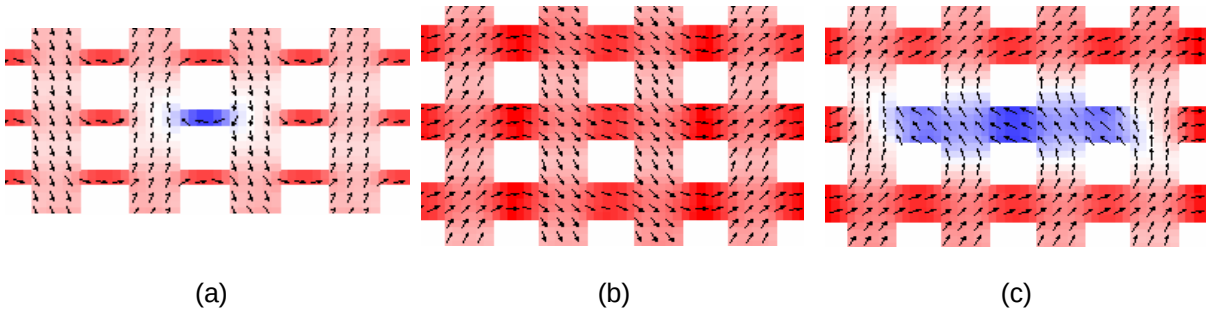

Figure 3.15 The remanent states for (a) *dx*=30 nm, *dy*=5 nm with the bias field=0Oe; (b) *dx*=30 nm, *dy*=25 nm with the bias field=0 Oe and (c) *dx*=30 nm, *dy*=25 nm with the bias field=10 Oe and antidot size of 30 nm×30 nm for all the cases.

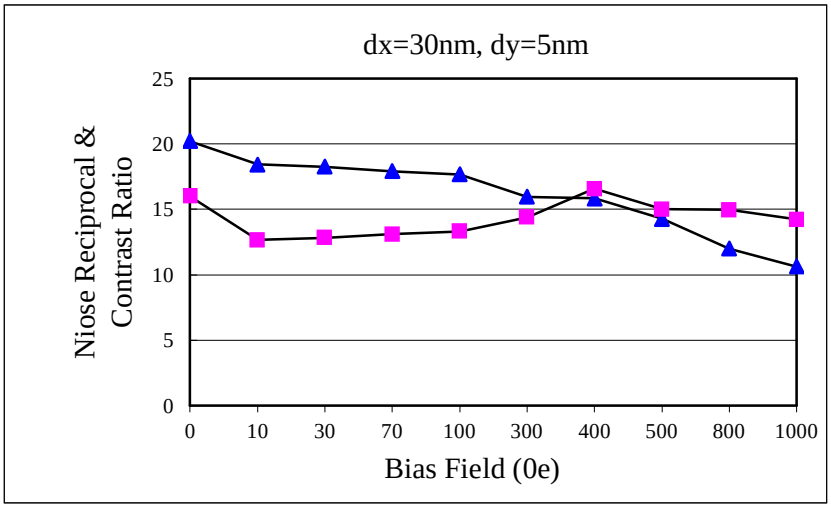

Figure 3.16 The variation of N^{-1} (blue triangle) and contrast ratio C_r (pink square) as a function of the crosstrack bias field H_y, keeping the aspect ratio constant at 6:1.

A bias field H_y along the crosstrack direction is applied throughout the whole film to separate the neighboring bits by aligning the inter-bit regions, which is expected to improve the contrast ratio. For antidots with a high aspect ratio, initially at low field less then 150 Oe, the C_r decreases. With a further increase of the bias field, C_r begins by

increase to 400 Oe, before dropping off significantly as shown in Fig 3.16. The initial decrease in C_r is due to the fact that with a relatively small H_y, the increase of the crosstrack alignment of the inter-bit region is not large enough to offset the decrease in the downtrack alignment of the bit region. With increasing the *Hy*, the influence from this crosstrack alignment becomes more prominent, which results in the increasing of C_r. And at field values above 400 Oe, the bias field H_y is strong enough to overcome the shape field, and bit magnetization is rotated along the direction of the bias field.

However, for antidots with aspect ratio of less than 2, the application of the bias field H_y fails to produce any improvement in C_r but instead causes an undesirable switching of the neighboring bits along the downtrack direction as shown in Fig 3.15(c). This observation may be explained in terms of the combined effects of magnetostatic interaction between neighboring bits and the crosstrack bias field in overcoming the shape anisotropy. However, only the two bits nearest to the central bit along the downtrack direction reverse, since there is the added effect of magnetostatic interaction arising from the magnetization of the central bit pointing in the opposite direction.

Interestingly, the neighboring bits along the crosstrack direction do not show the undesired switching even at bias field of as high as $5M_s$. The absence of switching is due to the weaker interactions between bits in the crosstrack direction, as in this case, the interaction occurs across empty antidots instead of across a continuous magnetic media.

3.3.4 Conclusion

In this section, micromagnetic simulation is performed to study the recording quality of a single bit of the Py antidot array under application of the in-plane component of the Karlqvist head field. The results show that the reciprocal of noise N^{-1} and contrast ratio C_r increase significantly with the increase in bit aspect ratio. A bias field along the crosstrack direction can further improve C_r for antidots with high aspect ratio, but causes undesirable switching of neighboring bits in the case of antidots with low aspect ratio. For an optimal noise performance in magnetic recording, the antidots should have a high aspect ratio of up to 6:1, aligned along the applied field direction, while the cross-track field should not exceed 400 Oe.

References

[1] F. W. Gorter, J. A. L. Potgiesser, and D. L. A. Tjaden, IEEE Trans. Magn. 10, pp. 899. 1974.

[2] D. A. Thompson, L. T. Romankiw, and A. F. Mayadas, IEEE Trans. Magn., 11, pp. 1039. 1975.

[3] T. R. McGuire and R. I. Potter, IEEE Trans. Magn. 11, pp. 1018. 1975.

[4] R. I. Potter, Phys. Rev. B, 10, pp. 4626-4636. 1974.

[5] A. O. Adeyeye, J. A. C. Bland, and C. Daboo, Appl. Phys. Lett. 70, pp. 3164-3166. 1997.

[6] C. C Wang, A. O. Adeyeye, N, Singh, Y. S. Huang and Y. H. Wu, Phys. Rev. B, 72, pp.174426. 2005.

[7] J-E. Wegrowe, D. Kelly, A. Franck, S. E. Gilbert and J.-Ph. Ansermet, Phys. Rev. Lett. 82, pp. 3681-3684. 1999.

[8] C. C. Yao, D. G. Hasko, Y. B. Xu, W. Y. Lee, and J. A. C. Bland, J. Appl. Phys. 85, pp. 1689-1692. 1999.

[9] J. Aumentado and V. Chandrasekhar, Appl. Phys. Lett. 74, pp. 1898-1900. 1999.

[10] M. J. Donahue and D. G. Porter <URL:http//math.nist.gov/oommf/>.

[11] A. Aharoni, Introduction to the Theory of Ferromagnetism, 2nd Edition. pp. 178, Oxford University Press, Oxford, 2000.

[12] L. Torres, L. Lopez-Diaz and O. Alejos, J. Appl. Phys. 87, pp. 5645-5647. 2000.

[13] ANSYS Release No. 5.7 (2000) by Swanson Analysis Systems, Inc. Houston, PA.

[14] R. C. O'Handley, Modern Magnetic Materials, Principles and Applications, Wiley, New York, pp. 576-579. 2000.

[15] K. Kakuno, J. Appl. Phys. 81, pp. 8105-8108. 1997.

[16] I. Ruiz-Feal, L. Lopez-Diaz, A. Hirohata, J. Rothman, C. M. Guertler, J. A. C. Bland, L. M. Garcia, J. M. Torres, J. Bartolome, F. Bartolome et al.,242-245, pp. 597-600. 2002.

[17] R. P. Cowburn et al., Apply.Phys.Lett.70, pp. 2309-2311. 1997.

[18] L.Torres et al., J. Appl. Phys. 85, pp. 6208-6210. 1999.

[19] L. Torres, L. Lopez-Diaz, and J. Iniguez, Apply. Phys. Lett. 73, pp.3766-3768. 1998.

[20] N. Dao, S. L. Whittenburg, R. P Cowburn, J. Appl. Phys. 90, pp.5235-5237. 2001.

[21] S. X. Wang and A. M. Taratorin, Magnetic Information Storage Technology, San Diego: Academic Press. 1999.

Chapter 4 Current Induced Magnetization Switching in Pseudo Spin Valve Structures

4.1 Introduction

In Chapter 3, we have dealt with the transport and magnetic properties of ferromagnetic film with antidot arrays, and investigated its possible application in ultra-high density information storage media. In this chapter, we will focus on spin-valve multilayer structure, and discuss its application as a potential spintronics device, i.e. non-volatile magnet random access memory (MRAM), which was first proposed by IBM in 1980's.

MRAM is a method of storing data bits using magnetic charges instead of electrical charges used in conventional RAM. The most significant advantage of the MRAM is that it can hold stored information for long periods of times and is thus non-volatile. Theoretical access speeds of MRAM could be similar to dynamic random access memories (DRAM), and MRAM storage density is potentially much higher than DRAM, which makes MRAM a more durable and attractive alternative than any other type of memory, thought researches on it are still at an early stage. Basically, there are two kinds of MRAM based on GMR and TMR effect, respectively. The key magnetic element in an MRAM based on the GMR effect is the pseudo-spin valve (PSV) multilayer structure, which consists of three typical layers, i.e. two FM layers sandwiched by a nonmagnetic spacer layer. In the conventional writing method, an external magnetic field generated by a current is used to switch the MRAM device as shown in Fig 4.1. It is known that

MRAM devices using GMR memory cells are organized as a series connection of many cells through all of which the current flows. When one memory cell in the series path is being sensed, the current flows through many other cells, which results on a high sensing power is owing to the power dissipated in the other cells in the sense path. Thus this method of switching has several disadvantages, in terms of integration capability and high power consumption, which limits its further application.

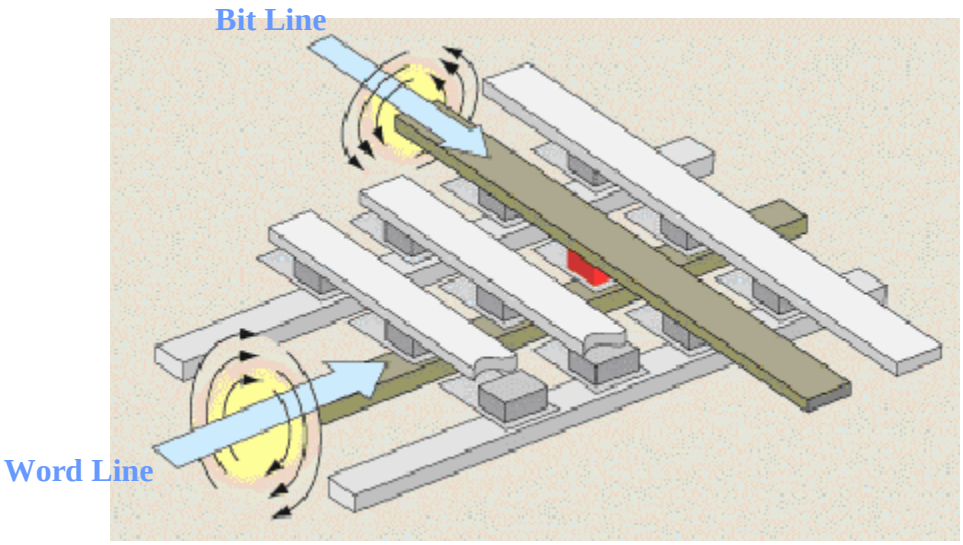

Figure 4.1 Schematic diagrams of typical MRAM cell arrays. Read and write operations are performed through bit line and word line. [Refer to: http://www.research.ibm.com/journal/rd/]

Recently, the current induced magnetization switching (CIMS) phenomenon has attracted much attention due to its potential advantage of lower power consumption and smaller risk of cross-writing, compared with the traditional magnetic field switching. CIMS phenomenon was first described theoretically by Berger [1] and Slonczewski [2] in 1996. Many experimental results have confirmed their theoretical models, and current-induced reversals have been observed in a variety of structures, such as multi-layer pillars

[3] and nanowires [4]. The detailed literature review about the existing studies of CIMS as well as the effect of the spin transfer torque, also namely as spin torque in the PSV structure can be referred to section 2.6 of Chapter 2, including in-depth discuss of the main theoretical models proposed by Zhang-Levy [5], Stiles-Zangwill [6] and main experimental works by Katine [3] and Buhrmann [7]. Previous studies [8-10] have suggested several origins for the current-induced switching: i) hydromagnetic drag force [8], which arises from the Hall effect, and is proportional to the sample thickness, ii) spin-transfer torque [9], which is caused by the exchange interactions between the spin polarized current and local magnetic moments, and iii) the classical Oersted field [10], induced by the current itself and is transverse to the current flow direction. The Oersted field contribution becomes less significant when the sample thickness is very small (a few tens of nanometers). Thus, most research work concentrate on the studies of effect of the s-d exchange interaction between the spin-polarized electrons carrying the current and the local magnetic moments. The exchange coupling between conduction electrons and local magnetic excitations is enhanced when the time interval between inelastic scattering events for the conduction electrons is longer than the inverse of the magnon-electron coupling energy. At this point, energy and angular momentum are efficiently transferred from the magnetization to the electrons at the Fermi surface. It is this exchange interaction, which produces the spin transfer between the current and local magnetic.

In this chapter, we will first introduce our own theoretical model of CIMS in magnetic multilayer structure. Section 4.2 describes a micromagnetic simulation of the magnetic switching mechanism in a ring-shaped pseudo spin valve structure, where we

considers the effects of both the Oersted and exchange fields due to spin torque.

4.2 Micromagnetic Study of Switching in Ring-shaped Spin Valve Structures

4.2.1 Introduction

Pseudo-spin valves (PSV) are a key element in high-density magnetoresistance random access memory (MRAM) [11]. For an ideal MRAM operation, we require a clear switching process between simple well-defined magnetization states. To achieve this, different geometries and sizes of the PSV magnetic multilayer, e.g. rectangles [12], truncated cones [12], needles [13] and ellipsoids [14], have been tried. However, there is a drawback to these geometries, because they result in complicated domain structures and switching processes, due to edge roughness and shape fluctuations. An alternative geometry is a circular PSV element, which forms flux-closure vortex states at remanence. These states minimize the role of the edge effect. It was found, however, that the vortex state is only stable for disks of diameters larger than approximately 100nm, depending on the materials and the thickness [14]. Moreover, the mechanism of vortex formation is complex and difficult to control [14].

Recently, it was found that the vortex structure is stabilized in ring-shaped magnetic elements, since the highly energetic vortex core is absent. The application of a vertical ring stack in MRAM devices was proposed by J. Zhu ***et al.*** [15] and subsequently studied by other researchers [16-19]. In such ring structures, the magnetic switching is

achieved by generating an Oersted field pulse using a write current. Another approach to switch the magnetization is by the application of a vertical spin-polarized current. The major advantages of current-induced, as opposed to field-induced magnetic switching, are lower power consumption and a more robust control of the switching. In the following sections, we present a micromagnetic simulation of magnetization reversal in a ring-shaped PSV consisting of a storage layer made of Permalloy (Py), a pinned layer of Co, and a Cu spacer layer. The transition between the two vortex stable states of the storage and pinned layer can be achieved by applying a vertical current pulse through the ring stack, shown schematically in Fig 4.2. The Cu spacer is sufficiently thick so that the interlayer exchange coupling between the two ferromagnetic layers can be neglected [18]. Since the thickness of each layer in the stack is only 3 nm, the effect from the hydromagnetic drag force can also be neglected. That leaves the Oersted field and the spin-transfer effects as the major contributing factors to the current driven reversal of the magnetization. Thus the origin of the current-induced switching will be discussed in these two areas. The switching mechanism is investigated for different current pulse duration and amplitude, and the threshold current density is obtained.

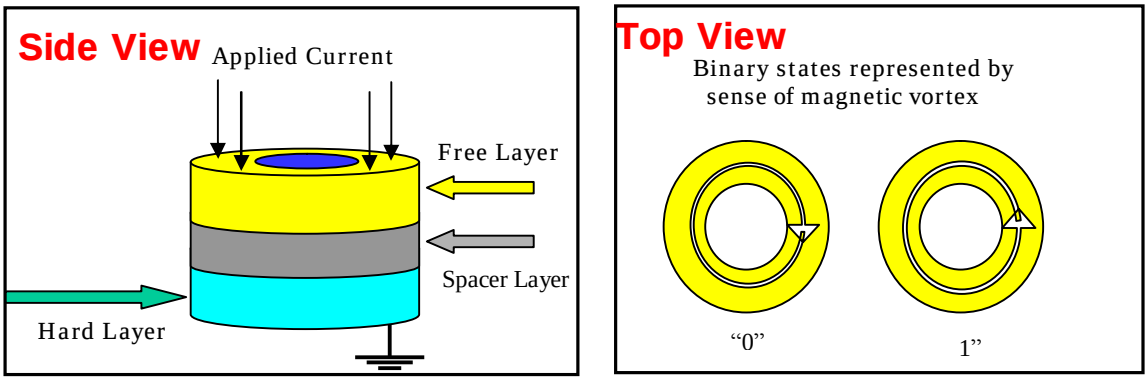

Figure 4.2 Schematic diagram of a vertical stack pseudo-spin valve with the application of a write current (left) and the binary states represented by sense of magnetic vortex of free layer (right).

4.2.2 The Oersted Field Generated by the Current

The Oersted field B generated by the current itself has the following expressions:

$$\begin{aligned} B &= 0 && R < R_{in} \\ B &= \frac{m_0 I}{2p\,(R_{out}^2 - R_{in}^2)}\left(R - \frac{R_{in}^2}{R}\right) && R_{in} < R < R_{out} \\ B &= \frac{m_0 I}{2p\,R} && R > R_{out} \end{aligned} \qquad (4.1)$$

where R is the distance to the center of the ring. The electron current I is assumed to be distributed uniformly over the cross-section of the ring. The outer radius of the ring R_{out} is set at 100 nm, while the inner radius R_{in} = 80 nm. In the region interior to the ring, no magnetic field exists, while outside the ring, the field becomes identical to that of a current-carrying wire, following Ampere's Law. Within the ring itself, the B-field is proportional to the current amplitude, and is radially symmetric and points in the tangential direction.

4.2.3 Spin Transfer Effect Analysis

Previous studies [19] have shown a spin-polarized current exerts a torque on the magnetic layers. The torque arises from the exchange coupling of the two magnetic layers, which is mediated by the spin current and local s-d exchange interaction. The resulting exchange field exerted on the Co layer h_{Co} due to the spin torque effect can be expressed as [19]

$$h_{Co} = \frac{j_s}{me}\frac{J_{Co}h}{v_{Co}^F}\frac{M_{Co}}{M_{Py}} \approx \frac{2m^*}{e}\frac{h^2}{m_{Co}}v_{Py}^F\frac{T_{Py}}{T_{Co}}j_s \qquad (4.2)$$

where $J_{Py(Co)}$ is the coupling constant between the conduction electrons and the local momentum; $M_{\mathrm{Py(Co)}}$ and $T_{Py(Co)}$ are the magnetic momentum and thickness of the Py (Co) layer; $v_{Py(Co)}^F$ and $h_{Py(Co)}$ are Fermi velocity and spin polarization ratio of the Py(Co) layer; m the permeability and j_s the spin polarized current density. The magnetization for Co is assumed to be m_{Co}=1.4x10^6 A/m, while its Fermi velocity n_{Co}^F is about 1.5x10^6 m/s. For the Py layer, the corresponding values are M_{Py}=8.0x10^5 A/m and n_{Py}^F = 0.22x10^6 m/s [20]. The field exerted on the Py layer follows the same expression as in Equ (4.2), but with the subscripts Co and Py interchanged. In Equ. (4.2), the only unknown quantity is the spin polarization ratio h, which also determines the spin current density $j_{s=}Ih/A$, where A is the cross-sectional area of the ring. Thus, we first focus on the determination of h taking into consideration both the effects of spin-diffusion and the spin-dependent reflection at the interfaces of the ring stack.

When an electron current is passed in a direction perpendicular to the plane of the magnetic layers (Fig 4. 2), it becomes spin polarized at the Co layer. We define the up and

down spin currents as

$$I_{\uparrow s1} = \frac{m_B}{2e} I(1+h_{co})$$
$$I_{\downarrow s1} = \frac{m_B}{2e} I(1-h_{co}) \tag{4.3}$$

where e, and m_B are the electron charge and Bohr magnetron, respectively, while h_{co} is the spin polarization ratio of Co layer. When the spin polarized current reaches the Co-Cu layer interface, the electrons encounter different transmission and reflection probabilities at the interface depending on their spin directions. The transmitted spin current $I_{\uparrow(\downarrow)t1}$ across the interface can be expressed as

$$I_{\uparrow t1} = G_{\uparrow t1} V_{\uparrow} = C_{\uparrow} G_{\uparrow t1} I_{\uparrow s1}, \quad G_{\uparrow t1} = (e^2/h) b_{\uparrow Co-Cu}$$
$$I_{\downarrow t1} = G_{\downarrow t1} V_{\downarrow} = C_{\downarrow} G_{\downarrow t1} I_{\downarrow s1}, \quad G_{\downarrow t1} = (e^2/h) b_{\downarrow Co-Cu} \tag{4.4}$$

where $b_{\uparrow(\downarrow)\text{Co-Cu}}$ is defined as the spin-dependent transmission probability for spin up (down) electrons and we assume $V_{\uparrow} = V_{\downarrow}$. The transmission and reflection probability are just the flux in the transmitted and reflected Bloch states divided by the flux in the incident Bloch state, and these two probabilities sum to one. The real transmission and reflection probabilities across the interface can be calculated for states on the Fermi surface of the pair of materials and the coefficient used in the following calculations are the average over the Fermi surface of the transmission/reflection probabilities. Equ (4.4) is only valid for diffusive transport across a length scale larger than the mean free path. We assume this equation is valid in this section where all the analysis is confined to the purely diffusive regions. In view of the limitation of this purely diffusive transport model, a more accurate analysis of the spin transport within the spin valve structure, based on a combined ballistic and diffusive transport, will be proposed in the next chapter. $C_{\uparrow}(C_{\downarrow})$

are the coefficients which describe the effects of some factors of decreasing the spin current such as the spin flip scattering at the interfaces, and scattering due to impurities and defects, which are encountered by spin up and spin down respectively. In this analysis, we have ignored these entire factors wand assumed that $C_{\uparrow}(C_{\downarrow})=1$. From Equ (4.4), the modified spin polarization can be written as

$$h' = \frac{I_{\uparrow t1} - I_{\downarrow t1}}{I_{\uparrow t1} + I_{\downarrow t1}} = \frac{(1+h_{co})b_{\uparrow Co-Cu} - (1-h_{co})b_{\downarrow Co-Cu}}{(1+h_{co})b_{\uparrow Co-Cu} + (1-h_{co})b_{\downarrow Co-Cu}} \tag{4.5}$$

When the spin current enters the nonmagnetic Cu layer, the spin polarization h' decays with a characteristic spin diffusion length l_{sf}. Thus, by the time, it traverses the thickness T_{Cu} of the Cu layer to reach the Cu-Py interface, h' is reduced to

$$h'' = h'\exp(-T_{cu} / l_{sf}) \tag{4.6}$$

Finally, at the Cu-Py interface, the spin current again encounters spin-dependent scattering, similar to that of the Co-Cu interface. Thus, the net spin polarization after passing through the ring stack is given by

$$\begin{aligned} h''' &= \frac{I_{\uparrow t2} - I_{\downarrow t2}}{I_{\uparrow t2} + I_{\downarrow t2}} = \frac{(1+h'')b_{\uparrow Cu-Py} - (1-h'')b_{\downarrow Cu-Py}}{(1+h'')b_{\uparrow Cu-Py} + (1-h'')b_{\downarrow Cu-Py}} \\ &= \frac{g_{Cu-Py} + h''}{1+g_{Cu-Py}h''} \end{aligned} \tag{4.7}$$

where we have defined the spin polarization ratio of the Cu-Py interface as

$$g_{Cu-Py} = \frac{b_{\uparrow Cu-Py} - b_{\downarrow Cu-Py}}{b_{\uparrow Cu-Py} + b_{\downarrow Cu-Py}} \tag{4.8}$$

We can obtain a numerical estimate of the spin polarization ratio within the ring element stack, based on known experimental values: h_{co} ~ 37% [19], $b_{\uparrow(\downarrow)\mathrm{Co\text{-}Cu}}$ = 0.95 (0.27) [21], $l_{sf.}$ of Cu ~ 140 nm, and $\gamma_{\mathrm{Cu\text{-}Py}}$ = 0.81 [22]. Substituting these parameters into

(7), the final spin polarization ratio is h'''=91%. This value is rather high compared to experimental data of each layer, h_{co} ~ 37% and h_{Py} ~80% [23]. Because we have neglected factors which may decrease h''' such as spin flip processes at the interfaces, crystal defects and impurities, and the effect of surface roughness of the magnetic layer.

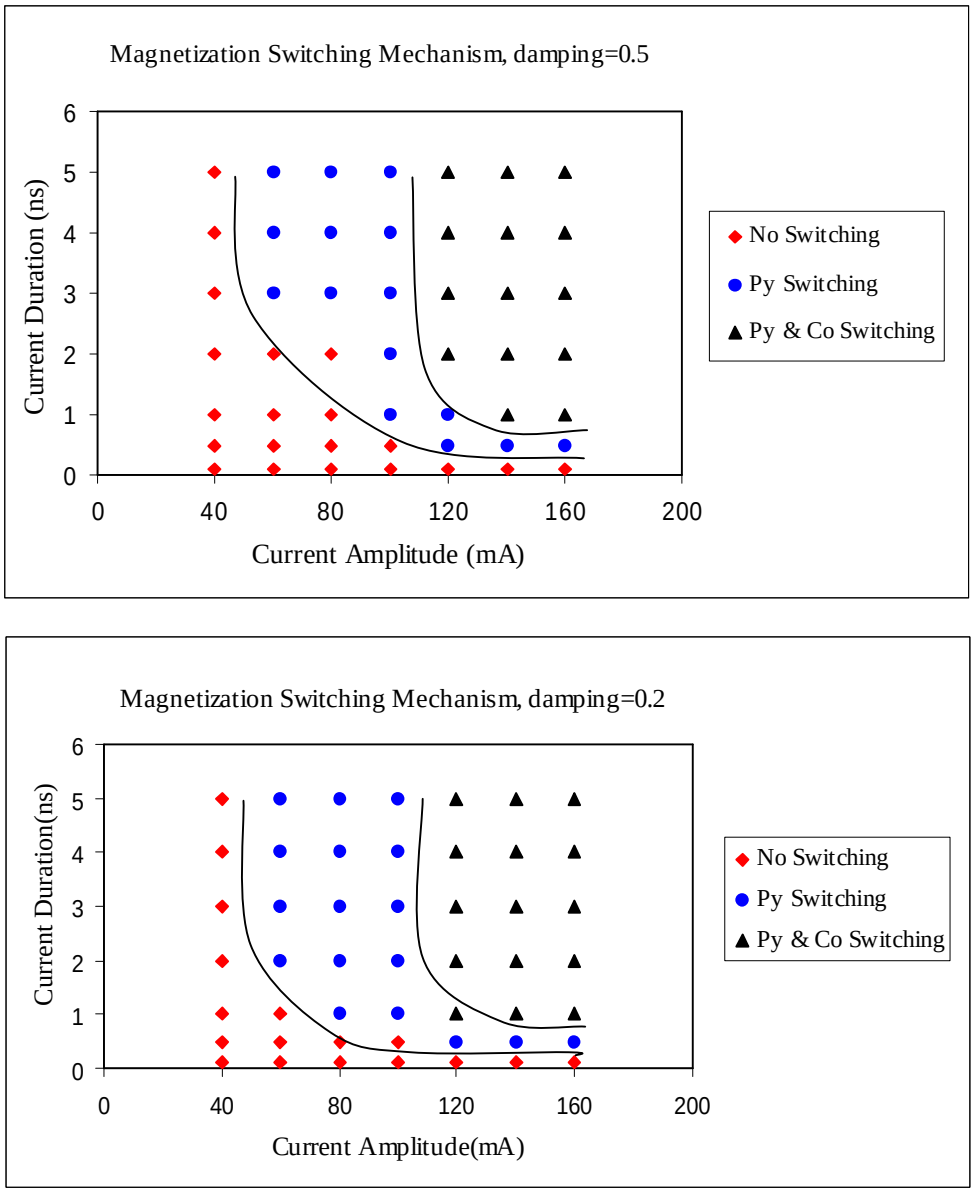

Figure 4.3 Diagram showing the switching behavior of Py (storage) and Co (pinned) layers, for different current pulse height and duration where damping constant α=0.5 (upper) and α=0.2 (bottom). Approximate boundaries between the difference switching are drawn for visual guidance only.

4.2.4 Switching Mechanism and Discussion

From the analysis of last section, we can use Equ (4.2) to evaluate the effective field $h_{Co(Py)}$ due to the spin current. The total effective field h_{eff} is then obtained by adding vectorially the Oersted field of Equ (4.1). We found the magnitude of the Oersted field (~ 10^3 Am^{-1}) to be much larger than the exchange field due to spin torque (~ 0.1 Am^{-1}). Thus, spin torque plays a relatively insignificant role in a vertical current geometry, unlike in a planar geometry, where the in-plane Oersted field is suppressed [24]. The switching process is modeled by micromagnetics, in which the ring stack is first meshed into 3D cubic cells of size 5 nm×5 nm×3 nm, and the value of h_{eff} is calculated at the center of each cell for a given current density j. The value of j is varied to obtain a switching cycle of the ring stack. The effective field h_{eff} is then incorporated into the Landau-Lifshitz-Gilbert (LLG) equation, and the resulting equilibrium magnetization is solved iteratively using the OOMMF software [25]. A default value of 0.5 of damping coefficient α is chosen so as to ensure convergence in a reasonable number of iterations [26]. In addition, it is within the medium region of damping constant. For contrast, micromagnetic simulation with other values of damping coefficients α=0.2 has also been performed, as shown in Fig 4.3. We can see that these two figures show similar trend of the switching mechanism of two FM layers. Thus the following discussion will concentrate on the results with α = 0.5. The switching mechanism is investigated for different amplitude and duration of the current pulse, and the different switching behavior is mapped out in Fig 4.3. We can observe a threshold amplitude for current-induced switching of about 50 mA, corresponding to j = 1.4 x10^8 A/cm^2, below which no switching occurs, even if the duration of the current is increased indefinitely. The threshold over-estimates the

experimental value of ~ 10^7 A/cm^2, but this difference is reasonable, considering the simplicity of our model and the difference in the device geometry. The reference refers to spin valve having long strip geometry, instead of the ring stack considered by our model [27]. Above the threshold amplitude, we obtain ideal switching behavior where only the Py layer switches. However, at higher pulse amplitude, both the soft Py and hard Co layers switch simultaneously upon application of the pulse current. The pulse duration Δt also has a significant effect on the switching mechanism. For instance, at current amplitude I = 120mA, one can obtain any of the three switching patterns by adjusting Δt. To ensure ideal switching behavior, we need to maximize the range ΔI of pulse amplitude, for which only the Py layer reverses. We found that ΔI is optimized by using pulse duration Δt of at least 3 ns. For $\Delta t \approx 4$ ns, the write pulse is sufficiently long to enable the system to settle to a steady-state during the pulse duration. Hence, no further change in switching behavior occurs for $\Delta t \geq 4$ ns.

4.2.5 Conclusions

In summary, we have modeled the current-induced switching in a vertical ring-shaped PSV element. Our micromagnetic model considers the effects of both the Oersted and exchange fields due to spin torque of the write current pulse, of which the former is dominant. The switching mechanism of the spin valve is investigated for different amplitude and duration of the current pulse, and the conditions for the desired switching behavior mapped out. It is found that ideal switching condition can be achieved with a current pulse of as short at 3 ns.

4.3 Current Induced Magnetization Switching in Pseudo-spin-valve Multilayers

4.3.1 Introduction

In the last section, we have discussed the magnetization switching mechanism and properties of the ring-shaped pseudo spin valve structure induced by spin-polarized current. The micromagnetic model considers the effects of both the Oersted from the current itself and exchange fields due to spin torque, which is related to the longitudinal spin accumulation at the spacer/free layer interface. However, recent theoretical and experimental studies [28,29] of CIMS effect demonstrate that the transverse spin accumulation, rather than the longitudinal spin accumulation, considered in the last section, plays the dominant role in the spin-transfer process. Furthermore, due to the ease of fabrication, most actual experimental works in CIMS studies focus on planar multilayer structures. To date, the study of CIMS effect in ring-shaped spin valves is confined only to theoretical and simulation models. Thus in this section, we examine the spin-transport and spin transfer switching in magnetic multilayers, which considers both transverse and longitudinal spin accumulation. Our objectives will be to clarify the origins of spin transfer torque and the switching mechanism observed in experimental results, which has not been fully explained by existing models in the literature.

First, we will briefly review the origins of spin torque and the main theoretical model before we introduce our modified spin transport model. The origin of the spin-current induced magnetization switching is the interactions between the spins of the electron carriers and the local moments within the magnetic layer. This gives rise to a spin

torque which tries to align the spin and moment direction parallel to one another. In early theoretical studies [1,2,6,30], a significant amount of spin torque is believed to occur at the nonmagnetic/ferromagnetic interfaces due to spin-dependent reflection and transmission, which results in a net transfer of transverse angular momentum to the magnetic layer. Heide *et al.* [19] neglected any spin-filtering effects at the interfaces, but considered the net spin injection which occurs when carriers pass from one FM layer to another, whose magnetization is rotated in-plane with respect to the first. This results in an effective exchange field, which exerts a torque out of the plane of the multilayer. Zhang, Levy *et al.* [5,31] extend the model of net spin injection between the two FM layers to include the spin-diffusion effects as the injected spins gradually align themselves (over the spin diffusion length) to the moment of the second FM layer. At steady-state, a region of transverse spin accumulation is sustained near the interface. In their paper, the transverse spin accumulation is resolved into two components, i.e. in-plane and out-of-plane w.r.t. the multilayers. The resultant torque thus consists of two contributions, i.e. one due to an effective field which causes an out-of-plane rotation as in Ref. 18, while the other is the Slonzewski's "spin torque" of which causes an in-plane rotation [2]. Recently A. Fert *et al.* [28] presented a model, which considered the spin torques arising from the gradient of spin accumulation within the FM and Cu layers, as well as that due to the discontinuity of spin accumulation at the interfacial zones. The discontinuity generates a large spin current, part of which is absorbed by the free FM layer, and constitutes the main source of torque in the system. Based on these existing studies, we can summarize that spin-polarized current can give rise to a spin torque based on two distinct effects, i.e., i) spin-dependent reflection and transmission at the interfaces, and ii) transverse spin accumulation, which

are either discontinuous at the interfaces, or gradual i.e. exponentially decaying within the FM and spacer layers. As can be seen, these two effects to CIMS were considered separately in previous works. It is necessary to model their combined effects so as to achieve a quantitative understanding of the different contributions to spin torques in magnetic multilayer structures. This will guide us in designing a multilayer structure, which optimizes the spin torque effect, and minimizes the critical current to CIMS.

The following sub-sections are organized as follows: First, spin-transport in a ferromagnetic/normal metal/ferromagnetic (F//N/F) trilayer will be discussed, with consideration of spin-flip process within the normal metal layer and spin-dependent reflection/transmission at the F/N interfaces. Then we will analyze the spin torque generated by the transverse spin accumulation at the interfacial zones. In the next section, the critical current density required to achieve CIMS is obtained based on the spin currents calculated in the last two sections, via the Landau-Lifschitz-Gilbert (LLG) equation describing the dynamics of the magnetization reversal process. Finally, the last section contains a discussion of the quantitative results for the specific cases of Co/Cu/Co multilayer, with and without a Ru capping layer.

4.3.2 Spin Current Transport in Magnetic Multilayers

In this section, we will analyze the spin current transport in the spin valve magnetic multilayers. Figure 4.4 shows a four-layer spin valve structure, consisting of a pinned and free ferromagnetic (Co) layers, with angle q_0 between their magnetization directions M_{Co1} and M_{Co2}, respectively, and separated by a normal metal (Cu) spacer layer. We will consider two device types, i.e. with and without Ru as the cap layer adjacent to the free Co2 layer. In this study, the Cu spacer is sufficiently thick (6 nm) so that the interlayer exchange coupling between the two ferromagnetic layers can be neglected, but thin enough such that carriers maintain some degree of spin polarization after passing through it.

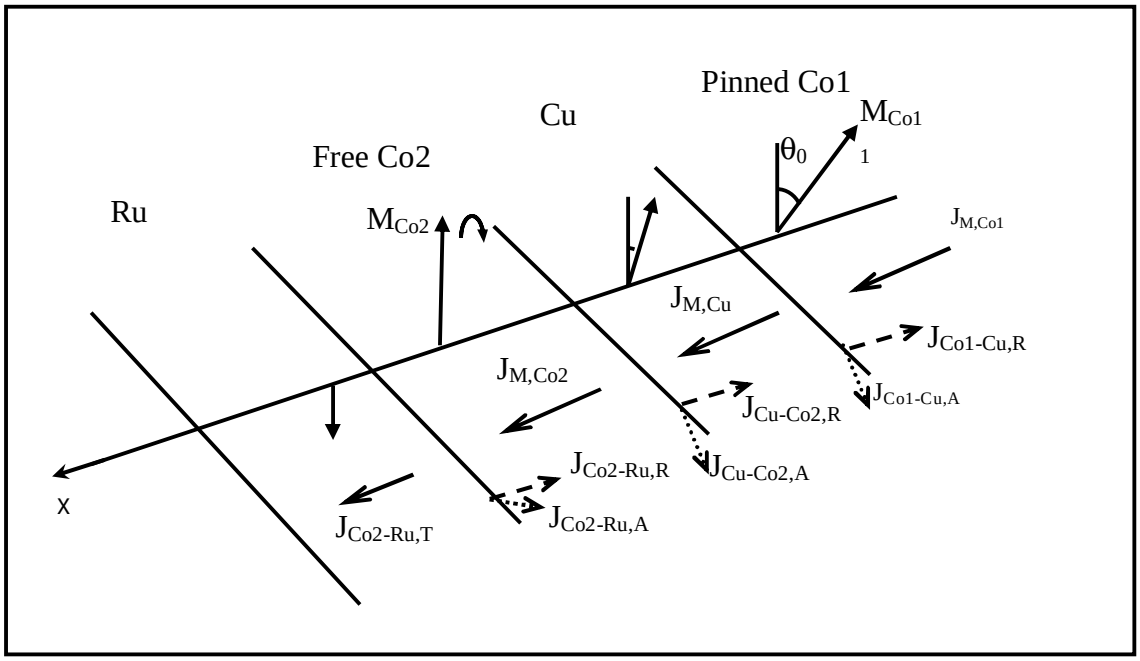

Figure 4.4 Schematic diagram of the spin current in Co/Cu/Co spin valve structure with a Ru external to the free Co2 layer. Thick black arrows indicate the local magnetization of each layer. The incoming spin current is divided into transmitted, reflected, and absorbed components at the interface, represented by solid, dashed and dotted lines, respectively.

Consider an electron current passed in a direction perpendicular to the plane of the multilayers (Fig 4.4) starting from the pinned Co1 layer. The current becomes spin polarized as it passes through the Co1 layer. Far from the Co1/Cu interface, the spin current is given by

$$J_{M,Co1\uparrow(\downarrow)} = \frac{m_B(1 \pm h_{Co})}{2e} J_q \tag{4.9}$$

where e is the electron charge, m_B the Bohr magneton, J_q the charge current and h_{Co} the spin polarization ratio of Co layer, defined as $(J_\uparrow - J_\downarrow)/(J_\uparrow + J_\downarrow)$ in bulk Co. The direction of $J_{M,Co1\uparrow(\downarrow)}$ is parallel (antiparallel) to the local magnetization direction of Co1 layer.

When the spin-polarized current $J_{M,Co1}$ reaches the Co1/Cu interfacial zone, part of the incoming spin current is absorbed in the interfacial zone. This absorbed component can be expressed as $J_{Co1-Cu,A} = te^{ie} J_{M,Co1}$, where t is the coefficient for the spin memory loss.[13] The real (imaginary) part of $J_{Co1-Cu,A}$ represents the absorbed spin current component perpendicular (parallel) to the plane of the multilayers. For most interfaces between the ferromagnetic and nonmagnetic metals, the angle e is very small (i.e. it is mostly the out-of-plane component which is absorbed). The remaining spin-current will either be reflected back into the Co1 layer or undergo differential transmission through the interface into Cu layer, depending on their spin directions. The transmitted (reflected) spin current $J_{Co1-Cu,T\uparrow(\downarrow)}$ ($J_{Co1-Cu,R\uparrow(\downarrow)}$) at the Co1/Cu interface can be expressed as

$$J_{Co1-Cu,T\uparrow(\downarrow)} = b_{\uparrow(\downarrow)Co-Cu}(1-t)J_{M,Co1\uparrow(\downarrow)} \tag{4.10a}$$

$$J_{Co1-Cu,R\uparrow(\downarrow)} = g_{\uparrow(\downarrow)Co-Cu}(1-t)J_{M,Co1\uparrow(\downarrow)} \tag{4.10b}$$

where $b_{\uparrow(\downarrow)Co-Cu}$ ($g_{\uparrow(\downarrow)Co-Cu} = 1 - b_{\uparrow(\downarrow)Co-Cu}$) are the spin-dependent transmission (reflection) probabilities respectively, at the Co1/Cu interface. The spin-dependent transmission through the interface, and the transverse component of the absorbed spin current result in a build-up of nonequilibrium spin, i.e., spin accumulation at the interface. These accumulated spins will exert a spin torque on the local magnetic moments within the pinned Co layer. However, the pinned layer is made much thicker than the free Co layer, so that its magnetization configuration is assumed to be unaffected by the spin torque during the magnetization switching of the free layer.

The transmitted spin current entering the nonmagnetic Cu layer decays with a characteristic spin diffusion length l_{Cu}. Thus, by the time it traverses the thickness T_{Cu} of the Cu layer to reach the Cu-Co2 interface, the spin current is reduced to

$$J_{M,Cu\uparrow(\downarrow)} = J_{Co1-Cu,T\uparrow(\downarrow)} \exp(-T_{Cu} / l_{Cu}) \tag{4.11}$$

At the Cu/Co2 interfacial zone, the spin current encounters a spin-dependent scattering process, similar to that at the Co1/Cu interface. The incoming electron spins will be partially absorbed at the interfacial zone, i.e. $tJ_{M,Cu}$, while the remainder will be either reflected back across the interface into Cu layer, or be transmitted across the interface zone into the free layer Co2. The imbalance of electron spin on both sides of the Co2 layer will exert a torque on the local moments of the free layer so as to align them along the magnetization $\boldsymbol{M_{Co1}}$ of the Co1 layer. The strength of this spin torque will be given in the

next section. The expression for the transmitted (reflected) spin current $J_{Cu-Co2,T(R)}$ at the Cu/Co2 interface is similar to Equ (4.10), i.e.

$$J_{Cu-Co2,T\uparrow(\downarrow)} = b_{\uparrow(\downarrow)Cu-Co}(1-t)J_{M,Cu\uparrow(\downarrow)} \tag{4.12a}$$

$$J_{Cu-Co2,R\uparrow(\downarrow)} = g_{\uparrow(\downarrow)Cu-Co}(1-t)J_{M,Cu\uparrow(\downarrow)} \tag{4.12b}$$

where $b_{\uparrow(\downarrow)Cu-Co}$ ($g_{\uparrow(\downarrow)Cu-Co} = 1 - b_{\uparrow(\downarrow)Cu-Co}$) are defined as the spin-dependent transmission (reflection) probabilities at the Cu/Co2 interface. The reflected spin current will travel in the reverse direction back into the Cu layer. Due to the long spin diffusion length of Cu compared to the spacer thickness, the reflected spin current maintains a high degree of its initial value when it arrives at the Cu/Co1 interface. Thus, the spin-filtering processes at the two Co-Cu interfaces are not entirely independent of each other and so we need a self-consistent approach to account for the effect multiple scattering of spin current at both interfaces. The specular transmission/reflection at the two interfaces are continued until the ratio between the transmitted spin current at the *m*th reflection $J^m_{Cu-Co2,T}$ is less than some preset fraction of the original spin current, i.e. $\frac{J^m_{Cu-Co2,T}}{J_{M,Co1}} \le 10^{-4}$. After *m* reflections, the total transmitted spin current at the Cu/Co2 interface is the sum of transmitted spin currents at alternate reflections. After the spin current enters the Co2 layer, it will be "re-polarized" along the magnetization direction of the Co2 layer. By the time it reaches the Co2/Ru interface, the spin current along the magnetization of Co2 layer is increased to

$$J_{M,Co2\uparrow(\downarrow)}(T_{Co2}) = J_{Cu-Co2,T\uparrow(\downarrow)} exp\left(-\frac{T_{Co2}}{l_{Co}}\right)\cos q_0 + \frac{m_B(1\pm h_{Co})}{2e} J_q\left[1 - exp\left(-\frac{T_{Co2}}{l_{Co}}\right)\right] \tag{4.13}$$

where h_{Co} is the spin polarization ratio of Co.

We now consider the effect of the spin current entering the Ru cap layer, which is added on to the typical trilayer spin-valve structure. It has been theoretically predicted that inserting Ru into Co leads to a "negative" magnetic scattering anisotropy, i.e., majority spins are scattered more strongly than minority spins [32], due to the formation of an inter-diffused CoRu alloy. This negative magnetic scattering anisotropy results in a high spin accumulation at the Co2/Ru interfaces. Due to the small thickness of the Ru layer compared with its mean free path, ballistic transport analysis of the spin current is carried out at the Co-Ru interface. The wavefunction of the transmitted current $J_{Co-Ru,T}$ at the Co2/Ru interface is an admixture of both majority and minority wavefunctions in Ru as expressed in Equ. (4.14) (assuming that the incident electron spin points in a direction of (θ_0, $\phi = \pi/4$) with respect to the local magnetization direction)

$$y = e^{-ip/4}\cos(\theta_0/2)b_{\uparrow Co-Ru}exp(ik_x^{\uparrow}x) + e^{ip/4}\sin(\theta_0/2)b_{\downarrow Co-Ru}exp(ik_x^{\downarrow}x) \qquad (4.14)$$

From the electron wavefunction, the charge current density and the spin angular momentum current density tensor can respectively be evaluated [6]

$$j(x) = -\frac{i\mathbf{h}}{2m}\Sigma[y_s^{*}\nabla y_s + h.c.] \qquad (4.15)$$

$$Q(x) = -\frac{i\mathbf{h}^2}{4m}\sum_{s,s'}\left[y_s^{*}[s_m]_{s,s'} \otimes \frac{\partial}{\partial x_n}(y_{s'}) + h.c.\right] \qquad (4.16)$$

where the summation is over both spin directions s, s' and s_m is the vector of Pauli spin matrices. The spin current is denoted by a tensor $\mathbf{J}$ such that $[\mathbf{J}]_{m,n}$ represents flux of electrons having spin orientation m, along the x_n direction. The spin current polarization unit vector p is then defined as

$$p = \frac{2}{\mathbf{h}} \frac{Q(x) \cdot j(x)}{\left| j(x) \right|^2} \tag{4.17}$$

and the transmitted spin polarized current is then given by

$$J_{Co-Ru,T\uparrow(\downarrow)} = J_{M,Co2\uparrow(\downarrow)}(x) \frac{j_{Co-Ru,T}(x)}{j(x)} \tag{4.18}$$

We can obtain a numerical estimate of the spin polarization of current within the four-layer spin valve structure, based on known experimental values of parameters: $h_{Co} \approx 38\%$ [19], $t_{Co-Cu(Cu-Co)} = 0.3$, $e = 3\times10^{-2}$, $b_{\uparrow(\downarrow)Co-Cu} = 0.73(0.54)$, $g_{\uparrow(\downarrow)Co-Cu} = 0.27(0.46)$ [21], l_{Cu} of Cu ~ 140 nm, l_{Co} of Co ~ 59 nm, $b_{\uparrow(\downarrow)Cu-Co} = 0.94(0.33)$, $g_{\uparrow(\downarrow)Cu-Co} = 0.06(0.67)$ [33], $t_{Co-Ru} = 0.35$ and $b_{\uparrow(\downarrow)Co-Ru} = 0.18(0.82)$. The thickness of the spin valve multilayers are chosen to be T_{Co1} = 10 nm, T_{Cu} = 6 nm, T_{Co2} = 3 nm and T_{Ru} = 0.45 nm. Substituting these parameters into Equs (4.9) to (4.18), the spin polarization ratio of transmission current of Cu/Co2 interface is 74.7%. After the current reaches the Ru layer, the spin-polarized current is decreased to 4.3% due to the strong scattering of majority spins at the Co2/Ru interface. In our calculations, we have neglected factors such as, crystal defects and impurities, and the effect of surface roughness of the magnetic layer.

4.3.3 Spin Transfer Torque

In the previous section, we have evaluated the spin currents at various layers of the spin-valve structure, which result in a transverse spin accumulation at the crucial Cu/Co2 interface. This is composed of (a) net spin accumulation generated from the reflected and transmitted spin current due to the spin-diffusion process, and (b) the transverse

component of absorbed spins at the interfacial zone. It was shown in previous studies that the spin torque effect acting on the free layer is proportional to the spin accumulation at its interfaces [28]. The contribution from (a), arises from the interaction between reflected spin current $J_{Cu-Co2,R}$ and transmitted spin current $J_{Cu-Co2,T}$ with the Co2 layer over a distance T (exchange length of spin-electron interactions) from the Cu/Co2 interface. During this interaction, the direction of the reflected spin current $J_{Cu-Co2,R}$ remains constant but there

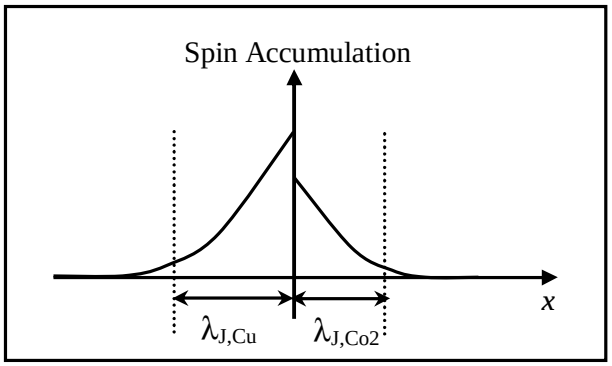

Figure 4.5 Schematic diagram of the population of the non-equilibrium spin-polarized electrons near Cu/Co interface. The spin accumulation decays exponentially with characteristic lengths $l_{J,Cu}$ within the Cu layer and $l_{J,Co}$ within the Co layer.

is a decay in the magnitude of its transverse component due to spin depolarization with a diffusion length l_{Cu}, which yields a net spin accumulation current $J^{Ac}_{Cu-Co2,R}$

$$J^{Ac}_{Cu-Co2,R} = -\int_{-T}^{0} \frac{\partial[J_{Cu-Co2,R} exp(\frac{x}{l_{Cu}})}{\partial x} dx = J_{Cu-Co2,R}[exp(-\frac{T}{l_{Cu}}) - 1] \qquad (4.19a)$$

where we have neglected $\uparrow(\downarrow)$ arrows for clarity. On the other hand, the repolarization of

the transmitted spin current $J_{Cu-Co2,T}$ within Co2 layer also results in a spin accumulation current $J^{Ac}_{Cu-Co2,T}$ given by

$$J^{Ac}_{Cu-Co2,T} = J_{Cu-Co2,T} - J_{M,Co2}(T) \tag{4.19b}$$

The contribution from (b) is due to the absorbed spin current $tJ_{M,Cu}$ at the Cu/Co2 interface. This causes a discontinuity in the spin accumulation density at the interfacial zone as shown in Fig 4.5. Away from the interface, the spin accumulation density decays exponentially with characteristic lengths $l_{J,Cu}$ within the Cu layer and $l_{J,Co}$ within the Co2 layer [5], where $l_{J,Cu(Co)}$ are significantly smaller than their respective spin diffusion lengths $l_{Cu(Co)}$. The resulting spin current due to the spin accumulation discontinuity is approximately a factor $l_{Co}/4l_{MFP,Co} >> 1$ [28] larger than the original absorbed spin current, where $l_{MFP,Co} \approx$ 6 nm is the mean free path of the Co layer. So the total absorbed transverse spin current at the Cu/Co2 interface from contributions (a) and (b) is

$$J_{Cu-Co} = t_{Cu-Co} J_{M,Cu} \sin\theta_0 \frac{l_{Co}}{4l_{MFP,Co}} + J^{Ac}_{Cu-Co,R} + J^{Ac}_{Cu-Co,T} \tag{4.20}$$

Additionally, spin flip processes within the lead layer is another source of spin accumulation at the boundary between the lead layer and the Co2 layer. But in most experimental pseudo-spin-valve (PSV) structures, the lead layer is made up of by Cu, which has a long spin diffusion length. So the resulting distributed torque is very small and can be neglected.

In an alternative device structure, a ruthenium (Ru) layer is inserted in between the Cu lead layer and Co2 layer. The Ru constitutes a "wall" of spin scatterers, which strongly

acts on the majority spins. This translates into a short spin diffusion length for Ru of 14 nm [34], resulting in a much higher distributed torque at the Co2/Ru interface. The reflected and transmitted spin accumulation currents, $J^{Ac}_{Co2-Ru,R}$ and $J^{Ac}_{Co2-Ru,T}$, are given by

$$J^{Ac}_{Co2-Ru,R} = J_{Co2-Ru,R} - J_{M,Co2}(T_{Ru}) \tag{4.21a}$$

$$J^{Ac}_{Co2-Ru,T} = \int_0^{T_{Ru}} \frac{\partial[J_{Co-Ru,T} exp(-\frac{x}{l_{Ru}}) \times sin(1-\frac{x}{l_{Ru}}) q_0]}{\partial x} dx \tag{4.21b}$$

The integral in Equ (4.21b) extends only to the thickness of the Ru layer T_{Ru} which is smaller than the exchange length of spin-electron interactions. The total absorbed transverse spin current at the Co2/Ru interface can be expressed as

$$J_{Co-Ru} = t_{Co-Ru} J_{M,Co2} sinq_0 \frac{l_{sf}}{4l_{MFP,Ru}} + J^{Ac}_{Co2-Ru,R} + J^{Ac}_{Co2-Ru,T} \tag{4.22}$$

where $l_{sf} = 1/\sqrt{(1/l_{sf})^2 + (i/l_J)^2}$, $l_{sf} = l_{Ru}/\sqrt{1-bb'}$, $l_J = \sqrt{l_{MFP,Ru} d_J / 3p}$ [12] and the mean free path $l_{MFP,Ru}$ within Ru ~ 1.4 nm [35]. The relaxation length l_{sf} for the transverse spin incorporates not just the usual spin diffusion length but also an additional contribution due to spin precession about the local magnetic moments. From the above results, the total torques exerted on the magnetic moments of the free Co2 layer can be expressed as [6]

$$\frac{\dot{\Gamma}}{\mathbf{h}} = \frac{A}{2}(J_{Cu-Co} + J_{Co-Ru}) M_{Co2} \times (M_{Co2} \times M_{Co1}) \tag{4.23}$$

where A is the cross-sectional area of the spin valve structures.

4.3.4 Results and Discussion

Since the spin-transfer torque is proportional to the charge current, Equ (4.23) can be written as

$$\vec{\Gamma} = G\, J_q A[M_{Co2} \times (M_{Co2} \times M_{Co1})] \tag{4.24}$$

Equating the torque to the rate of change of angular momentum, we have

$$\vec{\Gamma} = \frac{d\vec{L}}{dt} = \frac{m}{g}\frac{d\vec{M}}{dt} = \frac{m}{g} M_s At \frac{d\vec{m}}{dt} \tag{4.25}$$

where m is the permeability in free space and g is the gyromagnetic ratio. Based on the above relation, we introduce a quantity G' which is related to G in Equ. (4.24) as

$$G' = \frac{gm_B}{htM} G = \frac{g}{mtM} G \tag{4.26}$$

From the LLG equation, the critical current density at zero applied magnetic field can be expressed in terms of G' as [28]

$$j_C^{P\to AP} = \frac{ag}{G'^{P\to AP}}(-H_{an} - H_{ex} - 2pM) \tag{4.27a}$$

$$j_C^{AP\to P} = \frac{ag}{G'^{AP\to P}}(H_{an} - H_{ex} + 2pM) \tag{4.27b}$$

where a is the Gilbert damping coefficient measured by ferromagnetic resonance to be 0.007 for Co, g for Co is 2.21×10^5 m/(A.s), $m_0 = 4\pi\times 10^{-7}$ kg.m/c^2, H_{an} is the anisotropy field = 4.2×10^6 A/m for Co, H_{ex} is the exchange field and M_s is the saturation magnetization and measured to be 1.4×10^6 A/m for Co. Here, we assume that H_{an} dominated over any exchange field H_{ex} for large Co layer. $P\to AP(AP\to P)$ denote parallel to antiparallel magnetization switching, i.e. the angle q_0 between Co1 and Co2 layers changes from 0° to 180° and vice-versa. Since the maximum torque occurs when $q_0 = 90°$ and zero at $q_0 = 0°$, we consider the average torque value, i.e. at $q_0 = 45°$ to obtain the numerical value of G' from Equ (4.26). By substituting the calculated results of the absorbed transverse spin current [i.e. Equs (4.19) to (4.22)] into Equs (4.24), (4.26)

and (4.27), we found that without the Ru layer, i.e., without J_{Co-Ru} in Equ (4.23), the critical currents are $j_C^{P\to AP} = -1.02\times10^8\, A/cm^2$ and $j_C^{AP\to P} = 6.97\times10^7\, A/cm^2$. With the presence of the Ru layer adjacent to the Co2 layer, the additional distributed torque at the Co2/Ru interface causes a decrease in the critical current to $j_C^{P\to AP} = -5.39\times10^7\, A/cm^2$ and $j_C^{AP\to P} = 3.78\times10^7\, A/cm^2$, respectively.

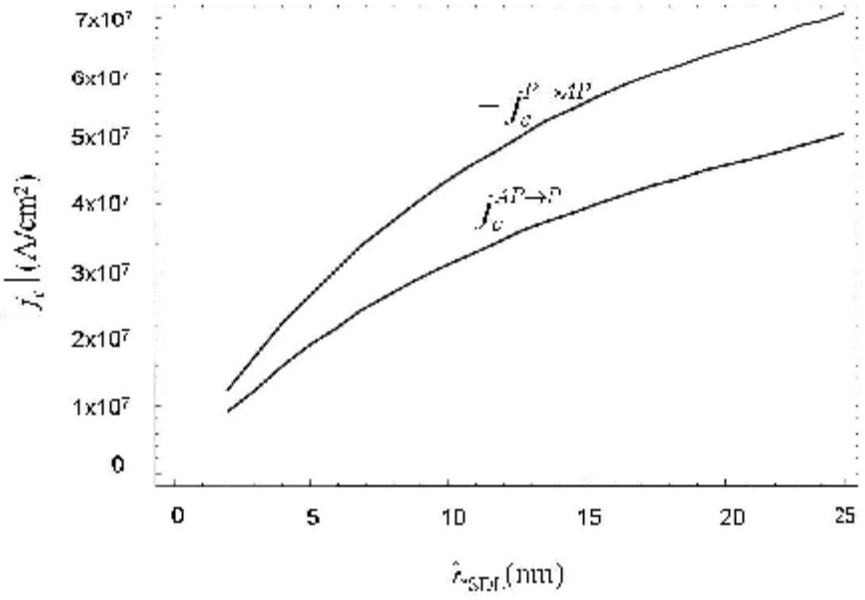

Figure 4.6 Plot of the absolute value of the critical current density $|j_c|$ as a function of the spin diffusion length of the cap layer λ_{SDL}.

Our data are generally consistent with the experimental and theoretical results of other models, for which the critical current density is of the order of 10^7 A/cm^2. The reduction of the critical current density by a factor of 1.8 times with the insertion of Ru layer is also in agreement with Dr. Ochiai's [36] experimental results obtained from Co/Cu/Co PSV structures. Their results indicated that the insertion a Ru layer, reduces the critical current density j_c by a factor of not more than 2 times. Two crucial factors in the reduction of j_c are the short diffusion length of the Ru layer l_{SDL} and the low majority

carrier transmission coefficient $b_{\uparrow,Co-Ru}$, both of which reflect the strong scattering nature of Ru. Figure 4.6 shows the strong dependence of j_c on the l_{SDL} of the cap layer, keeping other parameter values e.g. reflection/transmission coefficient the same as for a Co-Ru interface. A decrease of $j_c \approx 1\times10^7$ A/cm^2 occurs for l_{SDL} = 2 nm.

For the practical application of current-induced switching in PSV structures, it is essential to investigate ways of further reducing the critical switching current. In our model, the critical current density is determined by the absorbed transverse spin current, which is related to the spin polarization ratio of the pinned ferromagnetic layer, the spin-dependent transmission and reflection probability at the interface and the spin-flip process within the nonmagnetic layers. Thus, the most obvious method of reducing the critical current is by increasing the spin-polarization ratio of the pinned ferromagnetic. An ideal possibility is to use a half-metal, which possesses almost 100% spin polarization in the CIMS devices. Our analysis also indicates that the critical current density is strongly dependent on the interfacial spin scattering between the ferromagnetic and nonmagnetic layers. This suggests that experimental methods of modifying those interfaces should be worth exploring. These include varying the interfacial roughness or changing the local composition, which will in turn modify the spin-dependent transmission and reflection probabilities at the interfaces. Another potential method is to enhance the spin accumulation at the interfaces of the free layer, which exerts an additional torque on the magnetic moments of the free layer. In our model, this is achieved by inserting a Ru layer between the free layer and the top lead electrode, to act as a strong scatterer of majority spins. Further experimental studies on Ru layer in exchange-biased spin valve [37] have

also confirmed the role of the Ru layer in reducing the critical current density. Recently, some researchers [38] have found that the insertion of another strong spin-scatter, $Fe_{50}Mn_{50}$ could also decrease the critical current for current-induced switching in multilayer magnetic nanopillar structures, via a similar mechanism as that induced by Ru. These evidences all suggest a means of increasing spin accumulation by incorporating a strong spin-scatterer material with a short spin diffusion length and high reflection coefficient, between the magnetic trilayer and the lead electrode.

4.3.5 Conclusions

In section 4.3, we have studied the switching of a magnetic layer with the application of a spin polarized current in a PSV structure. The spin polarized current in the PSV multilayers is analyzed based on spin-differential reflection/transmission at the interfaces, interfacial transverse spin absorption and spin depolarization within the nonmagnetic spacer. The insertion of Ru layer between the free and top electrode layer is found to enhance the spin accumulation at the interface. This results in a reduction of the critical current density by a factor of about 2 times, which is in agreement with experimental results. Finally, we propose several methods for further reduction in the critical current density, which is crucial for future spintronics applications.

References

[1] L. Berger, Phys. Rev. B, 54, pp.9353-9358. 1996.

[2] J. C. Slonczewski, J. Magn. Magn. Mater., 159, pp.L1-L7. 1996.

[3] J. A. Katine, F. J. Albert, R. A. Buhrman, E. B. Myers and D. C. Ralph, Phys. Rev. Lett., 84, pp.3149-3152, 2000.

[4] J.-E.Wegrowe, et al., Appl. Phys. Lett., 80, pp.3775-3777, 2002.

[5] S. Zhang, P. M. Levy and A. Fert, Phys. Rev. Lett., 88, pp.236601. 2002.

[6] M. Stiles and A. Zangwill, J. Appl. Phys. 91, pp.6812-6817. 2002

[7] F. J. Albert, N. C. Emley, E. B. Myers, D. C. Ralph and R. A. Buhrman, Phys. Rev. Lett., 89, pp.226802. 2002.

[8] W. J. Carr, J. Appl. Phys., 45, pp. 394-396, 1974.

[9] K. Xia, P. J. Kelly, G. E. W. Bauer, A. Brataas and I. Turek. Phys. Rev. B, 65, pp. 220401(R), 2002.

[10] E. Salhi and L. Berger, J. Appl. Phys., 76, pp. 4787-4792, 1994.

[11] B. A. Everitt, A. V. Pohm, and J. M. Daughton, J. Appl. Phys., 81, pp. 4020-4022. 1997.

[12] C. A. Ross, M. Farhoud, M. Hwang, et al., J. Appl. Phys., 89, pp.1310-1319. 2001.

[13] J. Yu, U. Rüdiger, L. Thomas, S. S. P. Parkin and A. D. Kent, J. Appl. Phys., 85, pp.5501-5503. 1999.

[14] R. P. Cowburn, D. K. Koltsov, A. O. Adeyeye, M. E. Welland and D. M. Tricker, Phy. Rev. Lett., 83, pp.1042-1045. 1999.

[15] J.-G. Zhu, Y. Zheng, and G. A. Prinz, J. Appl. Phys., 87, pp.6668-6673. 2000.

[16] L. Lopez-Diaz, J. Rothman, M. Klaui, and J. A. C. Bland, IEEE Trans Magn., 36(5), pp.3155-3157. 2000.

[17] J. Rothman, M. Klaui, L.Lopez-Diaz, et al. Phys. Rev. Lett., 86, pp.1098-1101. 2001.

[18] S. S. P. Parkin, Appl. Phys. Lett., 60, pp.512-514. 1992.

[19] C. Heide, P. E. Zilberman and R. J. Elliott, Phys. Rev. B 63, pp.064424. 2001.

[20] D. Y. Petrovykh, et al., Appl. Phys. Lett., 73, pp.3459-3461. 1998.

[21] M. D. Stiles, J. Appl. Phys., 79, pp.5805-5810. 1996.

[22] M. D. Stiles and D. R. Penn, Phys. Rev. B, 61, pp.3200-3202. 2000.

[23] S. Dubois, et al., Phys. Rev. B, 60, pp.477-484. 1999.

[24] L. Gan, S. H. Chung, K. H. Aschenbach, M. Dreyer, and R. D. Gomez, IEEE Trans Magn., 36(5), pp.3047-3049, 2000.

[25] M. J. Donahue and D. G. Porter <URL:http//math.nist.gov/oommf/>.

[26] J. Grollier, et al., J. Appl. Phys., 92, pp.4825-4827. 2002.

[27] J. L. García-Palacios and P. Svedlindh. Phys. Rev. Lett., 85, pp.3724-3727. 2000.

[28] A.Fert ***et al***, J. Magn. Magn. Mater. 272-276, pp.1706-1711. 2003 .

[29] B. Ozyilmaz, A. D. Kent, D. Monsma, J. Z Sun, M. J. Rooks and R. H. Koch, Phys. Rev. Lett. 91, pp.067203. 2003.

[30] Ya. B. Bazaliy, B. A. Jones and S. C. Zhang, Phys. Rev. B, 57, pp.R3213. 1998.

[31] A. Shpiro, P. M. Levy and S. Zhang, Phys. Rev. B, 67, pp.104430. 2003.

[32] A. Campbell and A. Fert, ***Ferromagnetic Materials***, edited by E. P. Vol. 3, Chap. 9, pp.751.Wolforth (North Holland, Amsterdam, 1982.

[33] J. Bass and W. P. Pratt Jr., J. Magn. Magn. Mater., 200, pp.274. 1999.

[34] K. Eid, R. Fonck, M. AIHaj Darwish, W. P. Pratt, Jr. and J. Bass, J. App. Phys., 91, pp.8102. 2002.

[35] A. Dinia, S. Zoll and K. Ounadjela, J. App. Phys., **75**, pp.6548. 1994.

[36] T. Ochiai, Y. Jiang, N. Tezuka, and K. Inomata (unpublished).

[37] Y. Jiang *et al.*, Phys. Rev. Lett., 92, pp.167204. 2004.

[38] S. Urazhdin, Norman O. Birge, W. P. Pratt, Jr. and J. Bass, Appl. Phys. Lett. 84, pp.1516. 2004.

Chapter 5 Combined Ballistic and Diffusive Model of Spin-polarized CIMS in PSV Structure and its Application

5.1 Introduction

CIMS makes possible the development of magnetic random-access memories (MRAM), which are controlled by the spin-transfer effect rather than by an external magnetic field. In chapter 4, we have discussed the magnetization switching mechanism and properties of the ring-shaped pseudo spin valve structure induced by spin-polarized current, which considers the effects of both the Oersted from the current itself and spin torque, which is equivalent to an effective field and is related to the longitudinal spin accumulation at the interface. In addition, we examine the spin-transport and spin transfer switching in magnetic multilayers, which considers both transverse and longitudinal spin accumulation where we considered the effect of the spin-dependent reflection and transmission at the interfaces, and transverse spin accumulation. All these previous analysis are confined to the purely diffusive transport regime. However, in the interfacial regions, the diffusive treatment of electron spin transport is not valid anymore, which means that the model considered in section 4.3 needs to be modified. It is thus essential to introduce ballistic elements e.g. of the spin transport across the thin spacer layer of the spin valve structure, and across the interfaces. At the same time, the diffusive picture is still useful in describing the spin torque from the dual processes of spin relaxation and precession process within the free FM layer.

Zhang, Levy (ZL) *et al.* [1,2] proposed a diffusive spin transport model in which spin current is driven by both the gradient of spin accumulation and spin dependent conductivity and they found that the transverse $\mathbf{m}_{\perp}$ and longitudinal $\mathbf{m}$ spin accumulation experience different decay lengths. Crucially, the resulting torque on the local moments is naturally decomposed into two items i.e. the effective field considered by Heide, and the in-plane spin torque of Slonczewski and Berger. However, the ZL model is entirely diffusive, i.e. it considers only the average effect of spin-dependent scattering. While this may be a reasonable assumption within each PSV layer, it neglects the strong scattering which leads to spin-dependent transmission and specular reflection at the interfaces. The ZL model thus ignores a significant source of spin transfer to the free layer, i.e. the absorption of the transverse spin momentum [3] in the free layer in order to preserve spin balance.

In the flowing sections, we will first propose a modified transport model which combines the diffusive (ZL) approach to spin relaxation in the free layer, and the ballistic approach of Stiles *et al.* [3] to include the ballistic transport across the interfaces. Due to the small thickness of the spacer layer, we also incorporate the effects of multiple specular reflections at the two Co-Cu interfaces. This ballistic spin injection model considers spin-differential transmission and reflection probabilities at the two Co-Cu interfaces, and the effect of multiple reflections at the interfaces. Later, this model is used to re-calculate the spin transfer toque and critical current density at the Co/Cu/Co PSV structure with and without Ru layer, which could be compared with the results obtained in chapter 3 using purely diffusively model. At last, with the trend of the reducing Ic, the PSV structure with

perpendicular magnetization orientation is proposed and resultant spin torque is numerical calculated.

5.2 Combined Ballistic and Diffusive Model of Spin-polarized CIMS in PSV Structure

5.2.1 Model Definition

The structure under consideration in this section is a PSV structure consisting of a Co1(pinned)/Cu(spacer)/Co2(free) trilayer with the Co layers magnetized in an in-plane direction, while current flow is perpendicular to the plane of the layers. In the diffusive model [1] the spin current $\mathbf{j}_m$ (the difference between majority and minority spin currents) is driven by (i) the spin dependence of the conductivity of the material and (ii) the current due to the gradient of the spin accumulation **m**., i.e.

$$\mathbf{j}_m = b_{\mathrm{C}} j_e \mathbf{M}_d - 2D_0[\frac{\partial \mathbf{m}}{\partial x} - b_{\mathrm{C}} b_{\mathrm{D}} M_d (\mathbf{M}_d \cdot \frac{\partial \mathbf{m}}{\partial x})] \tag{5.1}$$

where x is the current direction, $b_{C,D}$ are the spin polarization of conductance and diffusivity, respectively, $\mathbf{M}_d$ is the unit vector which points in the direction of the local magnetization and D_0 is the diffusion constant. In CIMS, we are concerned with the dynamics of **m** and $\mathbf{M}_d$ in the free layer. The former is governed by a) the injected $\mathbf{j}_m$ and b) the precessional motion of **m** about the magnetization $\mathbf{M}_d$ of the free layer. Under quasistatic condition, the longitudinal component **m** (i.e. parallel to $\mathbf{M}_d$) decays with the usual characteristic spin diffusion length $l_{sdl} = \sqrt{2(1-b_C b_D) D_0 t_{sf}}$, where t_{sf} is the spin-flip relaxation time [1]. The transverse component $\mathbf{m}_{\perp}$ experiences an additional decay

length of $l_J = \sqrt{2hD_0/J_{sd}}$ where J_{sd} is the strength of the *s-d* interactions. **m** can be expressed as [1]

$$\begin{aligned}\mathbf{m}_\perp = \mathbf{m}_x(x) + i\mathbf{m}_y(x) = G_1 \exp\left(-\frac{x}{l_+}\right) + G_2 \exp\left(-\frac{x}{l_-}\right) \\ + i[-iG_1 \exp\left(-\frac{x}{l_+}\right) + iG_2 \exp\left(-\frac{x}{l_-}\right)]\end{aligned} \tag{5.2}$$

$$\mathbf{m} = m_z(x) = G_3 \exp\left(-\frac{x}{l_{sdl}}\right) \tag{5.3}$$

where $l_+^{-1} = \sqrt{\left(1/l_{sf}^2\right) - \left(i/l_J^2\right)}$ and $l_- = l_+^*$, and $G_{1,2,3}$ are constants to be determined by considering Equ (5.1), which acts as a boundary condition at the spacer-free layer interface. To do this, we substitute the ansatz of **m** [Equs (5.2) and (5.3)] into the right-hand side of Equ (5.1), while the left-hand side which denotes the injected spin current $\mathbf{j}_m$ entering the free layer, is to be obtained by considering the spin transport within the preceding pinned Co1 and Cu spacer layers, and at the Co1-Cu and Cu-Co2 interfaces.

We apply a ballistic model to describe spin injection at the two interfaces. In this model, we assume that an incident electron at an interface $x = x_0$ experiences a spin-differential reflection and transmission probability across the interface, so that the electron wavefunction for spins along the majority/minority direction can be expressed as

$$\left|y_\uparrow\right\rangle = \begin{matrix}\left(e^{ikx} + R_\uparrow e^{-ikx}\right)\left|\uparrow\right\rangle & x < x_0 \\ T_\uparrow e^{ikx}\left|\uparrow\right\rangle & x > x_0\end{matrix} \tag{5.4}$$

$$\left|y_\downarrow\right\rangle = \begin{matrix}\left(e^{ikx} + R_\downarrow e^{-ikx}\right)\left|\downarrow\right\rangle & x < x_0 \\ T_\downarrow e^{ikx}\left|\downarrow\right\rangle & x > x_0\end{matrix} \tag{5.5}$$

where the spinor axis is set by the free Co2 layer magnetization. If the electron spin is at an angle q $(\neq 0, p)$ to the Co2 magnetization, its wavefunction is an admixture of both majority and minority wavefunctions in Co2, i.e.

$$y = e^{-ip/4}\cos(q/2)\left|y_{\uparrow}\right\rangle + e^{ip/4}\sin(q/2)\left|y_{\downarrow}\right\rangle \tag{5.6}$$

From the electron wavefunction, the charge current density and spin current density can respectively be evaluated as [3]

$$j(x) = -\frac{i\mathbf{h}}{2m}\sum_{s}\left[y_s^{*}\frac{\partial}{\partial x}y_s + h.c.\right] \tag{5.7}$$

$$[\mathbf{J}]_{m,n} = -\frac{i\mathbf{h}^2}{4m}\sum_{s,s'}\left[y_s^{*}[s_m]_{s,s'}\otimes\frac{\partial}{\partial x_n}(y_{s'}) + h.c.\right] \tag{5.8}$$

where the summation is over both spin directions s, and s_m is the vector of Pauli spin matrices. The spin current is denoted by a tensor $\mathbf{J}$ such that $[\mathbf{J}]_{m,n}$ represents flux of electrons having spin orientation m, along the x_n direction $[(x_1, x_2, x_3) \equiv (x, y, z)]$. From $\mathbf{J}$, we can thus define a vector denoting spin polarization ratio of current flowing in the x direction as

$$\mathbf{j}(x) = \frac{2}{\mathbf{h}}[\mathbf{J}(x).\hat{\mathbf{x}}] = \frac{2}{\mathbf{h}}[J_{11}(x), J_{21}(x), J_{31}(x)]. \tag{5.9}$$

In the ballistic spin injection at the Co1-Cu spacer interface, the incident current traveling through the pinned Co1 layer is spin polarized along the Co1 magnetization, with a polarization ratio of b_{Co} of bulk Co. The electron wavefunction is

$$\left|y\right\rangle = [b_{Co}\cos q + (1-b_{Co})\sin q]\left|y_{\uparrow}\right\rangle + [b_{Co}\sin q + (1-b_{Co})\cos q]\left|y_{\downarrow}\right\rangle \tag{5.10}$$

At the interface, one component of the incident spin current is reflected back into the Co1 layer, another component is transmitted into the Cu spacer while the remainder is

absorbed at the interfacial zone. Based on Equs (5.4)-(5.10), the incident/transmitted/ reflected current density ($j_{inc}/j_t/j_r$) and spin polarization current ($\mathbf{j}_{inc}/\mathbf{j}_t/\mathbf{j}_r$) can be calculated. By defining a unit polarization vector $\mathbf{p} = \mathbf{j}/j$, the absorbed spin current at the pinned Co-Cu interface is given by

$$\mathbf{j}_{abs} \equiv \mathbf{p}_{abs} j_{abs} = \mathbf{p}_{inc} j_{inc} - \mathbf{p}_t j_t - \mathbf{p}_r j_r \tag{5.11}$$

The transmitted spin current $\mathbf{p}_t j_t$ decays with a spin diffusion length of Cu l_{Cu} within the nonmagnetic Cu layer. Unlike in the Co2 layer, there is only one characteristic decay length for all spin orientations in Cu layer. Thus there is only a decrease in magnitude but no change in the spin direction as the spin current traverses the thickness t_{Cu} of the Cu layer. At the Cu-Co2 interface, the spin current is reduced to

$$\mathbf{j}_{Cu} = \mathbf{p}_t j_t \exp(-t_{Cu}/l_{Cu}) \tag{5.12}$$

$\mathbf{j}_{Cu}$ undergoes a similar spin-dependent reflection and transmission process at the Cu-Co2 interface as that occurring at the Co1-Cu interface. The reflected component will travel in the reverse direction back into the Cu layer. Due to the long spin diffusion length of Cu compared to the spacer thickness, the reflected spin current maintains a high degree of its initial value when it arrives at the Cu-Co1 interface. Thus, the spin-filtering processes at the two Co-Cu interfaces are not entirely independent of each other and so we need a self-consistent approach to account for the effect multiple scattering of spin current at both interfaces.

We now evaluate $\mathbf{j}_t$ and $\mathbf{j}_{abs}$ at the Cu-Co2 interface, which will contribute to the spin transfer and spin torque in the Co2 layer. An angle of $p/4$ is assumed between the magnetization of the free and pinned layers. After the incident spin current has undergone

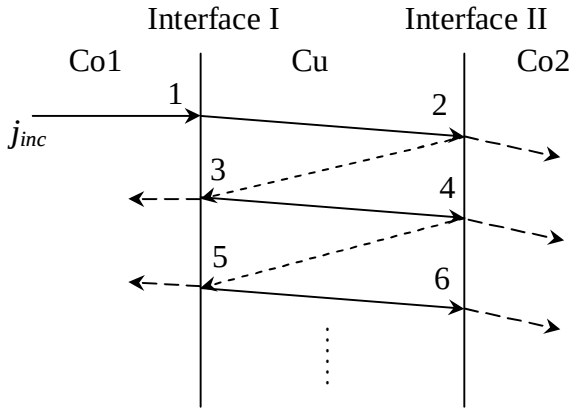

Figure 5.1 Schematic diagram of the spin polarized current transport across the Co1/Cu/Co2 PSV multilayer, with multiple specular reflections at the two Co-Cu interfaces. The number of transmission/reflections experienced by the charge and spin currents is indicated at the interfaces.

$m = 2n$ reflections [n reflections each at (Co1-Cu) and (Cu-Co2) interfaces, as shown in Fig 5.1], the absorbed and transmitted spin current at interface II is given by

$$\mathbf{p}_{\text{abs}}^{(m)} j_{\text{abs}}^{(m)} = (\mathbf{I} - C_2\mathbf{A}_2 - D_2\mathbf{B}_2)\cdot(D_1D_2\mathbf{B}_1\mathbf{B}_2)^{n-1}\cdot\mathbf{A}_0\cdot\mathbf{p}_{\text{inc}}^{(0)}C_0 j_{\text{inc}}^{(0)} \tag{5.13a}$$

$$\mathbf{p}_{\text{t}}^{(m)} j_{\text{t}}^{(m)} = C_2\mathbf{A}_2\cdot(D_1D_2\mathbf{B}_1\mathbf{B}_2)^{n-1}\mathbf{A}_0\cdot\mathbf{p}_{\text{inc}}^{(0)}C_0 j_{\text{inc}}^{(0)} \tag{5.13b}$$

where $\mathbf{p}_{\text{inc}}^{(0)} = (0, \sin q, \cos q)$, $\mathbf{I}$ is a unit matrix, $\mathbf{A}_0$ and $\mathbf{B}_0$ are (3×3) spin transfer matrices and C_0, D_0 are charge transfer functions of q (the angle between the spin polarization vector and the spinor axis), which govern the initial spin current injection across interface I, while $\mathbf{A}_{1,2}$, $\mathbf{B}_{1,2}$ and $C_{1,2}$, $D_{1,2}$ are the corresponding matrices and functions at Cu-Co1 and Cu-Co2 interfaces, respectively, during subsequent specular reflections. They are defined as $\mathbf{p}_{\text{t}}^{(m)} = \mathbf{A}\cdot\mathbf{p}_{\text{inc}}^{(m-1)}$, $\mathbf{p}_{\text{r}}^{(m)} = \mathbf{B}\cdot\mathbf{p}_{\text{inc}}^{(m-1)}$, $j_{\text{t}}^{(m)} = Cj_{\text{inc}}^{(m-1)}$ and $j_{\text{r}}^{(m)} = Dj_{\text{inc}}^{(m-1)}$. In this calculation of PSV structure, these two sets of matrices (functions) are the same because both the free and pinned layers are made of Co. The initial value of $q_0 = p/4$, i.e. incident

electrons first incident at the Co1-Cu interface are polarized along the pinned layer magnetization. Subsequent spin orientations are given by

$$q_1 = \arctan\left(\frac{\left[\mathbf{p}_t^{(0)}\right]_y}{\left[\mathbf{p}_t^{(0)}\right]_z}\right),\ q_m = \arctan\left(\frac{\left[\mathbf{p}_r^{(m-1)}\right]_y}{\left[\mathbf{p}_r^{(m-1)}\right]_z}\right),\quad (m>1) \tag{5.14}$$

while the incoming charge currents are given by

$$j_{\text{inc}}^{(0)} = (1,0,0),\ j_{\text{inc}}^{(1)} = j_t^{(0)}\exp\left(-\frac{t_{Cu}}{l_{sf}}\right),\ j_{\text{inc}}^{(m)} = j_{\text{r}}^{(m-1)}\exp\left(-\frac{t_{Cu}}{l_{sf}}\right)(m>1) \tag{5.15}$$

The specular reflections at the two interfaces are continued until the ratio between the transmitted spin current at the *m*th reflection is less than some preset fraction of the original spin current, i.e. $\frac{\mathbf{p}_t^{(\text{m})} j_{\text{t}}^{(\text{m})}}{\mathbf{p}_t^{(0)} j_{\text{t}}^{(0)}} \le 10^{-5}$. After $m = 2n$ reflections, the total absorbed spin current $\mathbf{j}_{\text{abs}}$ at the two interfaces is the sum of absorbed spin currents at alternate reflections. Thus, $\mathbf{j}_{\text{abs}}$ at the Co1-Cu and Cu-Co2 interfaces are respectively

$$\mathbf{j}_{\text{abs}}^{(\text{I})} = \sum_{k=1}^{n} j_{\text{abs}}^{(2k-1)}\mathbf{p}_{\text{abs}}^{(2k-1)},\quad \mathbf{j}_{\text{abs}}^{(\text{II})} = \sum_{k=1}^{n} j_{\text{abs}}^{(2k)}\mathbf{p}_{\text{abs}}^{(2k)} \tag{5.16}$$

A torque is exerted on the moments of the free Co2 layer due to the transverse component of the absorbed spin current $\mathbf{j}_{\text{abs},\perp}^{(\text{II})}$ at Cu-Co2 interface. The absorbed torque per moment is then given by

$$\frac{\left(\mathbf{j}_{\text{abs},\perp}^{(\text{I})}/e\right)\times A\times(\mathbf{h}/2)}{M_s\times A\times t_{\text{Co2}}} = \frac{\left(\mathbf{j}_{\text{abs},\perp}^{(\text{I})}/e\right)\times(\mathbf{h}/2)}{M_s t_{\text{Co2}}} \equiv u_{\text{abs}}\hat{\mathbf{y}} + v_{\text{abs}}\hat{\mathbf{x}} \tag{5.17}$$

where A is the cross-sectional area, t_{Co2} the free layer thickness, and u_{abs} (v_{abs}) denotes the in-plane and out-of-plane components of the torque. We neglect the effect of $\mathbf{j}_{\text{abs}}^{(\text{I})}$ on the pinned Co1 layer.

Another contribution to the spin torque in the free layer arises from the relaxation of the transmitted spin current $\mathbf{j}_t^{(II)}$ in the free layer, as described in Equ (5.1). As explained earlier [c.f. Equs (5.2) and (5.3)], this relaxation has a characteristic decay length of l_{sdl} for the longitudinal spin component, and $l_{\pm}$ for the transverse component. For a ferromagnetic material like Co, typically $l_J << l_{sf}$ [2], so that the transverse relaxation length is largely determined by l_J, i.e. $|l_{\pm}| \approx l_J$ which is significantly smaller than the normal spin diffusion length l_{sdl}. Substituting $\mathbf{j}_t^{(II)}$ and the ansatz of Equs (5.2) and (5.3) into the left- and right-hand side of Equ (5.1), respectively, and equating all three components of the spin current across both sides of interface II, we obtain the following equations

$$-2D_0\left(\frac{G_1}{l_+}+\frac{G_2}{l_-}\right)=\left[\mathbf{j}_t^{(II)}\right]_x \equiv 0\,, \tag{5.18a}$$

$$2iD_0\left(-\frac{G_1}{l_+}+\frac{G_2}{l_-}\right)=-\left[\mathbf{j}_t^{(II)}\right]_y \equiv -j_t \sin q' \equiv -j_t d \sin q_0\,, \tag{5.18b}$$

$$b\, j_t - 2D_0(1-b_C b_D)\left(-\frac{G_3}{l_{sdl}}\right)=\left[\mathbf{j}_t^{(II)}\right]_z \equiv j_t \cos q' \equiv j_t e \cos q_0\,, \tag{5.18c}$$

where j_t is the magnitude of the in-plane (i.e. *y*-*z* plane) component of $\mathbf{j}_t^{(II)}$, q' is the angle this in-plane component makes with the free layer magnetization. In order to express our answers in terms of the macroscopic angular deviation between the free and pinned layer magnetizations q_0, we introduce additional factors d and e which are given,

respectively, by $d=(\sin q'/\sin q_0)$ and $e=(\cos q'/\cos q_0)$. From Equs (5.18a-c), we determine the constants $G_{1,2,3}$ to be

$$G_1=\frac{j_t l_+ d\sin q_0}{4iD_0} \tag{5.19a}$$

$$G_2=-\frac{j_t l_- d\sin q_0}{4iD_0} \tag{5.19b}$$

$$G_3=-\frac{j_t l_{sdl}[b-e\cos q_0]}{2D_0(1-b_c b_d)} \tag{5.19c}$$

Only the transverse components G_1 and G_2 will give rise to an in-plane (out-of-plane) torque on the local moments within free Co layer. This current-induced torque per moment can be written as

$$\begin{aligned} \mathrm{G} &= \mathbf{M}_d^{(2)}\times\left(\frac{J_{sd}}{M_s}\mathbf{m}_\perp\right)=\left(\frac{J_{sd}}{M_s}m_x\right)\mathbf{M}_d^{(1)}\times\left(\mathbf{M}_d^{(2)}\times\mathbf{M}_d^{(1)}\right)+\left(\frac{J_{sd}}{M_s}m_y\right)\mathbf{M}_d^{(1)}\times\mathbf{M}_d^{(2)} \\ &\equiv u\mathbf{M}_d^{(1)}\times\left(\mathbf{M}_d^{(2)}\times\mathbf{M}_d^{(1)}\right)+v\mathbf{M}_d^{(1)}\times\mathbf{M}_d^{(2)} \end{aligned} \tag{5.20}$$

In the evaluation of the coefficients u_t and v_t, the coefficients $G_{1,2}$ are averaged over t_{Co2} i.e.

$$\langle G_{1,2}\rangle=\frac{1}{t_{\mathrm{Co2}}}\int_0^{t_{\mathrm{Co2}}}G_{1,2}(x)\,\mathrm{d}x \tag{5.21}$$

Based on the analysis in Ref. 1, the effective magnetic field in the in-plane and out-of-plane orientations due to spin torque are given by

$$u_t=-\frac{hj_t v_0 d}{egm_B t_{Co2}}\left[1-\cos(x)e^{-x}\right] \tag{5.22a}$$

$$v_t=\frac{hj_t v_0 d}{egm_B t_{Co2}}\sin(x)e^{-x} \tag{5.22b}$$

where $x = t_{Co2}/\sqrt{2}\,l_J$, and $v_0 = 0.5a_0^2 c_0 \sin 60°$ is volume per Co atom = half the hcp unit cell volume (a_0 = 0.251nm and c_0 =0.409nm being the lattice constants), and g = 1.725 is the moment per Co atom in units of the Bohr magneton m_B.

5.2.2 Spin Torque Calculation and Discussion

In this section, we obtain a numerical estimate of the spin torques within the Co1/Cu/Co2 PSV structure, based on typical experimental parameters of t_{Co1} = 10 nm, t_{Cu} = 6 nm, t_{Co2} = 3 nm and known experimentally determined values of spin polarization ratio in Co $h_{Co} \approx 38\%$ [4], spin diffusion lengths $l_{sdl}^{Cu} \approx 140$ nm, $l_{sdl}^{Co} \approx 60$nm and $l_J^{Co} \approx 3$nm, and transport parameters at the Co-Cu interface [5], i.e. $T_{\uparrow(\downarrow)}^{Co\text{-}Cu} = 0.73$ (0.54), $R_{\uparrow(\downarrow)}^{Co\text{-}Cu} = 0.27$ (0.46), $T_{\uparrow(\downarrow)}^{Cu\text{-}Co} = 0.94$ (0.33) and $R_{\uparrow(\downarrow)}^{Cu\text{-}Co} = 0.06$ (0.67). Substituting these parameters into Equs (5.7) to (5.16), we found that the spin polarization vector of current undergoes a change across the Co1-Cu interface from (0, 0.71, 0.71) to (0, 0.56, 0.82), i.e. an in-plane rotation of the spin polarization direction from 45° to 34.1°, while the magnitude of the spin current is reduced to $0.479j_{m0}$ where $j_{m0} = b_{Co} j_e$, the original incident value in the bulk Co1 layer (as shown in Fig 5.2). Within the Cu layer, the spin current maintains its orientation while its magnitude decays exponentially over t_{Cu} with decay length l_{sdl}^{Cu}. After the ballistic transmission across the Cu-Co2 interface, the transmitted spin current $\mathbf{j}_t$ into the free Co2 layer has a polarization vector of (0, 0.21, 0.978) (i.e. directed at 12.2°) and a magnitude of $0.39j_{m0}$. By considering Equ (5.16), the calculated absorbed spin current $\mathbf{j}_{abs}^{(II)}$ at this interface is found to have a magnitude of

0.174 j_{m0} and is oriented perpendicular to the free Co2 layer magnetization. Thus, $\mathbf{j}_{abs}$ is a significant contributor to the total spin momentum transfer to the local moments of the free layer in addition to the relaxation of the transverse spin components of $\mathbf{j}_t$. However, this contribution has been neglected by the fully diffusive model of Ref. 12, while the fully ballistic model of Ref. 10 neglects the spin relaxation of $\mathbf{j}_t$ in the free layer. By combining both contributions, the in-plane and out-of-plane components of the effective field due to the spin torques are calculated to be $u = 121.6$ Oe (compared to 108 Oe if $\mathbf{j}_{abs}$ has been ignored) and $v = 181$ Oe, for $j_e = 10^7$ A/cm^2. Considering previous experimental studies of the pseudo-spin-valve Co/Cu/Co structure, the critical magnetic fields to switch the free layer are mostly in the range of 300 Oe to 1kOe [6,7]. From our model, these fields correspond to the injected electron current density of $j_e = 2.5\times10^7$ A/cm^2 to 8.2×10^7 A/cm^2. These results are consistent with the actual CIMS experiments, for which the critical current density is observed to be of the order of 10^7 A/cm^2. In this analysis, only the in-plane component of the spin torque u is considered, while the effect from the out-of plane component v is ignored due to the small thickness of the free layer, which makes it highly improbable for switching to occur along that direction.

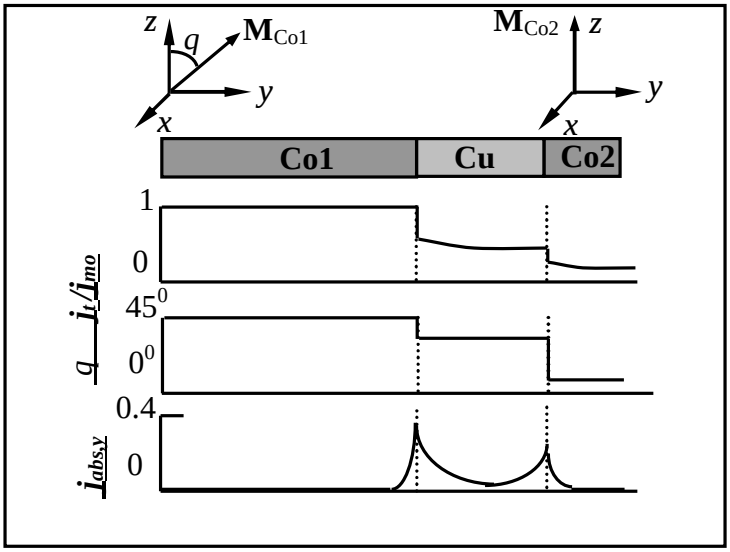

Figure 5.2 Plots of the magnitude of transmitted spin current j_t, the angle q of the spin current with respect to the free layer magnetization and the absorbed transverse spin current $j_{abs,\,y}$ (in units of the bulk spin-polarized current in pinned Co layer j_{m0}) across a Co/Cu/Co PSV multilayer, with non-collinear magnetization.

5.2.3 Conclusions

In conclusion, we have presented a spin transport model to calculate the current-induced spin torque in the free layer of a PSV trilayer (Co/Cu/Co) structure. The model incorporates ballistic spin-dependent transmission/reflection of electrons at the Co-Cu interfaces, and the diffusive relaxation of spin accumulation within the free layer. The resultant injected spin current into the free layer is obtained by considering multiple reflections at the Co1-Cu and Cu-Co2 interfaces. Based on known experimental parameters, a significant absorption of spin current occurs as a result of specular reflections at the Cu-Co2 interface. This absorbed spin current provide an extra source of spin torque to the Co2 layer in addition to the spin torques arising from the relaxation of the transverse spin accumulation, which has been considered in previous diffusive models.

By considering the Landau-Lifshitz-Gilbert (LLG) equation, the strength of the spin torque is quantified by evaluating the resultant effective fields in the in-plane and out-of-plane directions. Based on the typical experimental results of switching magnetic field of Co/Cu/Co trilayers, the resultant critical electron current density required to switching the magnetization direction of free Co layer is evaluated to be in the order of the $10^7 A/cm^2$, which is in good agreement with CIMS experimental results. Since interfacial specular reflections has a contribution to the total spin torque, this suggests that new material and device designs which enhance spin filtering effects at the interfaces of a PSV structure, can help reduce the critical current density for CIMS.

5.3 Application of Combined Model in PSV Structure with and without Ru Cap Layer

In the previous section, a combined ballistic and diffusive model has been presented to analyze the spin current transport and spin torque effective in the normal three-layer PSV structure and the critical switching current I_c is evacuated to be in the order of the 10^7 A/cm^2, which is in good agreement with CIMS experimental results. However, for the practical application of current-induced switching in PSV structures, it is essential to investigate ways of further reducing I_c. Thus in this section, we will analyze the spin torque effect in the spin valve magnetic multilayers with Ru cap layer so as to explore its possibility of reducing Ic and also test the general accuracy and efficiency of the combined model.

5.3.1 Structure Introduction

In most experimental pseudo-spin-valve (PSV) structures, the lead layer is made up of by Cu, which has a long spin diffusion length of about 60nm. So the resulting distributed spin torque at this free FM/lead layer interface is very small and can be neglected. Thus the spin transport analysis in the pseudo spin valve with a Cu lead could be stopped at the free FM layer. However, in this section, we will consider an alternative device structure where a ruthenium (Ru) layer is inserted in between the Co2 layer and Cu lead layer which has been first introduced in section 4.3 of chapter 4. It is also known that the Ru layer constitutes a "wall" of spin scatterers, which strongly acts on the majority spins and results in a much larger spin accumulation at the Co2/Ru interface. The detailed of the numerical calculation of the spin current transport at the Co2/Ru interfacial zone is similar to those at the first two interfaces, which has been described in detail in the previous section. From the previous analysis, the total torques exerted on the magnetic moments of the free Co2 layer is the sum of the spin torque at the two interfaces of Cu/Co2 and Co2/Ru.

We can obtain a numerical estimate of the spin polarization of current within the pseudo spin valve structure with and without Ru layer, based on known experimental values of parameters. However for Co/Ru interface, there is no experimental report on the transmission and reflection probabilities. Since it is a known fact that the majority spins are scattered more than the minority spins at this interface, it is thus reasonable to assume $b_{\uparrow,Co-Ru} = a/2$ and $b_{\downarrow,Co-Ru} = 0.5 + b/2$, where a and b are two independent variables ranging from 0 to 1. The thickness of the spin valve multilayers are chosen to be T_{Co1} = 10

nm, T_{Cu} = 6 nm, T_{Co2} = 3 nm and T_{Ru} = 0.45 nm. Based on the above parameters, we can thus calculate the numerical magnitude of the transmitted reflected and absorbed current at each interfacial zone and within each layer.

5.3.2 Spin Torque Calculation and Discussion

Based on the analysis presented in the previous section, we can evaluate the absorbed spin currents and the transverse spin accumulation at the crucial Cu/Co2 and Co2/Ru interfaces. The transverse component of the absorbed spin current $\mathbf{j}_{\text{abs},\perp}^{Cu-Co2}$ at Cu-Co2 and $\mathbf{j}_{\text{abs},\perp}^{Co2-Ru}$ at Co2-Ru interface gives rise to a spin torque on the moments of the free Co2 layer. The absorbed torque per moment is given by

$$\frac{\left(\mathbf{j}_{\text{abs},\perp}^{(\text{I})}/e\right)\times A\times(\mathbf{h}/2)}{M_s\times A\times t_{\text{Co2}}}=\frac{\left(\mathbf{j}_{\text{abs},\perp}^{(\text{I})}/e\right)\times(\mathbf{h}/2)}{M_s t_{\text{Co2}}}\equiv u_{\text{abs}}\hat{\mathbf{y}}+v_{\text{abs}}\hat{\mathbf{x}} \tag{5.23}$$

where $\mathbf{j}_{\text{abs},\perp}$ is $\mathbf{j}_{\text{abs},\perp}^{Cu-Co2}$ or $\mathbf{j}_{\text{abs},\perp}^{Cu-Co2}+\mathbf{j}_{\text{abs},\perp}^{Co2-Ru}$ for PSV without or without Ru capping layer, respectively, A is the cross-sectional area, T_{Co2} the free layer thickness, and u_{abs} (v_{abs}) denotes the in-plane and out-of-plane components of the spin torque. Another contribution to the spin torque in the free layer arises from the relaxation of the transmitted spin current in the free Co2 layer and the current-induced torque per moment can be written as

$$\begin{aligned}\text{G} = \mathbf{M}_{Co2}\times\left(\frac{J_{sd}}{M_s}\mathbf{m}_{\perp}\right)&=\left(\frac{J_{sd}}{M_s}m_x\right)\mathbf{M}_{Co1}\times\left(\mathbf{M}_{Co2}\times\mathbf{M}_{Co1}\right)+\left(\frac{J_{sd}}{M_s}m_y\right)\mathbf{M}_{Co1}\times\mathbf{M}_{Co2}\\&\equiv u_t\mathbf{M}_{Co1}\times\left(\mathbf{M}_{Co2}\times\mathbf{M}_{Co2}\right)+v_t\mathbf{M}_{Co1}\times\mathbf{M}_{Co2}\end{aligned} \tag{5.24}$$

where M_s is the saturation magnetization and measured to be 1.4×10^6 A/m for Co and u_t and v_t can be evacuated. These spin torques will try to align the magnetization of the free

Co2 layer parallel or antiparallel to the magnetization direction of the pinned Co1 layer, depending on direction of the spin current.

In this analysis, we assume the angle q_0 between Co1 and Co2 layers varies ranging from 0° to 180° in the plane of the multilayers. We found that without the Ru layer, i.e., without consideration of the spin torques at the Co2/Ru interface the critical currents, the spin torques from the absorbed current are $u_{abs} = 12$ Oe and $v_{abs} = 28$ Oe while those from the transmitted spin current are $u_t = 88$ Oe and $v_t = 217$ Oe for j_e = 10^7A/cm^2 and θ_0=45°. With the presence of the Ru layer adjacent to the Co2 layer, the total distributed torque exerted on the Co2 layer increases to $u_{abs} = 18$ Oe, $v_{abs} = 93$ Oe $u_t = 104$ Oe and $v_t = 340$ Oe for a=b=0.5. The in-plane and out of plane components increases by a factor of 1.22 and 1.77, respectively. If we assume that both the in-plane and out of plane spin torques contribute equally to the magnetization switching, then there would be a decrease in the critical current density by a factor of around 1.5.

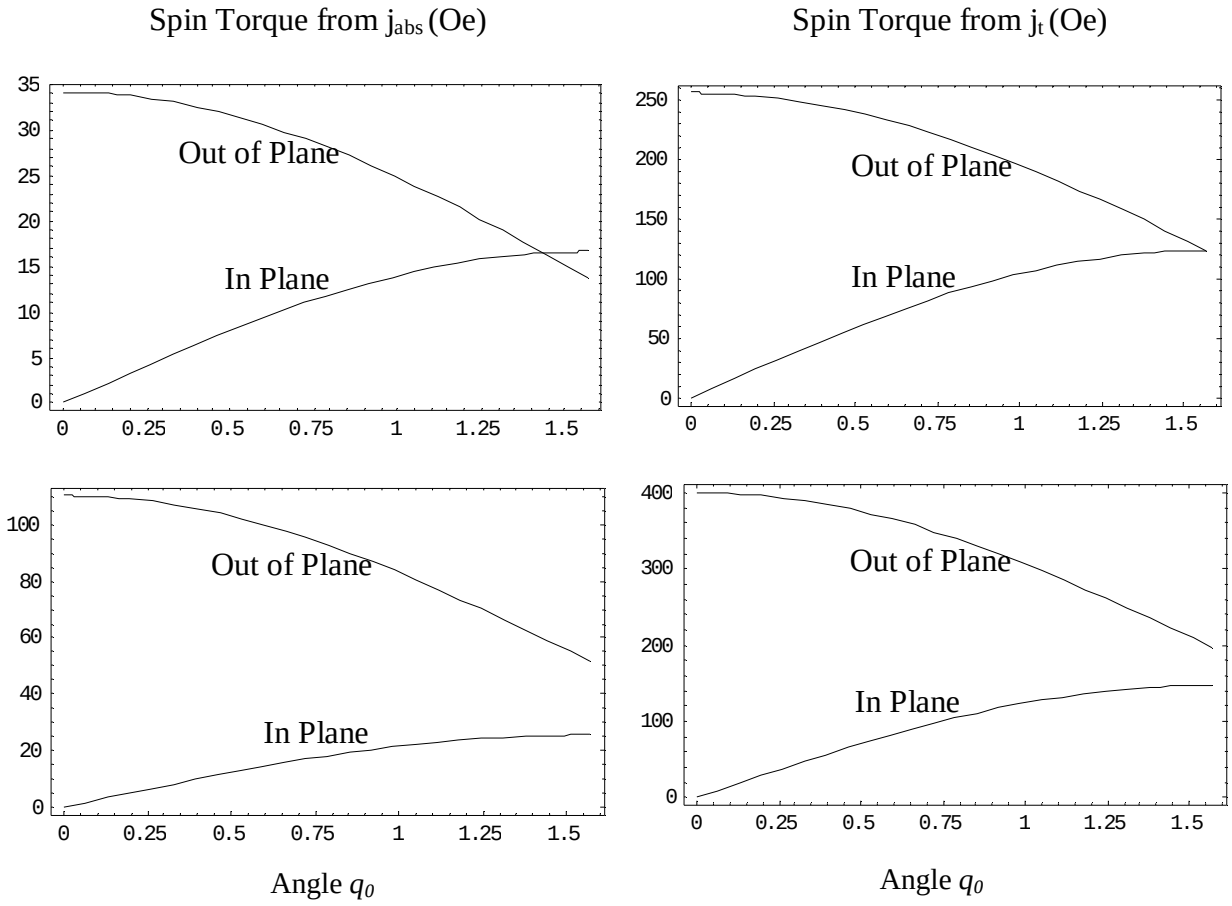

Figure 5.3 Variation of in- and out-of plane spin torques from absorbed j_{abs} (left) and transmitted j_t (right) spin currents as the function of the angles θ_0 between the magnetization direction of the pinned and free Co layers for Co/Cu/Co pseudo spin valve structure without (upper) and with (bottom) Ru capping layer, respectively.

In Figure 5.3, the resultant effective field arising from all spin torque contributions, i.e. u_t, u_{abs}, v_t and v_{abs} are plotted as a function of the angular deviation q_0 between the magnetization direction of the pinned and free Co layers in the PSV structures with and without the Ru capping layer where the electron current density is assumed to be $10^7 A/cm^2$ and the two variables a and b are assumed to be 0.5. From Equ (5.24), we know that the in-plane spin torque is in the plane of the y-z directions, i.e. the plane of M_{Co1} and M_{Co2}, which will try to rotate the magnetization direction of the free FM layer towards the

direction of the pinned Co1 layer. The out-of plane spin torque on the other hand, is in the direction of perpendicular to both M_{Co1} and $M_{Co2,}$ which produces a processional motion about M_{Co2}, similar to the effect of an effective field H_{eff} in the usual LLG equation. From Fig 5.3, we can observe both in-plane spin torques increase as the initial angle θ_0 between the two FM layers increase while out-of plane spin torque decrease as θ_0 increase. In addition, the magnitude of the spin torques from the absorbed spin current j_{abs} ranges from 0 to 120Oe. Although, this is generally smaller than that arising from the spin relaxation of the transmitted spin current, it still constitutes a significant contribution to the total spin momentum transfer. Comparing the spin torques for PSV with and without the Ru layer, we find that both the in-plane and out-of plane spin torques increase after we adding a Ru capping layer. For PSV structures with Ru layer, the total spin torque contribution from the absorbed current is more prominent than those without Ru, which is due to the large spin memory loss at the Co2/Ru interfacial zone.

Since the transmitted/reflection probability at the interfacial zones is a critical factor of the resultant spin torques, we thus investigate the magnitude of the spin torque as a function of the transmission probability for up spins at the Co2/Ru interface with *b* assumed to be 0.5 and θ_0 set at 45° (Fig 5.4). As the transmission probability for spin up electrons (i.e. *a*) increases, both the in-plane and out-of-plane spin torques decrease in magnitude. This is because when *a* is small, i.e. most of the spin-up electrons are either reflected or absorbed at the Co2/Ru interface, a large spin accumulation and spin absorption occur at the interface due to the ballistic specular reflection process, thus resulting in a large spin torque.

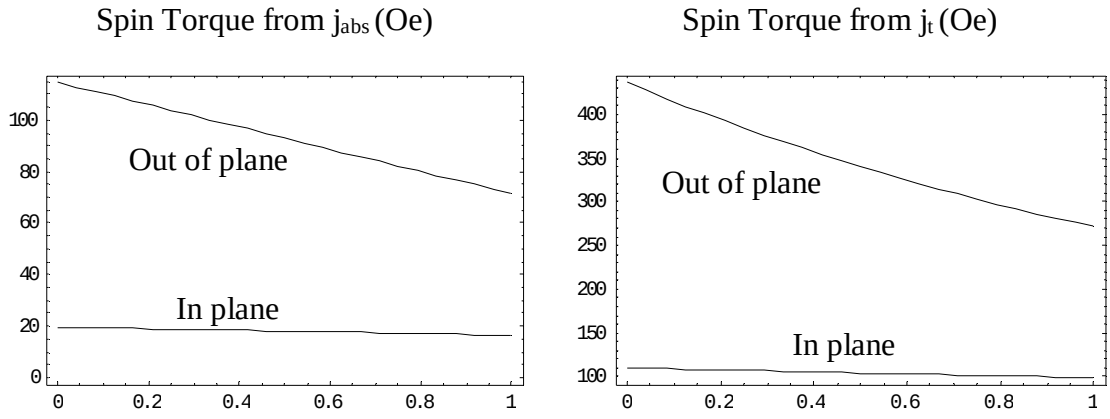

Figure 5.4 Plot of the spin plane and out of plane spin torques from absorbed j_{abs} (left) and transmitted j_t (right) spin currents as the function of the variable a, where we assume $\theta_0=45^0$ and b=0.5.

Considering previous experimental studies of the pseudo-spin-valve structure, the critical magnetic fields to switch the free layer are mostly in the range of 300Oe to 1kOe [6,7]. In our model, these magnetic fields correspond to the injected electron current density of j_e is approximately in the range of 1.7 to $5.8\times10^7 Acm^{-2}$. Thus our data are generally consistent with the experimental and theoretical results of other models. The reduction of the critical current density by a factor of 1.5 times with the insertion of Ru layer, which is in reasonable agreement with Dr. Ochiai's [8] experimental results obtained from Co/Cu/Co PSV structures. Their results indicated that the insertion a Ru layer, reduces the critical current density j_c by a factor of not more than 2 times.

5.3.3 Conclusions

For the practical application of current-induced switching in PSV structures, it is essential to investigate ways of further reducing the critical switching current. There are three main factors, which control the magnitude of the absorbed transverse spin current, which determines the size of the spin torque. These are i) the intrinsic spin polarization ratio of the ferromagnetic material in the pinned layer, ii) the spin-dependent transmission and reflection probability at the interfaces and iii) the amount of spin relaxation within the nonmagnetic spacer. From the above analysis, It is clear that the incorporation of a strong spin-scatterer material with a short spin diffusion length and high majority spin reflection coefficient between the PSV trilayer and the lead electrode is one of the ways to further decreasing Ic and further works are desired in this area. Thus in the previous sections, we have analyzed the spin current transport and spin torque effect in the PSV with a Ru cap layer and our results indicated that the insertion of Ru cap layer will result in a large spin accumulation at the free/cap layer interface and the reduction of the critical current density Ic by a factor of not more than 2 times.

5.4 Spin Torque in Co/Cu/Co with Perpendicular Magnetic Anisotropy

5.4.1 Structure Introduction

In the previous sections, we have proposed a combined model to study the spin transport and spin torque effect of CIMS in magnetic multilayers with in-plane magnetization. For MRAM applications, having multilayers which are magnetized in the in-plane direction poses several disadvantages, e.g. requiring an aspect ratio (length/width)

of greater than 2 to enhance shape anisotropy for magnetic stability, and reduction of magnetization curling at the edges [9]. However, in order to achieve high-density MRAM, the bit cell size has to be reduced to submicron range, and this requires a low aspect ratio, which is more easily achieved in a perpendicular magnetized MRAM. Previous experimental works have succeeded in inducing perpendicularly magnetized multilayers in Co on Au(111) and Cu(111) substrates, and Fe on Cu(111), Cu(100), Cu(110), Au(100) and Pd(100) substrates, for FM layer thickness below a certain critical thickness, ranging from 2 to 7 monolayers (ML) [9-13]. In 10ddition, capping the Co thin film layer with Cu could enhance the perpendicular anisotropy, and extend the critical thickness [14]. The magnetic properties of spin valve and MTJ devices with perpendicularly magnetized film have been studied under the application of magnetic field. But as far as we are aware, there has been no report as yet of CIMS study involving perpendicularly magnetized MRAM structure. In this section, we will analyze the spin-transport and the resulting spin torque effect in perpendicularly magnetized spin valve, and predict the critical current for CIMS induced by the spin torque.

The structure under consideration is a pseudo spin valve structure consisting of a Cu/Co1(pinned)/Cu(spacer)/Co2(free)/Cu(111) multilayer with current flow in a perpendicular to plane of the layers. The two Co layers are assumed to be magnetized in the out-of plane direction with angle q_0 between $\boldsymbol{M}_{Co1}$ and $\boldsymbol{M}_{Co2}$, respectively, as shown in Fig 5.5. The bottom Cu (111) ensures an fcc crystal structure within the Co films, which induces a perpendicular easy axis. A Cu cap layer is added to increase this perpendicular anisotropy. The thicknesses of Co1, Cu and Co2 layers are set at 3ML, 4ML and 3ML,

respectively, and the monolayer thickness for Cu and Co is estimated to about 2.09 Å [15]. The thickness of both Co layers is below the critical thickness for maintaining a perpendicular anisotropy. Due to the small thickness of the multilayers, the spin transport is dominated by the spin-dependent specular scattering at the two Co/Cu interface. A ballistic free electron model is used to describe spin transport at the two interfaces.

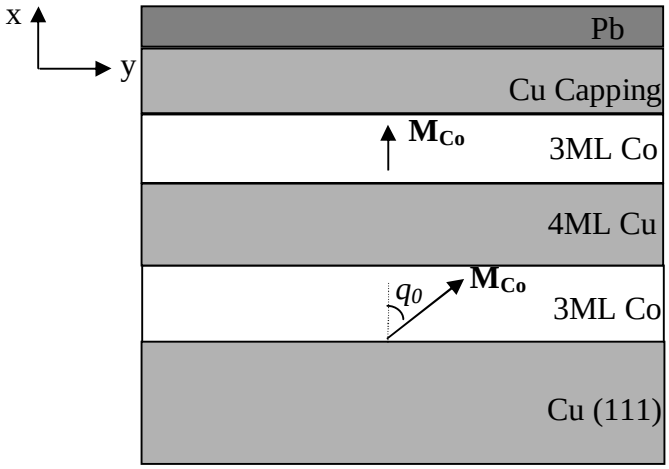

Figure 5.5 Schematic diagram of 3ML Co/4ML Cu/3ML Co with Cu as capping layer and Pb as surfactant grown on the Cu (111). The magnetization orientation of two Co layers is in the out of plane with an angle q_0 between them.

5.4.2 Spin Torque Calculation and Discussion

In this section, we numerically calculate the magnitude of the spin torques, within the Co1/Cu/Co2 perpendicular PSV structure. The parameters for fcc Co of our structure is assumed to the same as those of hcp Co with in-plane easy axis, i.e. $h_{Co} \approx 38\%$, spin diffusion lengths $l_{\mathrm{sdl}}^{\mathrm{Cu}} \approx 140$ nm, $l_{\mathrm{sdl}}^{\mathrm{Co}} \approx 60$nm and $l_J^{\mathrm{Co}} \approx 3$nm. The parameters for specular reflection at the Co-Cu interface are $T_{\uparrow(\downarrow)}^{\mathrm{Cu\text{-}Co}} = 0.73$ (0.54), $R_{\uparrow(\downarrow)}^{\mathrm{Cu\text{-}Co}} = 0.27$ (0.46), $T_{\uparrow(\downarrow)}^{\mathrm{Co\text{-}Cu}} =$ 0.94 (0.33) and $R_{\uparrow(\downarrow)}^{\mathrm{Co\text{-}Cu}} =$ 0.06 (0.67). The detailed calculation procedure has been

described in the combined model at section 4.2, which incorporates both ballistic spin injection at the two Co-Cu interfaces and diffusive spin relaxation within the Co and Cu layers. There are two contribution to the total spin torques exerted on the free layer, one is from the absorbed spin current at the interface, which results in an in-plane torque, v_{abs} and an out-of-plane spin torque, u_{abs}; the other contribution is from the transmitted current within the free layer which also results in two spin torques, v_t in the in-plane direction and u_t in the out-of-plane direction. When spin current enters the Cu layer, it maintains its spin orientation while its magnitude decays exponentially with decay length l_{sdl}^{Cu}. In Fig 5.6, the magnitude of these spin torques has been plotted as a function of the initial angle θ_0 between the magnetization direction of the pinned and free Co layers where the electron current density is taken to be $10^7 A/cm^2$. The numerical results for PSV with in-plane magnetization are also presented for comparison. We know that the in-plane spin torque (i.e. $v_{abs} + v_t$) tends to produce a precessional motion of M_{Co2}, while the out-of-plane

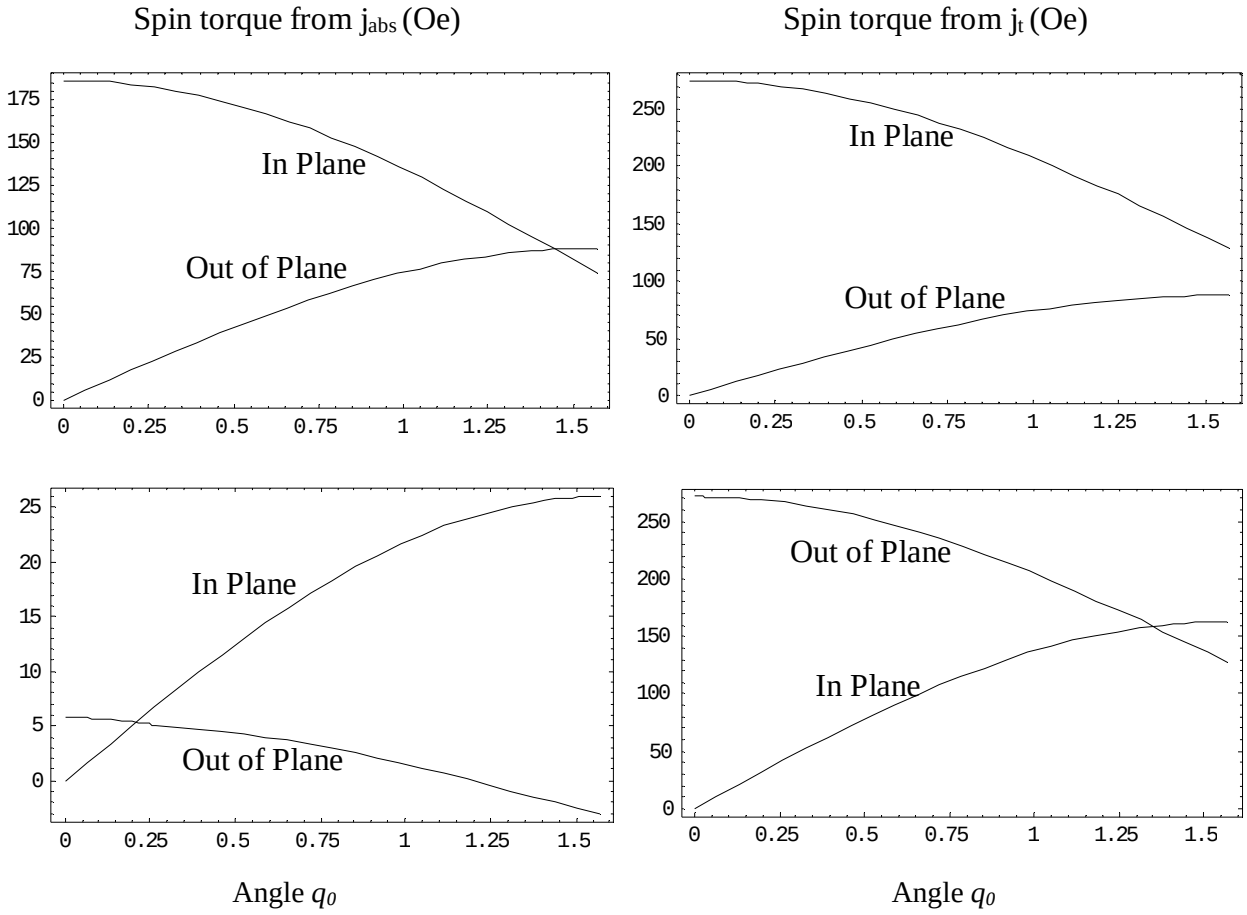

Figure 5.6 Variation of in- and out-of plane spin torques from absorbed j_{abs} (left) and transmitted j_t (right) spin currents as the function of the angles θ_0 between the magnetization direction of the pinned and free Co layers for Co/Cu/Co pseudo spin valve structure with perpendicular (upper) and in-plane (bottom) magnetization, respectively.

component (i.e. $u_{abs} + u_t$)) tends to rotate the magnetization direction of the free FM layer towards that of the pinned layer. Comparing the relative magnitude of the two spin torque contributions, the in-plane and out-of-plane effective fields due to $\mathbf{j}_{abs}$ is comparable to $\mathbf{j}_t$ in PSV. By contrast in PSV with in-plane magnetization, the contribution due to $\mathbf{j}_{abs}$ is significantly smaller, i.e. by a factor of ~ 5 (50) for the in-plane (out-of-plane) components. Thus in PSV with perpendicular magnetization, $\mathbf{j}_{abs}$ is a significant contributor to the total

spin momentum transfer, and must be included in the spin transport model, in addition to the relaxation of the transverse spin components of $\mathbf{j}_t$. Enhancing the absorbed spin current by increasing the spin-dependence of the specular reflection at the interfaces is thus one possible method to reduce the critical current density. For PSV with perpendicular magnetization, when the magnetization direction of the two Co layers are parallel to each other, i.e. $\theta_0 = 0$, there is no out-of-plane spin torques while the in-plane spin torques are largest at 186Oe and 275Oe, corresponding to $\mathbf{j}_{abs}$ and $\mathbf{j}_t$, respectively, which means that there is only an in-plane effective field exerted on free layer. Because both the transverse spin accumulation $\mathbf{m}_\perp$ and $\mathbf{j}_t$ have only one component, which is in the direction of $\mathbf{M}_{Co2}$. It is observed that both in-plane spin torque components decrease, while both out-of-plane components increase in magnitude as θ_0 increases. When θ_0 increases to $\pi/2$, i.e. the magnetization direction of the free layer is in the in-plane direction, the out-of-plane spin torque reaches its maximum while the in-plane spin torques are smallest. The out-of-plane spin torque due $\mathbf{j}_{abs}$ and $\mathbf{j}_t$ reaches almost identical values of 88.3Oe and 87.8Oe, respectively. Considering previous experimental studies of the magnetization switching in the Co layer with perpendicular anisotropy, the critical magnetic fields to switch the free layer are mostly in the range of 100Oe to 500Oe [15,16]. From our calculations, the lower end of this field range can already be obtained with a critical current density j_{crit} in the order of 10^6 to 10^7 A/cm^2. Due to the smaller spin torque from $\mathbf{j}_{abs}$, our calculations predict a higher j_{crit} for PSV with in-plane magnetization. This is also in line with experimental results for actual CIMS in PSVs with in-plane easy axis, for which the critical current density is observed to be of the order of 10^7A/cm^2. However

until now, there is no publication of observation of CIMS in the perpendicular spin valve structures.

5.4.3 Conclusions

In section 5.4, we have utilized the spin transport model to calculate the current-induced spin torque in the free layer of a PSV structure, where the magnetization of the two ferromagnetic layers is in the out-of-plane direction. The model incorporates ballistic spin-dependent transmission/reflection of electrons at the Co-Cu interfaces, and the diffusive relaxation of spin accumulation within the free layer. From the spin current transport analysis result, we obtain a significant contribution to the spin torque from the absorbed spin current $\mathbf{j}_{abs}$, due to the specular reflection process at the Co-Cu interfaces. This contribution is comparable to the contribution from spin relaxation of transmitted spin current $\mathbf{j}_t$ within the free Co layer. On the other hand the contribution from $\mathbf{j}_t$ far outweighs (by up to a factor of 50) that of $\mathbf{j}_{abs}$ in PSV with in-plane magnetization. The total spin torque from the two contributions is higher and hence its corresponding critical current for CIMS is lower in PSVs with perpendicular magnetization, compared to those with in-plane magnetization directions. In addition, perpendicularly magnetized PSV when used as an MRAM has other known advantages, such as greater magnetic stability. Our analysis thus suggests the use of new ferromagnetic and substrate materials in future MRAMs, which are able to induce a strong easy axis in the perpendicular direction, as well as enhance the spin dependence of specular reflection at the interfaces (so as to increase $\mathbf{j}_{abs}$).

References

[1] S. Zhang, P. M. Levy and A. Fert, Phys. Rev. Lett. 88, pp.236601. 2002.

[2] A. Shpiro, P. M. Levy and S. Zhang, Phys. Rev. B. 67, pp.104430. 2003.

[3] M. D. Stiles and A. Zangwill, J. App. Phys. 91, pp.6812-6817. 2002.

[4] C. Heide, P. E. Zilberman and R. J. Elliott, Phys. Rev. B. 63, pp.064424. 2001.

[5] M. D. Stiles, J. Appl. Phys. 79, pp.5805-5810. 1996.

[6] F. J. Castano, Y. Hao, M Hwang, C. A. Ross, B. Vögeli, Henry I. Smith and S. Haratani, Appl. Phys. Lett. 79, pp.1504-1506. 2001.

[7] F. J. Albert, J. A. Katine, R. A. Buhrman and D. C. Ralph, Appl. Phys. Lett. 77, pp.3809-3811. 2000.

[8] T. Ochiai, Y. Jiang, N. Tezuka, and K. Inomata, has submitted to Appl. Phys. Lett.

[9] E. Girgis, J. Schelten, J. Janesky, S. Tehrani and H. Goronkin, Appl. Phys. Lett. 76 pp.3780. 2000.

[10] W. Kuch, A. Dittschar, M. Salvietti, M.-T. Lin M. Zharnikov, C. M. Schneider, J. Camarero, J. J. de Miguel, R. Miranda and J. Kirschner, Phys. Rev. B 57, pp.5340. 1998.

[11] M. T. Kief and W. F. Egelhoff, Jr, J. Appl. Phys. 73. pp.6195. 1990.

[12] M. Sawada, K. Hayashi and A. Kakizaki, Phys. Rev. B, 63, pp.195407. 2001.

[13] C.H. Lee, Hui He, F. J. Lamelas, W. Vavra, C. Uher and Roy Clarke, Phys. Rev. B 42 pp.1066. 1990.

[14] F. Huang, M. T. Kief, G. J. Mankey and R. F. Willis, Phys. Rev. B 49, pp.3962. 1994.

[15] W. F. Egelhoff Jr. and M. T. Kief, Phys. Rev. B vol, 45, pp7795-7804. 1992.

[16] J. Camarero, T. Graf, J.J. de Miguel, R. Miranda, W. Kuch, M. Zharnikov, A. Dittschar, C. M. Schneider, and J. Kirschner, Phys. Rev. Lett, pp.76 4428. 1996.

Chapter 6 Conclusion and Future Work

6.1 Conclusion

In this project, we have conducted the micromagnetic and transport analysis for two specific patterned magnetic nanostructures: namely the Permalloy antidot array and the magnetic multilayer structures. The transport and electromagnetic properties of these nanostructures have been investigated.

First, a combined micromagnetic and magnetotransport model was presented which accounts for the nonuniformity of both magnetization and current density distribution in the Permalloy antidot array. The influence from geometry and planar Hall effect on the magnetic behaviour of the antidot array was analyzed. The analysis showed that the magnetotransport behavior of a Permalloy film is strongly influenced by the antidot geometry, such as the interdot spacing and aspect ratio. The applicability of the antidot structure for high-density information storage was also investigated, by performing simulation of the recording process. This simulation involved the Karlqvist writing head field model applied to an individual information bit. Recording performance such as contrast and signal to noise ratios were analyzed as a function of antidot geometry. Further analysis on the correlation between geometry and magnetic properties may lead to the optimization of the antidot structure for storage applications.

Subsequently, the electron spin transport properties and spin polarized current

induced magnetization switching (CIMS) in the second type of magnetic nanostructure i.e. a magnetic multilayer structure were discussed. For the thin-film magnetic structures, the spin transfer torque effect, which arises from the interactions of the electron spins and local momentums of ferromagnetic materials, is a significant contributor for the magnetization switching. We introduced a model, which naturally combines the ballistic transport across the interface and the diffusive model within the free and pinned layers of a pseudo-spin-valve (PSV) structure. The effect of the spin torque, which is expressed in terms of the in-plane and out-of plane effective field was analyzed. The results showed that the spin torque exerted on the ferromagnetic layer not only depends on the transmitted current into the free FM layer, but is also related to the transverse component of the absorbed spin current at the two interfaces of the free FM layer. Based on the model, the critical current density for magnetization switching in the normal pseudo-spin-valve structures was calculated to be in the range of 10^7-10^8A/cm^2, which is within the typical range observed in existing experimental observations.

Apart from the normal pseudo-spin-valve structure, the effect of the spin torque and magnetization switching mechanism were also investigated on modified magnetic multilayer structures. First, the micromagnetic analysis of the ring-shaped spin valve structure was carried out with the application of the spin-polarized current pulse. In this model, we considered the effects of both the Oersted and exchange fields due to spin torque of the write current pulse. The switching mechanism of the spin valve was also investigated for different amplitude and duration of the current pulse, and the optimal conditions for the desired switching behavior was mapped out as a function of pulse

duration and amplitude.

Next, we considered the spin current transport in a Co/Cu/Co pseudo-spin-valve structure with and without a Ru cap layer, and concluded that the presence of the Ru layer leads to the reduction of the critical current density necessary for magnetization switching, which was later confirmed to be in agreement with the experimental studies. Our analysis considered the spin accumulations at the two interfaces of the free magnetic layer and indicated that both of them contribute to the total spin torques exerted on the free layer.

Finally, we analyzed a spin valve structure with varying easy axis orientation, ranging from the in-plane to the perpendicular (i.e. out-of-plane) direction, in order to investigate the effect of anisotropy orientation on the current-induced magnetization switching of the ferromagnetic layer under the applied of the perpendicular to plane current. Our calculations predicted a lower critical current density which is in the order of 10^6-10^7A/cm^2 compared with the PSV structure with in-plane magnetization. This study makes an important contribution to the study of current induced magnetization switching for the possible future applications of the perpendicular spin valve structures, which can achieve a high density due to the small aspect ratio it requires.

Based on the theoretical analysis of mechanism of current induced magnetization switching, we also concluded that there are several methods which may be used to decrease the critical current density: a) increasing the spin polarization ratio of the pinned ferromagnetic layer, and b) to increase the transverse component of spin accumulation on

both sides of ferromagnetic layer, by having strong spin-dependent scattering at the interfaces. In addition, the geometry and anisotrophy properties of the ferromagnetic layer could also be optimized for further reduction of the critical current density. Further studies need to be performed on these aspects.

The electromagnetic properties related to electron spins are becoming more significant, with the decease of the size of magnetic structures which are being fabricated and the continuing demand for ever smaller device feature size, lower power consumption and higher speeds. So the studies which we have performed on the spin and charge transport properties, and the interaction between spin electrons and local momentum electrons provide an important contribution, which will help realize the utilization of these magnetic nanostructures in spintronic devices.

6.2 Future Work

In our electromagnetic transport model of Chapter 3, we have focused on the magnetoresistance behavior of magnetic thin film with rectangular antidot arrays for a few kinds of magnetic materials and dot shapes in order to test the general accuracy and efficiency of the transport model. However, an important extension of our work will be to incorporate the effects of domain wall dynamics and domain wall resistance. Recent works [1,2] have shown that the interaction between the conduction electrons and the domain wall is highly complex, and can significantly contribute to the overall magnetoresistance. However, the analysis is still confined to the simple one-dimensional case in the adiabatic limit. It would be interesting to see if, for example, geometrical

features such as constrictions can influence the strength of the domain wall resistance.

Effect of Domain Walls

Moreover, in our present model, the current density distribution is calculated without the consideration of the contribution of domain wall resistance. From MFM measurements [3-6] of antidot structures, it is clear that the presence of antidots induces the formation of domain walls. Previous experimental [7,8] and theoretical [9,10] studies have also shown that the effect of domain wall resistance can have a significant effect on electron transport within the films. Thus, a more refined model which combines the normal magnetotransport (i.e. AMR and Hall effects) with the domain wall resistance, should be developed to analyze the transport properties in nanostructures with multiple domains.

Multi-domain Switching

In our combined ballistic and diffusive models, the spin current transport and spin torque in the pseudo-spin-valve structure were analyzed, and the effect of these spin torque contributions was to induce magnetization switching of the free layer. However, one simplifying assumption of our analysis is that the magnetization of the ferromagnetic layer is uniform (single domain), and that the magnetization switching is coherent in nature. At present the dimension of the spin valve pillar is about 100nm, which means that magnetization switching may not be entirely in the coherent mode. Furthermore, the nonuniformity of current density through the device means that certain regions of the free layer would switch first (domain nucleation). Recent studies on spin excitation induced by

spin polarized current [11,12] have also shown that current-induced magnetization switching may occur via several modes, including chaotic dynamical modes, which are far removed from the simple coherent switching model. Thus, an extension to our existing model, a detailed study based on micromagnetics of the magnetization switching and precession in ferromagnetic layers with multi-domain structure should be performed. Furthermore, due to the presence of domain walls, further investigation could also incorporate the effect of domain wall displacement [13,14] induced by the spin polarized current.

Further Reduction of Ic

Our analysis has revealed some methods to achieve a lower critical current density Ic in the spin valve structures, such as the insertion of a Ru cap layer on top of the free ferromagnetic layer or by modifying the easy axis orientation of the free layer. Another method is to make use of a spin injector with higher spin polarization ratio, such as half metals, Fe_3O_4 or CrO_2, with their (theoretically) almost 100% spin polarization ratio. But material research into half metals is on-going, and there are still some obstacles to overcome before the spin polarization can be demonstrated to approach 100% at room temperature. In addition, further experimental studies need to be performed to investigate the compatibility of interfacing half metals with semiconductors or other nonmagnetic metals, since the interfacial quality will strongly determine the spin injection efficiency.

Besides the spin valve structure, another technologically important structure as far as MRAM application is concerned, is the magnetic tunneling junction (MTJ) structure.

MTJs have been shown [15] to achieve higher MR ratio, compared with the PSV structure. Recently, CIMS has been successfully demonstrated in an MTJ structure [16] To achieve this, researchers have fabricated MTJs with extremely thin (sub 1 nm thickness) tunnel oxide layer, in order to reduce the resistivity of the structure, and allow sufficient current to flow to induce CIMS. The reported critical current density is in the same order as that in the spin valve structures. According to our analysis, the presence of a cap layer made of Ru, could decrease the Ic. Hence, we may propose a novel new structure combing the spin valve and magnetic tunneling junctions, which could produce a larger signal, compared with a purely PSV structure, and which may also achieve a lower Ic.

References

[1] G. Tatara and H. Kohno, Phys. Rev. Lett. 92, pp.086601. 2004.

[2] J. Shibata,G. Tatara and H. Kohno, Phys. Rev. Lett. 94, pp.076601. 2005.

[3] P. Vavassori, G. Gubbiotti, G. Zangari, C. T. Yu, H. Yin, H. Jiang and G. J. Mankey, J. Appl. Phys. 91, pp.7992-7994. 2002.

[3] C. C. Yao, D. G. Hasko, Y. B. Xu, W. Y. Lee, and J. A. C. Bland, J. Appl. Phys. 85, pp.1689. 1999.

[5] C. T. Yu, H. Jiang, L. Shen, P. J. Flanders and G. J. Mankey, J. Appl. Phys. 87, pp.6322-6324. 2000.

[6] U. Welp, V. K. Vlasko-Vlasov, G. W. Crabtree, Carol Thompson, V. Metlushko and B. IIic, Appl. Phys. Lett. 79, pp.1315-1317. 2001.

[7] U. Ebels, A. Radulescu. Y. Henry, L. Piraux and K. Oundajela, Phys. Rev. Lett. 84, pp.983-986. 2000.

[8] Qi Li, Y. F. Hu and H. S. Wang, J. Appl. Phys. 89, pp.6952-6954. 2001.

[9] P. M. Levy and S. Zhang, Phys. Rev. Lett. 79, pp.5110-5113. 1997.

[10] A. Brataas, G. Tatara and G. E. Bauer, Phys. Rev. B. 60, pp.3406-3413. 1999.

[11] K. J. Lee, A. Deac, O. Redon, J. P. Nozieres and B.Dieny, Nature Materials 3, pp.877-881. 2004.

[12] M. Covington SCIENCE 307 (5707), pp.215-216. Jan 2005.

[13] E. Salhi and L. Berger, J. Appl. Phys. 76, pp.4787-4792. 1994.

[14] L. Gan, S. H Chung, K. H. Aschenbach, M. Dreyer and R. D. Gomez, IEEE, Trans. Magn. 36(5), pp.3047-3049. 2000.

[15] R. C. Sousa, J. J. Sun, V. Soares, P. P. Freitasa, A. Kling, M. F. da Silva, and J. C.

Soaresb. J. Appl. Phys, 85(8), pp.5258-5260. 1999.

[16] G. D. Fuchs, N.C. Emley, I. N. Krivorotov, P. M. Braganca, E. M. Ryan, S. I. Kiselev, J. C. Sankey, D. C. Ralph and R. A. Buhrman, Appl. Phys. Lett, 85, pp.1205-1207. 2004.

List of Publications and Conferences Attended

1. J. Guo and M. B. A. Jalil, "**Combined ballistic and diffusive model of spin-polarized current-induced magnetization switching in pseudo-spin-valve structure"** *Physical Review B*, Vol.71, 224408. 2005.

2. J. Guo, M. B. A. Jalil and Y. Jiang , "**Current induced magnetization switching in pseudo-spin-valve multilayers with and without Ru capping layer"** *Physical Review B*, Vol.72, 064439. 2005.

3. J. Guo and M. B. A. Jalil, "**Micromagnetic study of switching in ring-shaped spin valve structures**" presented at 9th Joint MMM/InterMag Conference Anaheim, California, USA, 5-9, Jan 2004 and published in *IEEE Transactions on Magnetics* Vol. 40, No. 4, pp.2122-2124, July. 2004.

4. J. Guo and M. B. A. Jalil, "**Simulation of magnetic recording of periodic antidot array**" presented at International Conference on Magnetism, Rome, Italy, July, 27-Aug, 1 2003 and published in *Journal of Magnetism and Magnetic Materials*. Vol. 272-276, pp.722-723, May. 2004.

5. J. Guo and M. B. A. Jalil, "**Transport modeling of Py film with antidot array**" presented at 47th Annual Conference on Magnetism & Magnetic Materials, Tampa, Florida, USA, Nov 11-15, 2002 and published in *Journal of Applied Physics*, Vol. 93, No.10, pp.7450-7452, May. 2003.

6. J. Guo and M. B. A. Jalil, "**Finite element modeling of charge transport and magnetization of Py film with antidot array**", 4th ASEAN ANSYS User Conference, Singapore, 5-6, Nov. 2002.